

# **GROWTH DYNAMICS OF SINGLE BACTERIAL CELLS**

Sarah Boulineau



# **GROWTH DYNAMICS OF SINGLE BACTERIAL CELLS**

Proefschrift

ter verkrijging van de graad van doctor  
aan de Technische Universiteit Delft,  
op gezag van de Rector Magnificus prof. ir. K.C.A.M. Luyben,  
voorzitter van het College voor Promoties,  
in het openbaar te verdedigen op woensdag 12 juni 2013 om 10.00 uur  
door

Sarah BOULINEAU

Ingénieure diplômée, Université de Strasbourg  
geboren te Nice, Frankrijk

Dit proefschrift is goedgekeurd door de promotor:  
Prof. dr. ir. S.J. Tans

Samenstelling promotiecommissie:

Rector Magnificus,	voorzitter
Prof. dr. ir. S.J. Tans,	Technische Universiteit Delft, promotor
Prof. dr. O.Tenaillon,	Inserm, Frankrijk
Prof. dr. E.J. Bruggeman,	Vrije universiteit Amsterdam
Prof. dr. P.R. ten Wolde,	Vrije universiteit Amsterdam
Prof. dr. H.J. Tanke,	Universiteit Leiden/Technische Universiteit Delft
Prof. dr. ir. J.J. Heijnen,	Technische Universiteit Delft
Dr. J.W. Veening,	Rijksuniversiteit Groningen



The work described in this thesis was performed at the FOM Institute AMOLF, Science Park 104, 1098 XG Amsterdam, the Netherlands. This work is part of the research program of the Foundation for Fundamental Research on Matter (FOM), which is financially supported by the Netherlands Organization for Scientific Research (NWO).

Nederlandse titel: Groeidynamiek van individuele bacteriële cellen.

ISBN: 978-90-77209-73-8

A digital version of this thesis can be obtained from <http://www.amolf.nl> and from <http://repository.tudelft.nl>. Printed copies can be obtained by request via email to [library@amolf.nl](mailto:library@amolf.nl)

Cover by Thijs van Engeland

© 2013 by S. Boulineau

Printed by CPI-Wöhrmann Print Service – Zutphen







# Contents

<b>1 Introduction</b>	9
1.1 From molecular biology to systems biology	10
1.2 Quantitative single-cell dynamics studies	11
1.3 Scope of the thesis	15
<b>2 Controlling living cells and organisms with microfabricated polyacrylamide membranes</b>	17
2.1 Introduction	18
2.2 Results	20
2.3 Discussion	28
2.4 Materials and methods	31
<b>3 Single-cell dynamics reveals sustained growth during diauxic shifts</b>	41
3.1 Introduction	42
3.2 Results	43
3.3 Discussion	54
3.4 Appendix	57
<b>4 Prolonged linear growth in single bacterial cells upon exposure to antibiotics</b>	67
4.1 Introduction	68
4.2 Results	70
4.3 Discussion	74
4.4 Materials and methods	76
<b>5 Noise propagation from enzyme expression to cellular growth, and back</b>	79
5.1 Introduction	80
5.2 Results and discussion	80
5.3 Appendix	87
<b>6 Transient dynamics during nutrient shifts</b>	101
6.1 Introduction	102
6.2 Results and discussion	103
6.3 Conclusions and outlook	113
6.4 Materials and methods	115

<b>Bibliography</b>	117
<b>Summary</b>	133
<b>Samenvatting</b>	137
<b>Acknowledgements</b>	141
<b>List of publications</b>	143
<b>Curriculum Vitae</b>	145

# 1

## Introduction

Molecular biology in the twentieth century was a revolutionary discipline aimed at understanding biological processes mechanistically. Many successes of molecular biology came from interdisciplinary work involving physicists, geneticists and structural chemists. Fundamental discoveries of molecular biology include the demonstration that genetic mutations arise spontaneously, rather than being a response to selection [1], the discovery of DNA as carrier of the genetic material [2], the double helical structure of the DNA molecule by Watson and Crick in 1953 [3, 4], and gene regulation in 1961 by Jacob and Monod with the *lac* operon [5]. However, the focus of molecular biology was mostly on the characterization of individual macromolecules, and despite the initial influence of physicists, molecular biology developed into a qualitative, rather than quantitative, science [6].

A living cell can be viewed as a dynamical system in which a large number of different molecules react continuously with one another. Molecular interactions are central to biological function: gene expression, protein folding and function or enzymatic reactions are but a few examples of such interactions. To understand how the interaction between different components leads to biological function, it is not sufficient to study individual macromolecules. Systems biology is the discipline that aims to answer this question [7]. Although in the 1960s and 1970s some efforts were made to build mathematical models that describe cellular regulatory circuits [8, 9], system-level analysis of biological regulation was pushed by technology development in the 1980s and 1990s. With automated DNA sequencers it became possible to sequence entire genomes [10], with DNA microarrays to measure the expression level of a large number of genes [11], while advances in mass spectrometry made it possible to identify and quantify proteins and metabolites, and gave rise to the fields of proteomics and metabolomics [12, 13]. The advantage of high-throughput technologies is that they provide complete information about one layer of the system (genome, proteome, metabolome etc.) [7]. However, to understand how cells function, it has appeared necessary to understand the connection between these different layers and their effects. Integrative ‘omics’ studies can address this issue, but analyzing the data remains challenging because of the complexity of even the simplest bacterial cells. With genome-wide techniques, correlations between concentrations of molecules are identified, and models are used to determine the underlying structure of the molecular network [7]. However, these models do not explain correlations in terms of molecular mechanisms.

In parallel with genome-wide approaches, small scale approaches have been followed, where usually a circuit composed of a few proteins is studied. Here, the objective typically is to see how a particular molecular mechanism leads to a particular biological function. Experimental studies of cells response to perturbations are often combined with mechanism-based models that can then be used to predict cellular behavior. These models are based on kinetic parameters determined experimentally. Thus one limitation comes from the estimation of these parameters, as they are not always known and can be difficult to measure [7]. This approach has been used for instance in signaling networks such as bacterial chemotaxis [14, 15], transcriptional regulatory networks [16], and in cell fate decisions [17-19].

## **1.2** Quantitative single-cell dynamics studies

### **1.2.1 Motivation**

One of the generic features of life at the molecular level is the stochasticity, or randomness of molecular motion and reactions [20]. Cells must rely on noisy signals in biochemical networks to make decisions [21]. Molecular noise is unavoidable: biochemical reactions involve a low number of molecules subject to Brownian motion, which then gives rise to stochastic fluctuations in their interactions [22]. Thus, isogenic cells experiencing the same environment will display slightly different behaviors [23]. In addition to the stochastic nature of for example gene expression, other cell parameters contribute to cellular heterogeneity, such as cell cycle stage [24, 25], random partitioning at cell division [26], aging [27] and epigenetic factors [28-30]. Two well-known examples of phenotypic variability are persistence [31], where a fraction of cells is able to resist antibiotics, and bistability, where a population of cells in presence of intermediate inducer concentrations is divided between induced and non-induced cells [32]. Traditional assays in microbiology provide information on the average of the population, and thus hide cell-to-cell variability. Experiments with single-cell resolution provide the opportunity to directly investigate the causes and consequences of such cellular heterogeneity.

Thanks to classic biological studies, and ‘omics’ technologies, the structure of gene regulatory networks, interactions between proteins and metabolic pathways are fairly well characterized for many biological functions [12, 33, 34]. To understand how these different networks respond to perturbations, it is nec-

essary to study their dynamics. Though it is now possible to perform single-cell analysis with omics-based methods, most of these techniques require cell lysis, and thus give information of genes, proteins and metabolites at specific time points outside of the cell's physiological environment [35]. These limitations can be overcome with live-cell imaging, which is non-invasive and permits spatiotemporal characterization of biological processes. In particular, time-lapse fluorescence microscopy coupled with fluorescent reporters has proven a powerful tool to investigate the dynamic properties of gene expression in single cells [36]. With automated image analysis, the tracking of the fate of many single cells over several generations (a time usually sufficient to account for biological processes of interest such as gene regulation) has become feasible. For instance, the differentiation dynamics of the *Bacillus subtilis* competence circuit have been investigated with this approach [37, 38]. To control the cellular environment, it is possible to combine this technique with either agarose pads or microfluidic devices. With agarose pads the environment stays constant in time, while microfluidic devices permit changes in the environment.

In this thesis, we use the model organism *Escherichia coli* to answer the general question: how does the growth of cells respond to perturbations? These perturbations can be either internal, such as gene expression noise, or external, which involve changes in the cellular environment. As detailed in the next section, the nature of stochastic gene expression has been well characterized. Recent studies have shown that noise can have functional roles in genetic circuits, for instance in cell fate [39]. However, the role of stochasticity in cellular growth and metabolism remains only scarcely explored. One of the most analyzed systems, the *lac* system, displays stochasticity in expression [40], and it was shown that stochastic repressor-operator association and dissociation events affect the cells transition from the 'off' to the 'on' state [29]. But the impact on growth is not well known. In general, the propagation of noise in gene expression to growth has not been thoroughly investigated. It is an important issue because random fluctuations in metabolic efficiency could compromise biological growth itself. Indeed, metabolic instability has been hypothesized to cause various critical physiological phenomena ranging from persistence in bacteria [41] to metabolic switching in cancer [42].

## 1.2.2 Dynamics of noise in gene expression

Since the work of Arkin *et al.* [43] showing a functional role for stochastic gene expression in phase  $\lambda$  more than ten years ago, the origins and consequences



of noise have been studied intensively, both experimentally and theoretically [20, 39, 44, 45]. It is not our intent to present an exhaustive review of the subject. Rather, we highlight here some landmark studies that used temporal information to understand gene regulation, an essential tool for the topics explored in this thesis.

One of the first studies to explore the sources of noise experimentally were by Elowitz *et al.* and Ozbudak *et al.* in 2002 [40, 46]. By measuring the expression of two different fluorescent proteins under the control of identical promoters in *Escherichia coli*, a first study [40] could distinguish between two sources of noise: extrinsic noise, which affects the expression of both copies of the gene equally, and intrinsic noise, which affects each copy of the gene independently, resulting in uncorrelated temporal fluctuations in the expression levels of the two genes. Depending on the promoter, both sources of noise can be significant. A second study [46] compared the noise levels of a reporter gene with varied transcription and translation rates in *Bacillus subtilis*. It was found that transcription is the dominant source of noise in prokaryotes, which confirmed a previous model of stochastic gene expression [47]. Recent single-molecule investigations in *E. coli* showed directly how proteins are produced in stochastic bursts [48, 49], caused by the production of mRNA molecules in transcriptional bursts [50]. Several studies have further investigated regulation at the mRNA level by means of single-molecule FISH (fluorescent *in situ* hybridization), both in prokaryotes and eukaryotes [51-53]. Intrinsic noise arises from these random fluctuations inherent to transcription and translation, while extrinsic noise has been hypothesized to be caused by differences between cells in global factors such as number of polymerase enzymes or ribosomes.

Gene expression noise dynamics can be characterized by its autocorrelation time, which is the characteristic time over which fluctuations persist. Intrinsic fluctuations were shown to persist only for a few minutes, consistent with the known mRNA half-life, while extrinsic fluctuations lasted a cell cycle in *E. coli* [54]. By studying the effects of noise in simple synthetic genetic networks, it was found that fluctuations in the expression of one gene can propagate to create fluctuations in downstream genes [55]. This temporal information can also be used to infer regulatory interactions. For instance, Dunlop *et al.* [56] showed how time-delayed correlations between two proteins can inform on whether one protein activates or represses the other, or whether a third protein controls them both (see Fig. 1.1).

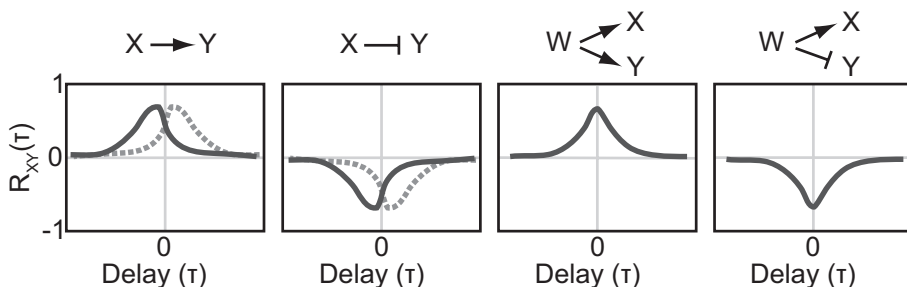


**Figure 1.1** Inferring regulatory interactions from cross-correlations. Top: schematic representation of four different regulatory motifs (X activates Y, X represses Y, W activates X and Y, W activates X but represses Y). Bottom: cross-correlation function for X and Y. The intensity of  $R_{XY}(\tau)$  indicates how strongly  $X(t + \tau)$  is correlated with  $Y(t)$ . A positive value denotes a positive regulation, while a negative value denotes a negative correlation. The timing of peaks or dips shows causality in this regulation. For instance, if X activates Y, the peak appears at negative delay times because X is upstream of Y (first column). Plain lines correspond to the motifs on the top column. Dashed lines correspond to the same motif where X and Y are exchanged. Adapted from [57].

### 1.2.3 Interplay between gene expression and growth

In order to survive, the cell's physiology must be tuned to the environment. Thus growth must be properly regulated and balanced, which can be a challenging task for cells living in fluctuating environments. For instance, when the conditions are favorable, it is advantageous for the cells to grow fast. On the contrary, upon stressful conditions such as starvation or presence of toxins, slow growth or even dormancy may allow for survival. Many other processes must in turn be coordinated with the growth rate, such as nutrient uptake, synthesis of the right amount of metabolites and DNA replication. These requirements suggest a complex interplay between gene expression and growth rate, where each depends on the other. At steady-state growth, a large fraction of all genes was found to exhibit a close correlation with the cellular growth rate [58]. In *E. coli*, a similar result was found with protein levels [59]. Hence gene expression changes are due to specific gene regulation mechanisms and global growth rate effects. A challenge is then to identify the regulatory parameters responsible for these gene expression changes. By using a small number of growth rate-dependent parameters (such as gene copy number or transcription rate), Klumpp *et al.* [60] developed a simple quantitative model of the coupling between the population mean gene expression and growth.

One of the goals of systems biology is to link molecular mechanisms with cellular behavior. Several studies have characterized how gene expression affects cellular growth [61-63], and conversely how the growth rate affects gene expression [60, 64-66]. What the origin of the interdependence of gene expression and cell growth is, is less clear. Scott *et al.* [67] used a phenomenological approach that does not require any information of molecular mechanisms, to characterize bacterial physiology. They proposed some ‘bacterial growth laws’ that partition the proteome in three components: a fixed fraction invariant to growth rate, a ribosome-affiliated fraction, and the remainder.

Most of the studies mentioned here were performed at a steady-state growth rate. Significant progress has been made to understand how cells achieve growth homeostasis, for instance by exposing the cells to different environmental perturbations or stresses. However, the cellular growth response to environmental changes has been obtained primarily using bulk techniques that measure the growth rate of the population as a whole [68-73]. Consequently, the transient change of growth rate of individual cells and its causal relationship to molecular mechanisms has been less well investigated.

### **1.3** Scope of the thesis

The goal of this thesis is to characterize the dynamics of cellular growth under two different types of perturbations, internal and external, and to link it to the dynamics of gene expression. To this end, we use a single-cell approach, combined with fluorescence time-lapse microscopy to measure both growth rate with sub-cycle resolution, and expression of genes of interest. Chapter 2 provides details on a novel hybrid microfluidic design used to control the cellular environment in chapters 3, 4 and 6. This device is well-suited to investigate growth at the single-cell level.

Chapter 3 shows how cells respond during a diauxic shift, the classic experiment originally performed by Monod in bulk. Surprisingly, we find that some cells do not exhibit a lag phase, as had previously been concluded from bulk data and widely assumed to be obligatory; a fraction of about 10% continues to grow at the same speed. A mathematical model integrating expression and growth that matches with the data provides a molecular-level explanation.

Chapter 4 deals with the response of cells growing on lactose to a translation-inhibiting antibiotic. In addition to growth, several essential enzymes are monitored. Inhibition of *lac* synthesis, with maintenance of ribosome synthesis,

leads to linear growth. The linear growth rate is correlated to the size of the cell, or age, at the moment of drug addition, resulting in significant single cell heterogeneity. Further increasing the antibiotic concentration leads to complete growth arrest but allows growth to proceed transiently, until ribosome synthesis is arrested.

In chapter 5, cross-correlation functions are used to demonstrate that expression noise of a single metabolically active enzyme can cause noise in cellular growth, mediated by transmission through the underlying metabolic network. In addition, growth noise transmits back to enzyme expression to form a loop, mediated not by specific regulatory interactions but by general growth factors that affect gene expression such as ATP. A stochastic model that integrates expression and metabolism accurately predicts correlations in re-wired networks.

Chapter 6 is a preliminary work concerning the transient dynamics of growth and ribosome synthesis during nutrient shifts. Growth rate is modulated by varying only the external concentration of glucose. The data show that adaptation to a higher growth rate is surprisingly slow while adaptation to a lower growth rate is comparatively faster. In both cases the response of individual cells is rather homogeneous.

## Controlling living cells and organisms with microfabricated polyacrylamide membranes

2

*The need for precisely controlling the environment of living cells and organisms has stimulated many developments in microfluidic technologies. However, their implementation in biology laboratories can be limited by technical barriers or by a lack of versatility of the methods. Here, we present a simple technique based on polyacrylamide membranes to build chemostat-like devices for cells and organisms, with the possibility to embed microfabricated features in the membrane. Polyacrylamide gels possess many beneficial properties for cell culture, being soft, porous and transparent, while simple to fabricate and handle. Here, we demonstrate the long-term growth of organisms ranging from prokaryotes to multicellular eukaryotes in a variety of polyacrylamide-based designs. These devices allow for precise temporal control of culture conditions, such as the chemical composition of the growth medium and the presence of drugs, on a minute timescale. In addition, we show how spatial confinement conferred by these devices allows for time-lapse microscopy in a parallel fashion.*

## 2.1 Introduction

The ability to create precisely controlled microenvironments has been pursued in microbiology [74], cell biology [75] and tissue engineering [76]. Microfluidic techniques have emerged as an important tool to impose spatial confinement, control transport of chemicals on the micrometer scale and drastically increase the level of parallelization of data acquisition [77, 78]. However, realizing these capabilities often requires technologically complex devices, potentially comprising microfabricated structures with multiple layers, surface treatments and multiple modules [74-76, 78]. As a consequence, fabricating and handling such devices can be challenging, which has limited their use in laboratories without specific microfabrication expertise [79].

PDMS-based microfluidics is extremely versatile and has been applied to the culture of bacteria [80], yeast [81], mammalian cells [82], and even embryos [83] or nematode worms [84]. While exquisite for controlling flows, PDMS based devices can require sophisticated designs to cope with the constraints of living objects and can be ultimately limited by the properties of PDMS as a material. PDMS devices can ensure localization of the object under study by confinement in microchambers and controlled medium exchange by laterally connecting channels that are narrow enough to prevent escape of the cells [85, 86]. However, whether it is necessary to either impose spatial confinement or decouple flow from diffusion, this requires multi-layered flow-cell designs and sometimes integration of *in situ* valves [87]. Watertight closure of the system is generally performed by a plasma treatment of the PDMS [88], which can be incompatible with complementary treatments required to obtain the stable hydrophilic or hydrophobic properties ensuring appropriate adhesion of cells to the surfaces of the culture chambers [89]. PDMS is not porous to aqueous solutions [88], which is desirable in some applications but a limitation in others, as it does not allow building osmosis membranes and can lead to local medium heterogeneities [90, 91] and accumulation of toxic residues [92]. In addition, PDMS has poorly tunable mechanical properties, which is critical for the correct growth of many cell types [93, 94].

Many of these issues could be addressed by the use of hydrogels. Hydrogels allow for free diffusion of the medium throughout the device, thereby ensuring uniformity of the cellular environment. In addition, hydrogels have highly tunable mechanical properties [95]. For these reasons, a variety of microenvironments based on hydrogels are being explored for tissue engineering [76, 96]. So far, the most commonly used hydrogel for the study of micro-organisms

as well as multicellular organisms is agarose, which is commonly used as an ‘agar pad’, a single monolayer of hydrogel, to confine bacteria [97], yeast [98] or nematodes [99, 100] to the imaging plane for live microscopy imaging. Simple layers of agarose have also recently been used as membranes to precisely control bacterial medium as a function of time [30, 101, 102]. In addition, agarose has been structured on the micrometer scale, e.g. to create grooves that guide the growth of bacteria [103, 104] or to build microchambers to spatially confine live nematode larvae [105]. However, agarose is brittle and tears readily, making it difficult to manipulate, especially in the form of thin layers. This severely limits microfabrication possibilities [106]. In addition, agarose is composed of sugar and can be directly metabolized by some organisms [107] or may contain residual non-purified simple sugars, which could hinder study of growth under well controlled conditions.

Here we propose polyacrylamide hydrogels as an alternative substrate for building controlled microenvironments. Polyacrylamide gels have several practical advantages that make them ideally suited for developing devices for live microscopy in biological studies. First, polyacrylamide is a commonly used material in biology laboratories for DNA and protein electrophoresis and its microfabrication requires minimal technological investments, as we will show below. Polyacrylamide gels are physico-chemically well characterized and known to be biocompatible [108, 109]. They are mechanically stronger (fracture energy  $G \sim 10 - 50 \text{ J.m}^{-2}$  [110]) than agarose gels ( $G \sim 0.1 - 6 \text{ J.m}^{-2}$  [111, 112]), and hence allow for easier handling and are better suited for microfabrication. Their elastic properties are tunable over a wide range, which allows to build environments with well controlled mechanical properties [108, 109, 113, 114]. They are permeable to aqueous solutions and composed of a synthetic polymer that cannot be metabolized as a carbon source, which allows for excellent control of the growth conditions. While polyacrylamide gels have been micropatterned by photopolymerization inside glass or PDMS microchannels [115-117], their unique properties have not yet been exploited to construct devices for biology studies using standard soft lithography techniques.

Here, we demonstrate two essential properties of polyacrylamide gels that enable the building of controlled environments and can be used simultaneously. First, we describe a soft lithography method to transfer micropatterns from a silicon wafer to a polyacrylamide gel, allowing to integrate confining culture chambers or microchannels. Second, we show how to use polyacrylamide gels as membranes to control the transfer of chemicals, adapting designs already developed with other materials, such as devices based on dialysis membranes for changing medium in time [118] or based on diffusion between lateral channels

for generating gradients in space [106, 119]. We describe several elementary designs for culturing cells and organisms, comprising a polyacrylamide membrane constrained between glass or PDMS components. We then demonstrate their use for the study of a range of organisms. We show that one can control the growth of *E. coli* bacterial colonies by controlling the carbon source as a function of time, and simultaneously track the response on the level of single-cell lineages. We also show that we can confine and grow *S. pombe* yeast cells, imposing a time-controlled reversible arrest of growth by a microtubule-depolymerizing drug. Finally, we show that we can confine *C. elegans* nematodes larvae in microchambers and follow the growth of multiple individual larvae in parallel by time-lapse microscopy.

## 2.2 Results

### 2.2.1 Microfabrication of polyacrylamide gels

*Master mold* – Microfabricated polyacrylamide membranes can be indefinitely reproduced by soft-lithography from a single silicon wafer comprising the desired micropattern made of an epoxy resin, such as SU-8 (Methods). The initial master mold was made according to standard protocol by UV-lithography from a printed transparent mask, allowing the specification of an arbitrary two-dimensional pattern with a uniform height determined by the user, typically ranging from 1 to 100  $\mu\text{m}$ .

*Molding of the acrylamide* – The aqueous solution of acrylamide monomers mixed with curing agents is poured on the master mold within a contour made of glass or metal of pre-determined height, bound to the wafer with silicon grease (Methods, Fig. 2.6). The molding cavity is then closed with a silanized glass coverslip. A gel is generally obtained after 20 min at room temperature, but waiting 2 hrs ensures optimal polymerization. After polymerization, this results in a polyacrylamide gel with one face shaped as the negative of the micropattern of the master mold. We could easily obtain replica of molds going down to 10  $\mu\text{m}$  features with an apparent fidelity at the micron scale (Methods, Fig. 2.7). Note that we also use unstructured flat polyacrylamide membrane in the following. These are obtained according to the same protocol in which the wafer has been replaced by a silanized glass slide.



*Preparation of a membrane* – After polymerization, the top silanized coverslip is removed, after which the gel is cut to the experimentally required dimensions and removed with tweezers. Importantly, the polyacrylamide membranes should be rinsed in water to remove non-polymerized toxic acrylamide monomers. In our studies, transferring the polyacrylamide layer to fresh purified water at least two times for approximately 1 hr proved sufficient to ensure biocompatibility and a lack of any observed growth defect in the organisms studied in this chapter. The membrane can be stored for several weeks in an aqueous solution. Before using the polyacrylamide membrane for a cell or organism culture experiment, we soaked it two times in the appropriate medium.

### 2.2.2 Experimental designs

In Figure 2.1, we first outline the different designs used in this research. In general, all devices consist of multiple layers stacked on top of each other, with the entire device being held together by mechanical clamping (Fig. 2.1). In our case, this clamping was achieved by a metal holder with screws, with the appropriate openings for microscopy acquisition and microfluidic connectors.

In all different designs the objects under study have to be confined between the polyacrylamide membrane and the glass coverslip through which microscopy imaging is performed. Here, we use two different approaches to achieve this. In the first design, we enclose the membrane within a surrounding glass spacer sealed to a top glass slide with vacuum silicon grease (Fig. 2.1A-B). This simple design ensures sufficient air tightness to limit evaporation and allows for observation under constant conditions for up to two days, provided that nutrients in the hydrogel membrane are present in large excess. In the second design a PDMS device containing a control channel is placed on top of and in direct contact with the polyacrylamide membrane (Fig. 2.1C), thereby allowing continuous diffusion of the medium to cells or organisms growing below the hydrogel membrane. As no sealing or chemical bonding is required, the PDMS channel can be re-used many times.

Potentially, microfabricated polyacrylamide membranes and PDMS control channels can be combined depending on the experimental needs (Fig. 2.1D), with the possible designs not limited to those in Fig. 2.1. For example, more complex designs containing microchannels embedded in the gel could be fabricated.

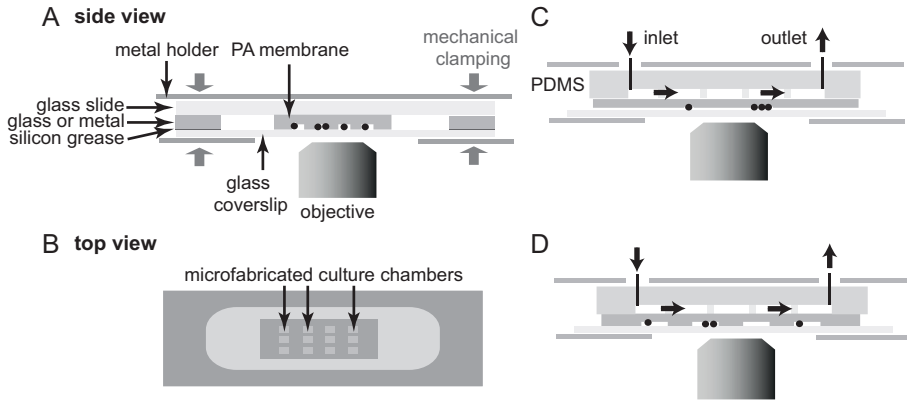


**Figure 2.1** Schematics of devices for cells or organisms culture in polyacrylamide membranes. In all devices presented here, cells or organisms (represented as black circles) grow at the interface between the polyacrylamide gel and a glass coverslip through which microscopy is performed. (A) Side view of a microfabricated membrane comprising culture chambers, mechanically clamped between a glass slide and a glass coverslip. The device is sealed with a glass or metal contour. Sealing can be enhanced by adding vacuum silicon grease between surfaces. (B) Top view of panel (A) showing the array of microchambers surrounded by the glass or metal contour. (C) Flow cell using a PDMS control channel in contact with a polyacrylamide monolayer, which allows transfer of the flowing medium to the cells. In this design, cells are compressed underneath a flat polyacrylamide monolayer. (D) A more complex device combining the microchambers of the design in panel (A) and with the PDMS control channel in panel (C).

### 2.2.3 Temporal and spatial control of the microenvironment

First, we used the advantageous transport properties of polyacrylamide gels to precisely control the medium composition in time, using an unstructured gel as a membrane, as well as in space, by setting up a concentration gradient within a membrane using molded microchannels.

In the first experiment, time control of the medium was obtained by placing a 500  $\mu\text{m}$  thick gel membrane between a structured PDMS layer and a glass coverslip (Fig. 2.2A). Flow was established in the PDMS channel with a syringe pump at flow rates ranging between 20 and 50  $\mu\text{L}\cdot\text{min}^{-1}$ . A fluorescent glucose analog (2-NBDG) was added or removed from the flowing medium at a particular time point by switching a valve, thereby changing the composition of the flowing medium within seconds. The amount of 2-NBDG fluorescence was measured as a function of time by standard fluorescence microscopy using a

100X objective focused on the gel-glass interface. After the change of medium, the measured fluorescence signal rose in an approximately exponential fashion to the newly imposed steady-state value with a half-time of  $\sim 5$  min (Fig. 2.2B-C). Fits to the diffusion profile (Methods) yielded diffusion coefficients of  $4.0 \times 10^{-10} \text{ m}^2 \cdot \text{sec}^{-1}$  to  $5.3 \times 10^{-10} \text{ m}^2 \cdot \text{sec}^{-1}$ , comparable to the typical diffusion coefficient of small molecules in water ( $5.0 \times 10^{-10} \text{ m}^2 \cdot \text{sec}^{-1}$ ).

In the second experiment, we aimed to set up a spatial concentration gradient by placing a structured gel membrane between a glass slide and a flat PDMS layer, the latter containing inlet and outlet connectors (Fig. 2.2D). Liquid was pumped through the  $100 \mu\text{m}$  high channels molded into the polyacrylamide hydrogel at a rate of  $50 \mu\text{L} \cdot \text{min}^{-1}$ . One channel contained pure water, whereas the other channel contained an aqueous solution of fluorescein molecules. Diffusion of fluorescein into the polyacrylamide hydrogel, coupled with its removal at the adjacent channel, is predicted to create a linear concentration gradient in the space between the two channels [106]. We found that the spatial gradient reached steady state after  $\sim 1$  hr. Subsequently, we imaged the concentration profile at mid-channel depth. We observed a linear concentration gradient within the gel between the two channels as predicted by the theory (Fig. 2.2E-F) [106].

## 2.2.4 Carbon controlled growth of bacteria

We tested the use of the polyacrylamide hydrogels to create a microfluidic chemostat for the growth of *E. coli* bacteria (Fig. 2.1C). First, we used time-lapse phase contrast microscopy to visualize single *E. coli* cells growing on a simple flat polyacrylamide membrane while flowing minimal medium with abundant lactose. Cells divided for at least 8-9 generations into monolayered colonies (Fig. 2.3A). Colony growth into monolayer was most probably favored both by the imposed confinement and the observed preferential adhesion of the bacterial cells to the hydrogel rather than to the glass surface. In the absence of vertical overlap between cells, we could perform unambiguous determination of their outlines and determine the length of individual cells using custom image analysis software (Methods). The population growth, quantified as the sum of the length of all cells in the microcolony, showed that cells were growing exponentially (Fig. 2.3B, green trace) with a doubling rate of  $\sim 0.9 \text{ h}^{-1}$ . The single-cell analysis of cell growth indicated variability in growth rate within each colony. This variability was not correlated with the position within the colony (Fig. 2.3C), which strongly suggested it was rather caused by internal stochastic factors rather than a

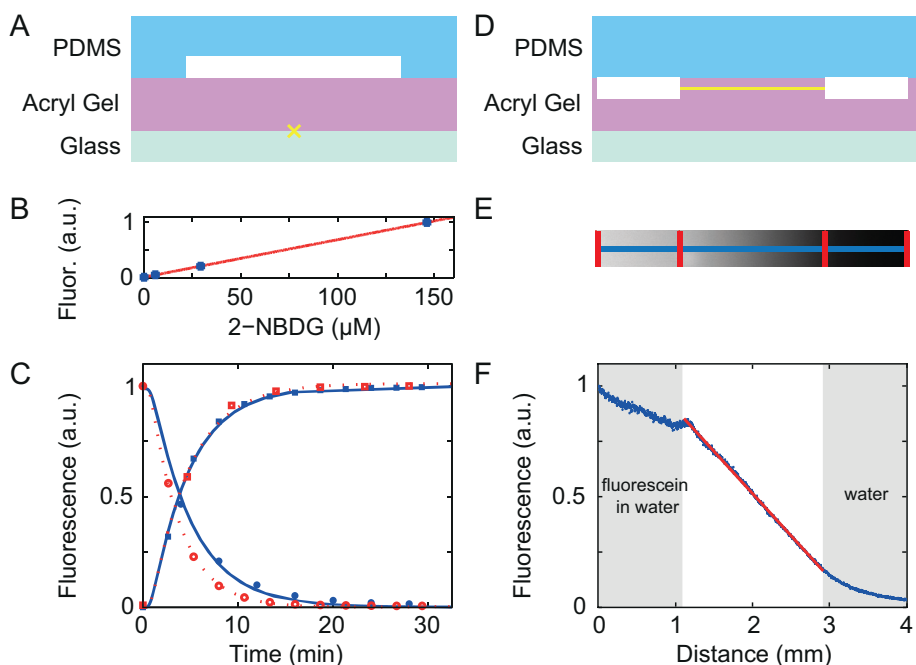


**Figure 2.2** Diffusion in unstructured and structured acryl gel membranes (A) Sketch of the flow cell device. An unstructured acryl gel (height  $500\ \mu\text{m}$ ) is sandwiched between a PDMS layer comprising a channel (in white, height  $113\ \mu\text{m}$ ), and a glass coverslip, similar to Figure 2.1A. (B) Fluorescence of the small dye 2-NBDG is proportional to its concentration in the flowing solution. (C) Dynamics of fluorescence after infusion (squares) or depletion (circles) of the dye 2-NBDG was measured at the gel-glass interface (yellow cross). Lines show fits to the 1D diffusion equation. Open symbols and dashed lines correspond to flow rates of  $50\ \mu\text{L}\cdot\text{min}^{-1}$ , closed symbols and solid lines to flow rates of  $20\ \mu\text{L}\cdot\text{min}^{-1}$ . (D) Sketch of the gradient generator device. A structured acryl gel (height  $1\ \text{mm}$ ) is sandwiched between a PDMS layer and a glass slide. Water containing  $3.5\ \mu\text{g}\cdot\text{mL}^{-1}$  fluorescein is flown through the left channel, while pure water is flown through the right channel, creating a concentration gradient within the gel. (E) Image of the fluorescence intensity profile at mid-channel height taken approximately 85 min after the flows were established (yellow line in (D)). Red lines indicate channel walls. (F) Fluorescence intensity profile (blue crosses) plotted versus distance (along blue line in (E)). The fluorescence intensity in the acryl gel in between the channels is linear (red line).

lack of uniformity in the environment.

Control of the growth rate of bacterial cells was demonstrated by exponential growth on minimal medium supplemented with various carbon sources (Fig. 2.3B). The population growth showed that cells grew at a constant rate in

each condition, yielding doubling rates of  $0.8 \text{ h}^{-1}$  for growth on maltose (Fig. 2.3B, red trace),  $0.6 \text{ h}^{-1}$  on lactate (Fig. 2.3B, yellow trace) and  $0.23 \text{ h}^{-1}$  on limiting lactose (Fig. 2.3B, blue trace). These values are in good agreement with our growth rate measurements in bulk (Fig. 2.8) and the relative quality of the different carbon sources ([120] and Methods). Growth on limiting lactose confirmed in particular that our nutrient free material is suitable for attaining and studying low growth rates.

To show the ability of our designs to study single-cell dynamics in changing environments, we performed a carbon shift (with the device of Fig. 2.1C), and monitored both growth and gene expression over time. We started from a single cell on a minimal medium containing lactose, and switched to a minimal medium containing glucose after three generations. Expression of the *lac* genes was measured with a GFP reporter inserted in the *lac* operon (see Methods). The *lac* genes control the import and metabolization of lactose and are induced during growth on lactose, but repressed when glucose is present.

We show the population-level dynamics in Fig. 2.3D. During growth on lactose, cells reached a steady growth rate of  $\sim 0.8 \text{ h}^{-1}$  and the mean fluorescence intensity of the microcolony over time was high, consistent with the full expression of the *lac* genes in all cells. Upon shifting to glucose, the growth rate was maintained at its pre-shift value during a delay of approximately 20 min, after which it increased abruptly to the higher glucose steady-state value of  $\sim 1 \text{ h}^{-1}$ . At the same time, the mean fluorescence started to decrease exponentially with a characteristic half-time of 70 min, close to the doubling time. This indicated the arrest of *lac* genes expression after the shift and a decrease in GFP per cell dominated by dilution [121], until attaining cellular auto-fluorescence levels after four generations. We performed single-cell analysis and observed significant variability between lineages related to stochastic factors both in genetic expression and growth (Fig. 2.3E), as previously described [29, 30].

Overall, we verified that the use of polyacrylamide gels allows precise determination of growth properties for given quality and abundance of nutrients in the media. We also tested the response of bacteria to a sudden change in the growth medium. Combined with quantitative movie analysis, we demonstrated that it was possible to measure growth and gene expression dynamics at the single-cell level with polyacrylamide based devices.

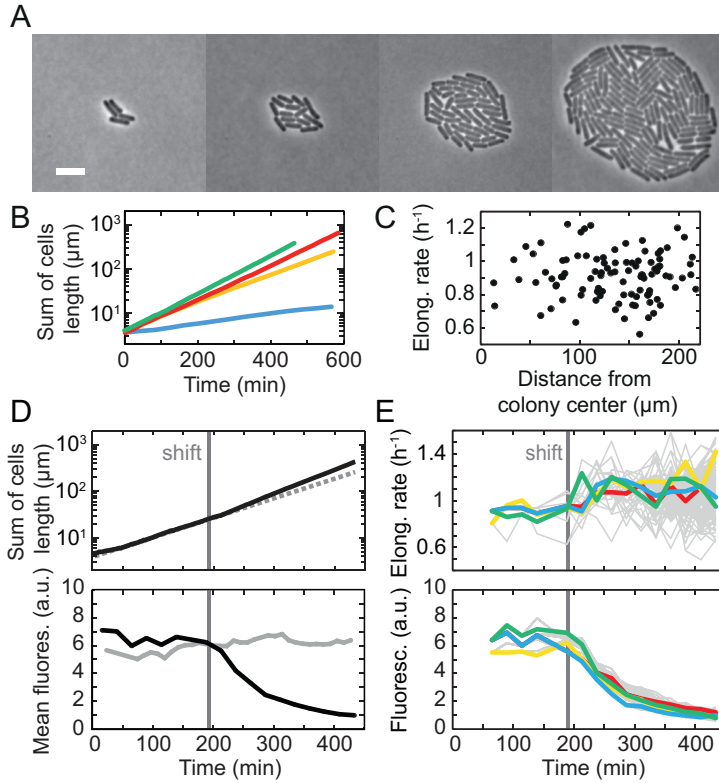


**Figure 2.3** Monitoring bacterial growth by time-lapse microscopy. (A) Phase contrast images of *E. coli* cells growing in minimal medium supplemented with lactose. Images were taken at 2 hrs intervals. White bar is 4  $\mu\text{m}$ . (B) Sum of cells length for microcolonies growing on minimal medium with lactose (green), maltose (red), lactate (yellow) and limiting lactose (blue) as sole carbon source. (C) Scatter plot of instantaneous growth rate and cell position within the microcolony, calculated 6.5 hrs after the start of the experiment. The cell position was calculated as the distance of the center of a cell to the arithmetic center of the microcolony. (D-E) Dynamics of growth and gene expression during shift from lactose to glucose. (D) Sum of cells length (top) and mean fluorescence intensity (bottom) of a microcolony. For comparison, fluorescence intensity for a microcolony growing only on lactose is shown in grey. (E) Elongation rates (top) and fluorescence levels (bottom) over time of all lineages within the microcolony. Selected lineages are highlighted in different colors. Note that for clarity the first cell cycle is not plotted.

## 2.2.5 Temporary induction of a growth arrest in yeast

We first checked that yeasts grew normally, both confined between an unstructured hydrogel monolayer and a glass cover slip and confined within microstructures such as channels or chambers in a device similar to Fig. 2.1A-B. When cells were confined between an unstructured flat hydrogel and glass, we could observe the constant exponential proliferation of fission yeast cells for more than 7 generations over 20 hrs (Fig. 2.4A). This corresponded to an average doubling time of 170 min at 32°C, in agreement with liquid culture growth rate in the same minimal medium. This indicated that the hydrogel imposed a mechanical pressure sufficient to confine the cells, but was soft enough to not perturb growth, most probably slightly deforming around the cells which have a 3-4  $\mu\text{m}$  diameter. We then grew yeast cells, confined in 3  $\mu\text{m}$  deep microstructures molded in the hydrogel. Timelapse imaging showed that colony expansion was constrained by the walls until the culture chamber was full (Fig. 2.4B).

We tested the ability of the microstructured membrane combined with a PDMS control channel on top (Fig. 2.1D) to control the chemical composition of the microenvironment, in this case by inducing microtubule depolymerization during a defined time window. In fission yeast cells, microtubules form 3-5 bundles composed of groups of 2-4 microtubules. These microtubules are involved in multiple biochemical pathways, notably the delivery of polarity factors essential for the control of cell growth [122]. After growing yeast cells for 2 generations, we supplemented the flowing medium with 50  $\mu\text{M}$  of the microtubule-destabilizing drug methyl-2-benzimidazole-carbamate (MBC). Within 5 min, fluorescently labeled microtubules disappeared in >80% of the cells (Fig. 2.4C). In the remaining fraction of cells, abnormally short microtubules were present, as already reported for MBC-treated fission yeast cells [123]. We observed that in the remaining fraction of the cells, microtubules were organized in mitotic spindles prior to addition of MBC, rendering them more stable. As expected, cell growth was halted in the absence of microtubules. After 60 min, the drug was removed from the flowing medium, leading to the reappearance of microtubules in >90% of cells within 5 min and inducing recovery of the growth process.

In conclusion, we have shown that yeast cells grow normally on polyacrylamide hydrogel membranes, and that colony expansion can be confined between a flat hydrogel membrane and a glass coverslip, or within a structured membrane. The membrane allowed for adding or removing a drug on a timescale of minutes.

## 2.2.6 Growth and development of spatially confined *Caenorhabditis elegans* larvae

We then tested whether our approach could be used to confine much larger, multicellular organisms. To that end, we monitored growth and development of single larvae of the nematode worm *Caenorhabditis elegans*, spatially confined to arrays of microchambers molded into polyacrylamide gel (Fig. 2.5A).

We grew *C. elegans* larvae by adding an individual *C. elegans* egg and sufficient *E. coli* bacteria as food source to each microchamber. We observed that eggs developed normally inside the polyacrylamide microchambers and that newly hatched larvae increased in length from about ~300  $\mu\text{m}$  directly after hatching to ~600  $\mu\text{m}$  over the course of 10-15 hrs (Fig. 2.5 A-B). All larvae stayed confined to the microchambers during the entire period of observation.

Development of *C. elegans* is divided in four larval stages, labeled L1 to L4, that are separated by molts during which a new cuticle is synthesized and old cuticle is shed. The molts are accompanied by a behaviorally quiescent state called lethargus. After 10-15 hrs, animals entered the lethargus accompanying the L1 molt (Fig. 2.5B), agreeing well with the observed duration of the L1 larval stage of ~15 hrs [99]. We observed that the start of the L1 molt correlated well with animal length. Note that the variability in the duration of the L1 stage we observed was mostly due to variation in animal length at the time of hatching. These results indicate that the development of L1 larvae occurred normally inside the microchambers.

## 2.3 Discussion

We have demonstrated the microfabrication of polyacrylamide membranes by soft lithography and used these to build controlled environments for the study of growing cells and organisms. While similar capabilities can be achieved with other techniques based on hydrogels, notably agarose gels, our method has several practical advantages. A major one is the advantageous mechanical properties of polyacrylamide, which allow easy handling of the gel both during microfabrication steps and experimental setup, especially compared to the classically used agarose layers which can easily tear. In addition, our method requires minimal investment in materials and technological infrastructure, as we used a protocol for fabrication of polyacrylamide hydrogels that is commonly



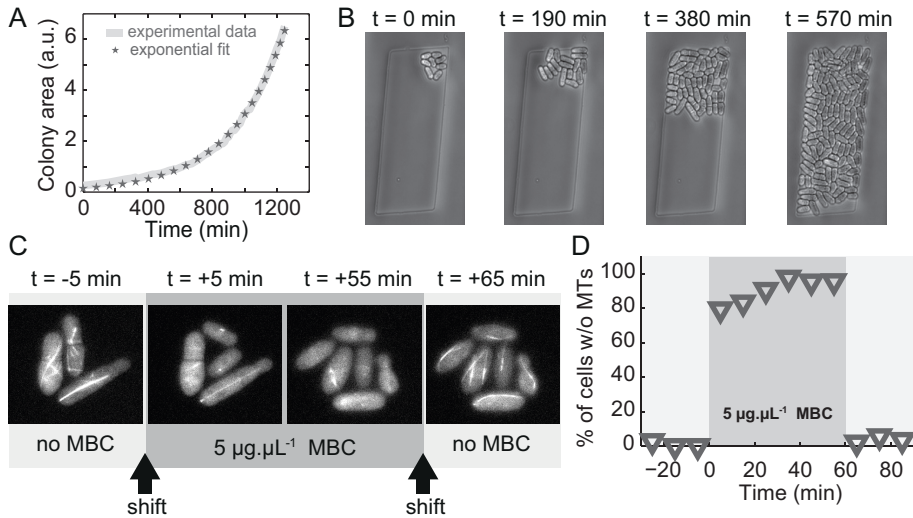


**Figure 2.4** Control of the environment of growing fission yeast colonies (A) Growth curve of the colony (area) obtained by a time-lapse experiment (blue) from 1 cell to 142 cells after 20 hrs. In red, single exponential fit of the growth rate with a doubling time of 240 min. (B) Phase contrast images of the fission yeast *S. pombe* growing in a microchamber. Fluorescent microscopy images of fluorescently labeled microtubules during treatment with the microtubule-inhibiting drug methyl-2-benzimidazole- carbamate (MBC). Before the injection of 5  $\mu\text{M}$  MBC, microtubules are observable in every cells ( $t = -5$  min). 5 min after the shift MT disappeared in more than 80% of the cells. MBC treatment lasts for one hour, over which MT assembly is not observed. Rapidly after the wash out of the drug, MTs reappeared in almost every fission yeast cells. (D) Percentage of cells without observable MTs in a time-lapse experiment, before, during and after microtubule depolymerization with 5  $\mu\text{M}$  of MBC.

used in biology laboratories for protein electrophoresis and only requires preparation of a solution that polymerizes at room temperature. Once polymerized, these membranes remain functional for months when stored in solution. In addition, the microfabrication step relies on a silicon mold that can be re-used many times.

We have proposed various devices that allow accurate spatio-temporal control of the environment. Control in time was achieved by diffusion through the gel into culture chambers that are otherwise entirely uncoupled from the flow in the PDMS channel. Diffusion coefficients of small molecules in the gel are close to their value in water, which combined with the possibility to build thin membranes allowed medium exchange with a characteristic time of 5 minutes. This response time is well suited for many applications that require the control of the growth and gene expression dynamics in micro-organisms such as bacte-

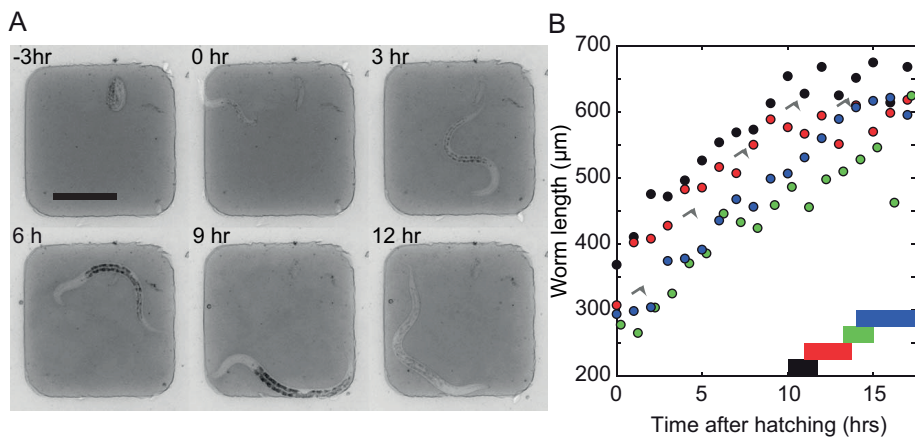


**Figure 2.5** *C. elegans* growth in microchambers. (A) Growth of a single *C. elegans* animal through the L1 larval stage constrained in a  $200 \times 200 \times 18 \mu\text{m}$  polyacrylamide microchamber filled with OP50 as source of food. Black bar is  $100 \mu\text{m}$ . Time is shown in hours after hatching. At 12 hrs after hatching the animal has entered the lethargus at the end of the L1 larval stage. (B) Worm length as a function of time after hatching. Different colors indicate animals grown in parallel on the same device. Horizontal bars show the duration of lethargus, ending with the molt at the start of the L2 larval stage. The markers indicated by the arrow correspond to the time points shown in (A).

ria or yeast, as these cellular responses typically need to be assessed on the time scale of several tens of minutes. We have demonstrated the creation of precisely controlled linear concentration gradients between continuously flowing solutions in channels embedded in a single gel layer. This method may be used to set up steeper gradients or more complex two-dimensional concentration patterns than conventional chemotaxis assays for which diffusion between PMDS channels is constrained to occur through a hydrogel layer in a third dimension [106]. We have demonstrated the potential of these devices to study dynamically the genetic or the morphologic responses to changes in growth medium or the addition of chemical inhibitors of cellular processes. In conclusion, these polyacrylamide-based devices are uniquely suited to study the response of diverse biochemical pathways to chemical perturbations. They are also of particular interest for studies on metabolism and growth as the polyacrylamide matrix is free of nutrients.

The physico-chemical properties of polyacrylamide layers are well suited for single-cell or organisms studies. In the case of bacteria, long-term growth in monolayers enabled convenient single-cell analysis. In the case of yeast cells, soft confinement by the membrane or by microstructures built within the hydro-

gel ensured localization of the colonies, while maintaining normal growth and morphological phenotypes without requiring the deposition of an additional soft layer on the glass [118].

This technology is also promising for the study of larger, multicellular organisms, such as *C. elegans*. In this context, polyacrylamide gels with microchambers provide two major advantages. First, they allow spatial confinement of these otherwise highly motile organisms, enabling time-lapse microscopy and parallel image acquisition without the use of anesthetic drugs [100] or automated tracking of individual animals [124]. Second, polyacrylamide hydrogels enable exchange of medium and waste products with the microenvironment of the animal.

Finally, the tunable mechanical properties of polyacrylamide hydrogels make them potentially highly useful for the culture of other cell types, given, for example, the exquisite sensitivity of mammalian cells to the mechanical properties of their support [93]. The potential to embed microfabricated polyacrylamide membrane in complex modular designs offers exciting opportunities to develop precisely controlled environments for cell biology studies and tissue engineering.

## 2.4 Materials and methods

### 2.4.1 Supplementary figures

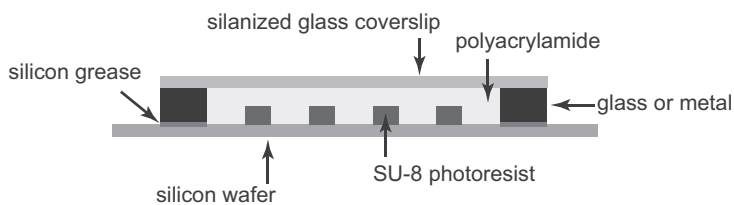


**Figure 2.6** Molding of the polyacrylamide gel. The acrylamide solution is injected with a pipette within the cavity created by the wafer with the photoresist pattern stuck with silicon grease to a glass or metal contour of desired height. A silanized coverslip is then added on top of the cavity and polymerization occurs at room temperature for 2 hrs.

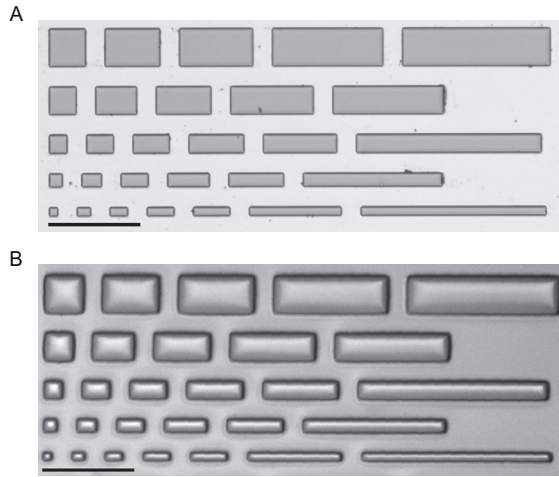


**Figure 2.7** SU-8 pattern on a wafer and molded acrylamide gel. (A) Image of a silicon wafer micropatterned with SU-8 photoresist. (B) Structures shown in (A) have been molded in a polyacrylamide gel. Scale bars 100  $\mu\text{m}$ . Smallest features are 10  $\mu\text{m}$  wide.

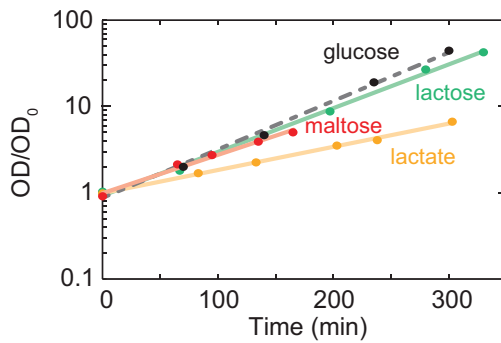


**Figure 2.8** Growth rates in batch cultures. Optical density at 550 nm (normalized by the exponentially fitted OD at  $t = 0$ ) versus time for batch cultures of MG1655 cells growing in minimal medium with abundant (0.1%) glucose (dotted line), lactose (green), maltose (red) and lactate (yellow) as sole carbon source. Exponential fits to the experimental data points (lines) yielded growth rates of  $1.12 \text{ h}^{-1}$  on glucose,  $1.01 \text{ h}^{-1}$  on lactose,  $0.88 \text{ h}^{-1}$  on maltose and  $0.54 \text{ h}^{-1}$  on lactate, comparable to those obtained for cells growing in the microfluidic device (Fig. 2.3B and D).

## 2.4.2 Fabrication of the microfluidic device

Master molds have been realized on silicon wafers with spin-coated SU-8 epoxy resins (MicroChem) of different viscosities (models 2005, 2025 and 2100) resulting in heights of 3  $\mu\text{m}$  for the yeast chambers, 18  $\mu\text{m}$  for the worm chambers and 100  $\mu\text{m}$  for the gradient assay. No specific wetting treatment was done to the surface of the wafer. For the polyacrylamide gel, we used a 37.5:1 ratio of acrylamide/bis-acrylamide (Bio-Rad) with a final concentration of 10%. Polymerization was initiated by the addition of 0.1% of ammonium persulfate (Sigma) and 0.1% of TEMED (Sigma). The mixture was poured in a mold consisting of a cavity made of a machined glass or aluminum slide of thickness varying between 150  $\mu\text{m}$  and 1 mm, glued to the wafer or to a simple silanized glass slide with vacuum silicon grease. A silanized glass coverslip was deposited on top and the solution was left to polymerize for about 2 hrs. The polyacrylamide membrane was then cut and transferred in deionized water for conservation. The PDMS (Sylgard 184, Dow Corning) channel was molded on a silicon wafer with SU-8 according to the protocol provided by the resin manufacturer (MicroChem) and consisted of a 113  $\mu\text{m}$  high and 3 mm wide channel comprising pillars to ensure uniformity of the pressure applied on the polyacrylamide membrane. Mechanical clamping of the whole device was performed by a homemade metal holder with 4 screws, comprising openings on the bottom for microscopy acquisition and on the top for illumination and the tubing.

## 2.4.3 Experimental devices

The flow was externally driven with syringe pumps (ProSense, NE-1000 and NE-300) connected to the microfluidic device by polyethylene tubing of 0.58 mm internal diameter (Smiths medical International Ltd.). When using a PDMS channel, the device was degassed 1 hr in low vacuum prior to flow to avoid trapped air bubbles. Switches were performed by a manual valve (Hamilton, HV 4-4). All experiments have been performed with an inverted microscope (Nikon, TE2000) embedded in a temperature-controlled incubation chamber (Solent), equipped with cooled CCD camera (Photometrics, CoolSnap HQ), xenon lamp with liquid light guide (Sutter, Lambda LS), GFP filter set (Chroma, 41017), computer-controlled shutters (Sutter, Lambda 10-3 with SmartShutter) and automated stage (Märzhäuser, SCAN IM 120 x 100). The microscope control software used was MetaMorph.

## 2.4.4 Bacteria

Growth experiments were performed using derivatives of *E. coli* MG1655 (*rph-1 ilvG- rfb-50*). To measure the expression of the *lac* operon, *lacA* was replaced with *GFPmut2* [125] and chloramphenicol resistance using the protocol described by Datsenko and Wanner [126] (gift of M. Ackermann).

Cells were grown in M9 minimal medium (47.7 mM Na<sub>2</sub>HPO<sub>4</sub>, 25 mM KH<sub>2</sub>PO<sub>4</sub>, 9.3 mM NaCl, 17.1 mM NH<sub>4</sub>Cl, 2.0 mM MgSO<sub>4</sub>, 0.1 mM CaCl<sub>2</sub>) (all the chemicals were provided by Merck), with 0.2 mM uracil (Sigma), supplemented with 0.1% (w/v) lactose (Fluka), maltose (Sigma), lactate (Sigma) and 0.001% (w/v) lactose in the limiting case. Note that adding uracil compensates for intrinsic pyrimidine starvation of the MG1655 strain [127] and accounts for the typically 15% higher growth rates measured in our study compared to Beg *et al.* [128].

Cells were initially inoculated from glycerol stock in TY medium and grown until the OD > 0.02 and next diluted in M9 medium with 0.1% (w/v) lactose for growth overnight. The following day, the overnight culture was diluted in M9 medium 0.1% (w/v) lactose (OD ~0.005) and transferred to the microfluidic chamber. 10 μL of culture were deposited on a glass coverslip, the polyacrylamide gel membrane was put on top and left to dry for about 2 min before the setup was assembled. All these steps were performed at 37°C.

Cell imaging was performed with a 100X oil objective (Nikon, Plan Fluor NA 1.3). An additional intermediate 1.5X magnification was used, resulting in images with pixel size corresponding to a length of 41 nm. Phase contrast images (300 ms exposure time with GIF filter) were taken every 1 to 2 min; fluorescence images every 25 min (1000 ms exposure) or 15 min (500 ms exposure). Data analysis is detailed in section 2.4.8.

## 2.4.5 Yeasts

Standard methods for *S. pombe* media were used throughout. For growth experiments, we used wild type fission yeast (*PT286 h- ade6-M216 leu1-32 ura4-D18*). For the drug shift experiment, we used a strain expressing GFP tubulin (*DB 871 h90 nmt1-GFP-tub:lys1+ leu- ura-*). Fission yeast cells were grown overnight in Edinburgh Minimal Medium (EMM) liquid culture to ensure an exponential growth. 2 μL of 10X-concentrated culture were deposited on a polyacrylamide gel membrane that had been incubated in EMM medium. A clean coverslip was put on top of it. All these steps were performed at room temperature, while the

experiment was performed at 32°C. Cells were imaged through a 40X objective oil immersion lens (Nikon, NA 1.0). Colony area was measured with ImageJ (<http://rsbweb.nih.gov/ij>) software. Fit of the colony growth was done with Matlab (MathWorks). Microtubules detection was performed visually.

## 2.4.6 Nematodes

The wild-type (N2) *C. elegans* strain was grown on NGM agar plates covered with *E. coli* OP50 as food source, following standard protocols [129]. Before sample preparation, the polyacrylamide microchamber array was soaked overnight in M9. Under a stereomicroscope, OP50 bacteria and a single embryo at the three-fold stage, between 550 and 840 min after fertilization [99], were transferred to each individual microchamber, using a worm pick to transfer bacteria and an eyelash attached to a Pasteur pipette to transfer eggs. Images of individual microchambers were captured every 15 min using a 10X Nikon objective (NA 0.30). L1 larvae hatched and developed at room temperature (22°C). Worm length was quantified as a function of time with a 1 hr interval. Entry into and exit from the L1 molt was monitored by reduction in movement during lethargus, decrease in contrast in the transparency of the animal's body due to synthesis of the new cuticle and finally the shedding of the old cuticle.

## 2.4.7 Fitting of diffusion coefficients in Figure 2.2C

The following formula was taken from [130]:

$$C = C_0 \left( \sum_{n=0}^{n_{\max}} -1^n \operatorname{erfc} \frac{(2n+1)l-x}{2\sqrt{Dt}} + \sum_{n=0}^{n_{\max}} -1^n \operatorname{erfc} \frac{(2n+1)l+x}{2\sqrt{Dt}} \right)$$

where  $l = 500 \mu\text{m}$  (width of system),  $x = 0 \mu\text{m}$  (position of measurement),  $C$  is concentration and  $t$  is time, values taken from Figure 2.2C. Fitting was performed with Matlab with  $n_{\max} = 3$ .  $C_0$  (maximum concentration) and  $D$  (diffusion coefficient) were used as fitting parameters.

## 2.4.8 Data analysis

The data analysis described in this section was used in all the other experiments of this thesis. Images were analyzed with a custom Matlab (MathWorks) program based on a software from Elowitz lab (Schnitzcells) [131]. Cell outlines were determined automatically by applying a Laplacian of Gaussian filter on the phase contrast images and cutting clumps of cells based on concavity and phase contrast maxima (Fig. 2.9A). All cell segmentations were visually checked, and if necessary corrected by forcefully running the same analysis procedures at user-defined locations. After tracking, a complete history of each cell lineage in the microcolony was unambiguously determined up until the microcolony expanded beyond the field of view, or when a second layer of cells would form. Generally this meant that the history of 9 generations of lineages, consisting of ~500 complete cell cycles from a single microcolony, could be determined in one experiment.

### Growth rate at sub-cell-cycle resolution

Growth rates were determined from exponential fits of cell length over time. Cell lengths were measured with sub-optical-resolution precision by analysis of phase contrast intensity profiles along the cell axis [132]. The cell axis was determined by fitting a third degree polynomial  $f(x)$  through the silhouette of the cell (Fig. 2.9A-B), as to fit both straight and curved cells (which are observed at very low growth rates). After determination of the pole positions ( $x_0$  and  $x_1$ ) on the axis (Fig. 2.9C), the cell length  $L$  was calculated by numerical integration of:

$$L = \int_{x_0}^{x_1} \sqrt{1 + f'(x)^2}$$

Growth rates ( $\mu$ ) were obtained by calculating the elongation rate with an exponential fit of length over time (see Fig 2.8I):

$$L(t) = L_0 e^{\mu \cdot \ln(2) \cdot t} = L_0 2^{\mu \cdot t}$$

Cell doubling times ( $T_d$ ) are  $T_d = 1/\mu$ . Sub-cell-cycle growth rates were determined by fitting length measurements within a time window (corresponding to a third of the cell's mean doubling time) centered at the time points when fluo-



rescence images were taken. For time points at the end of a cell cycle where the time window includes a cell division, fitting was performed using extrapolated length values from summation of the lengths of the two daughter cells. Vice versa, for those time points at the beginning of the cell cycle, half of the length of the mother cell ( $L_m$ ) was used with a correction for asymmetric division lengths between the cell ( $L_0$ ) and its sister ( $L_{s,0}$ ):

$$L(t) = \frac{L_0}{L_0 + L_{s,0}} L_m(t)$$

### Protein concentration and production rate

Fluorescence images were corrected for camera noise and uneven illumination of the sample, using a background image ( $I_b$ ) and a shading image ( $I_s$ ). Given the original image  $I$ , the calibrated output image  $I_c$  is given by:

$$I_c = \frac{I - I_b}{I_s - I_b}$$

The image was further enhanced by deconvolution using Matlab's Lucy-Richardson algorithm in combination with a point-spread function for our imaging system (experimentally determined using 0.02  $\mu\text{m}$  sized FluoSpheres from Invitrogen, see Fig. 2.9E-G).

The total fluorescence of each cell was determined by extracting those pixels that were within the cell outline. The protein production rate was then measured by taking the slope of the best linear fit over the total fluorescence signal over three consecutive time points.

To obtain protein concentrations from fluorescence images, one generally divides the cell's total fluorescence by its size. The size measurement, however, is also used for calculation of the growth rate. In order to avoid artificial correlations between these two measurements, we determined the protein concentration independent of cell size. The cell mean fluorescence was calculated by averaging pixels within 0.2  $\mu\text{m}$  of the cell axis, but more than 0.3  $\mu\text{m}$  away from the cell poles (Fig. 2.9G). The protein concentration was calculated from this value by subtracting background fluorescence (determined from pixels outside microcolony) and autofluorescence (determined from fluorescence of wild-type MG1655).

In order to correct measured parameters for cell-cycle phase effects, we first calculated the cell phase at each time point, as a linear function in time from

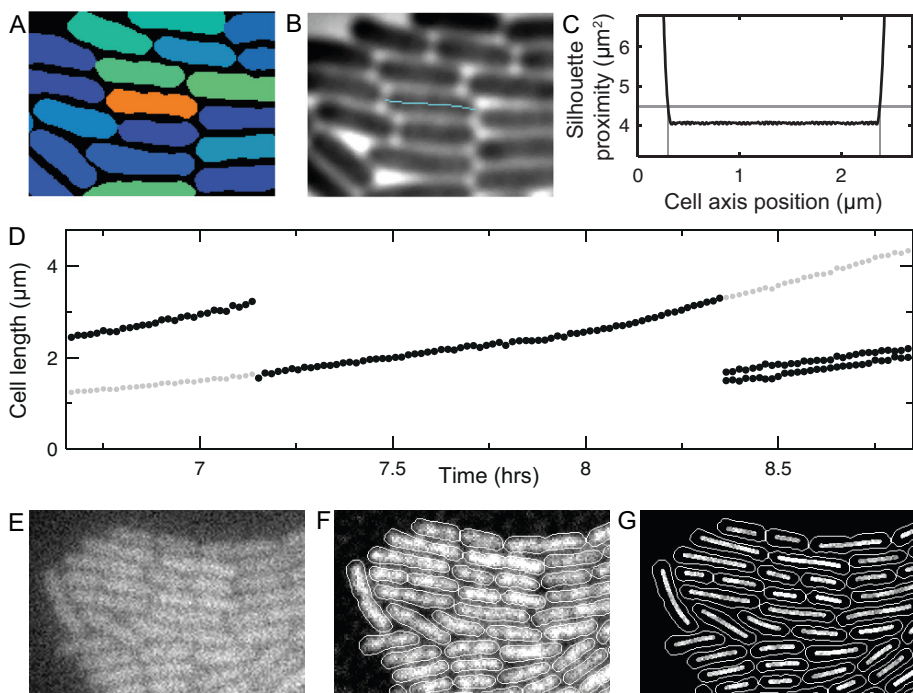


**Figure 2.9** Determination of cell length and enzyme concentration. (A) Segmented cell silhouettes are obtained by applying a Laplacian of Gaussian filter on phase contrast images. (B) The cell axis is determined by fitting a third degree line through the silhouette. (C) Cell length determination. We compute the distances between points on the cell axis and the closest 25 segmentation pixels. The sum of these distances squared, here termed the silhouette proximity, is plotted for points along the cell axis. In the center of the cell silhouette or mask, the silhouette proximity consistently remains at  $4.06 \mu\text{m}^2$ , but near the cell poles it rapidly increases. The location of the cell poles was taken at silhouette proximity of  $4.47 \mu\text{m}^2$ . (D) Elongation rate of a single cell. The length of a single cell, its parent and its offspring plotted over time (dark circles). Instantaneous exponential elongation rate is determined by fitting an exponential to this data for a fraction of the cell cycle. At the beginning and end of each cell cycle, length data of the parent or the offspring are used for this fitting process (grey circles, see text). (E) Initial fluorescence image. (F) Image after background correction, shading correction and deconvolution by a point spread function. Total cell fluorescence is determined as the sum of fluorescence values within the cell silhouette. (G) To accurately determine the cellular fluorescence intensity that reports for the enzyme concentration, we averaged the fluorescence values of pixels within a box of fixed width and equidistant length from the poles inside the cell perimeter.

0 at the cell's birth to 1 at its division. Next, the dependency of the parameter on the phase of the cell cycle was determined by a fit with a 3<sup>rd</sup> degree polynomial using all data points from a microcolony experiment. We subtracted the deviation of the fitted line from the cell cycle average at the phase for each data point. We used this method to normalize the growth rates, protein concentration and protein production rates that were used for correlation calculations in chapter 5 of this thesis.

*I would like to thank Daan Kiviet for developing our custom image analysis software, as well as Philippe Nghe and Noreen Walker for further improvements on the algorithm.*



## Single-cell dynamics reveals sustained growth during diauxic shifts

3

*Stochasticity in gene regulation has been characterized extensively, but how it affects cellular growth and fitness is less clear. We study the growth of *E. coli* cells as they shift from glucose to lactose metabolism, which is characterized by an obligatory growth arrest in bulk experiments that is termed the lag phase. Here, we follow the growth dynamics of individual cells at minute-resolution using a single-cell assay in a microfluidic device during this shift, while also monitoring *lac* expression. Mirroring the bulk results, the majority of cells displays a growth arrest upon glucose exhaustion, and resume when triggered by stochastic *lac* expression events. However, a significant fraction of cells maintains a high rate of elongation and displays no detectable growth lag during the shift. This ability to suppress the growth lag should provide important selective advantages when nutrients are scarce. Trajectories of individual cells display a highly non-linear relation between *lac* expression and growth, with only a fraction of fully induced levels being sufficient for achieving near maximal growth. A stochastic molecular model together with measured dependencies between nutrient concentration, *lac* expression level, and growth accurately reproduces the observed switching distributions. The results show that a growth arrest is not obligatory in the classic diauxic shift, and underscore that regulatory stochasticity ought to be considered in terms of its impact on growth and survival.*

## 3.1 Introduction

In the presence of two carbon sources, bacterial cells may either metabolize them both at the same time, or first use one and then the other. The latter strategy has been termed diauxic growth [133]. A classical example is the growth of *E. coli* on a mixture of glucose and lactose, which is characterized by initial rapid growth on glucose, followed by a phase of arrested growth when glucose is depleted, until the *lac* enzymes are expressed that allow growth on lactose [134]. Studies of glucose-lactose diauxie have led to many key discoveries on biological regulation, ranging from the existence of regulatory proteins and operator regions [5] to catabolite repression [135]. More generally, nutritional shifts experiments have revealed the dynamic changes of key classes of cellular components, such as protein, DNA, and ribosomes [68, 71, 136-138]. However, our understanding of the cellular growth response to environmental change has been obtained primarily using bulk techniques [68-73] that measure the growth rate of the population as a whole. As a result, it is unclear how the growth of individual cells responds during diauxic shifts.

This question is central to understanding how cells compete. Cellular heterogeneity within populations could critically affect the ability to consume limited resources before they are exhausted by competitors, which can be decisive for survival. For instance, populations could respond fast by following a bet-hedging strategy, in which the expression of genes is randomly turned on, thus generating sub-populations that are primed for diverse future environmental changes [139]. On the other hand, stochasticity in regulatory control could be disadvantageous, as the costs of spuriously expressing genes may lower the rate of growth and reproduction [140]. Stochasticity in gene regulation may thus have important consequences for fitness, and therefore, shed a new light on the function of regulatory systems in complex natural environments, as well as their historical evolutionary origins.

The advent of single-cell techniques has in recent years quantitatively characterized the stochastic nature of gene expression [36, 40, 141, 142]. The *lac* system in particular has been shown to display stochasticity in expression [40], as well as in the underlying repressor-operator association and dissociation events [29]. In response to changes in artificial inducer, *lac* expression was shown to exhibit bistability [143, 144] and heterogeneity in the timing of induction [30]. However, it remains poorly understood how cellular growth is affected. To address this issue, we have studied the dynamics of diauxic growth at the single-cell level. We used a microfluidic approach to control glucose and lactose levels in the

cellular environment, accurately determined cellular lengths at high time resolution, and used GFP labeling to monitor expression of the *lac* operon.

## 3.2 Results

### 3.2.1 Population growth and expression dynamics during diauxie

To control the environment, we used a microfluidic device in which microcolonies of cells were growing between a membrane and a coverslip [101, 118] (Fig. 3.1A). By flowing different media above the permeable membrane, cells were exposed to a variable but spatially uniform environment. We measured the depletion of a fluorescent glucose analog from the cellular area, upon instantaneous switch to plain minimal medium, and found an exponential decay with a half-life of  $\sim 5$  min (Fig. 3.1B). Starting with one or two cells, growing microcolonies were monitored by phase-contrast microscopy for 8–9 generations, yielding 200 to 500 cells for each microcolony at the end of the experiment. The lengths of the cells were determined using phase contrast images acquired every 1 to 2 min, and custom image analysis software (see section 2.4.8). We started by characterizing the steady-state growth limitations, using fixed external nutrient concentrations (Fig. 3.1C and D). The data for both glucose and lactose were consistent with the Monod relation [133], indicating characteristic limiting concentrations of  $5 \mu\text{M}$  for glucose and  $70 \mu\text{M}$  for lactose. For glucose a value of  $\sim 1 \mu\text{M}$  has been found previously in batch cultures [145]. Induction with artificial inducers IPTG and TMG has been shown to lead to bistability in *lac* expression [29, 143, 144]. Here we did not observe bistability, thus confirming theoretical predictions that natural inducers do not give rise to bistability because they are actively degraded by metabolism [146, 147].

We then subjected cells to an environmental switch after 4–5 generations. Switching from glucose to lactose or from a mixture of glucose and lactose to lactose only, gave similar results as expected (see Appendix, Fig. 3.9). We used a starting glucose concentration at which the growth rate is maximal ( $555 \mu\text{M}$ , Fig. 3.1C). The population growth, quantified by adding the lengths of all cells within the microcolony, displayed the prototypical diauxic growth behavior (Figure 3.2A): first a phase of rapid exponential growth, followed by a lag phase, after which growth restores to exponential growth. The two exponential growth rates matched the values for the fixed glucose and lactose media ( $\sim 1$  doubling/hr, and  $\sim 0.8$  doubling/hr respectively). The duration of the lag phase was about 20 min,

comparable to batch culture data [134, 148]. Expression of the *lac* operon was monitored using a GFP reporter (see Appendix). The mean fluorescence intensity within the microcolony in the first exponential phase was near the cellular auto-fluorescence, consistent with expected repression of the *lac* operon when growing on glucose [134]. Upon the shift, the mean fluorescence increased and reached a steady state level on a timescale that is similar to that observed for the growth rate (about 300 min, Fig. 3.2B). The fluorescence started to increase rapidly 30 min after the shift, though the precise onset of expression increase could not be determined precisely because the rise was smooth. Overall, these observed population dynamics of growth and expression are consistent with previous results from batch experiments.

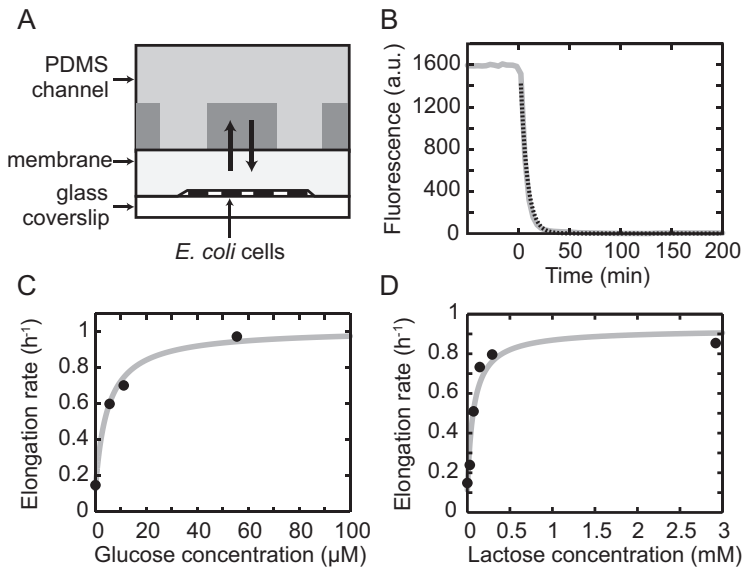


**Figure 3.1** Experimental setup. (A) Layout of the microfluidic device. The cells are growing between a glass coverslip and a polyacrylamide gel membrane. The medium reaches the cells and is exchanged by diffusion through the membrane. (B) Estimation of the fluid exchange time by means of the fluorescent glucose analog 2-NBDG ( $30 \mu\text{M}$ ). 2-NBDG is removed at time zero. The experimental curve is shown in red; the exponential decay fit is shown in black. (C-D) Mean growth rate of *E. coli* in steady-state growth in minimal media containing glucose (C) or lactose (D) as the only carbon source. In both cases, the fitted line is a Monod growth curve taking into account a non-zero growth rate on contaminants.



### 3.2.2 Growth dynamics in single cells during diauxie

We followed the growth of individual cells during the diauxic shift by determining their length over time. The instantaneous growth rate was determined at sub-cell cycle resolution by fitting the cell length over time to an exponential function. We observed no significant changes in cell width during the experiment. Cells within one colony displayed diverse growth behaviors (Fig. 3.2C and D). For the majority, traces of length versus time showed a sharp transition from the glucose growth rate (1.0 doubling/hr) to a low growth rate (between 0.2 and 0.6 doubling/hr), followed by a smoother transition to the lactose growth rate (0.8 doubling/hr). The low growth rate was similar to growth in media without any added carbon sources, which we could observe either in constant conditions (Fig. 3.1C and D), or when switching from glucose to a medium without added carbon sources (data not shown). These experiments suggested the intermittent growth at low rate was supported predominantly by metabolism of contaminants in the media, which unlike in batch cultures are continuously replenished in these experiments. Other minor contributions to growth after the shift could potentially come from internal cellular glucose reserves, residual glucose that was not depleted, and from lactose metabolized by leaked *lac* enzymes produced at low repressed levels. The length analysis sometimes displayed measurement artifacts at cell division, but their amplitude was small compared to the general trend and therefore did not affect the growth analysis (Fig. 3.2C, red). The data thus showed that the lag phase did manifest itself at the single-cell level.

To characterize the variability in growth dynamics, we determined the moment of growth decrease ( $\Delta T_{\mu_1}$ ) and restoration ( $\Delta T_{\mu_2}$ ). Both are quantified relative to the moment of switching the fluid flow, which we refer to as the shift time. The difference between  $\Delta T_{\mu_2}$  and  $\Delta T_{\mu_1}$  is a measure for the duration of the lag phase in individual cells. We found that  $\Delta T_{\mu_1}$  and the duration of the lag phase are not significantly correlated ( $r^2 \approx 0.01$  and p-value = 0.104, N = 185), suggesting that the growth decrease and the growth restoration are independent processes.  $\Delta T_{\mu_1}$  was narrowly distributed close to zero (mean of the distribution: 13 min), which shows the growth process responds rapidly to the glucose decrease (Fig. 3.3A).  $\Delta T_{\mu_2}$  on the other hand displayed a broad and asymmetric distribution that extended to lag times of up to hundreds of minutes (79 min on average) (Fig. 3.3B). A small fraction of lineage, ~5%, even failed to resume exponential growth within the timescale of the experiment. These delays thus exceed by far the average lag time of 20 min. This broad distribution of lag times suggests that escape from lag is strongly affected by the timing of stochastic internal cel-

lular events. We did not find correlations between progression into the cell cycle and the timing of the growth transitions ( $r^2 \approx 0.03$ , p-value = 0.02 for growth decrease;  $r^2 \approx 0.001$ , p-value = 0.7 for growth recovery,  $N = 185$ ).

Interestingly, not all cells showed a lag phase. Some cells displayed no discernible decrease in growth rate (15% of all traces) (Fig. 3.2D), in contrast with the abrupt entry into lag seen in the other cells. The absence of a lag phase did not appear to be related to correlations with the cell cycle, or the position of the cell within the microcolony (see Appendix, Fig. 3.8). The  $\Delta T_{\mu_2}$  distribution extended monotonically down to zero, which suggested that the cells without lag do not represent a distinct sub-population (Fig. 3.3B). To understand the origins of this lack of a lag phase in some cells, information on the dynamics of *lac* operon expression is required.

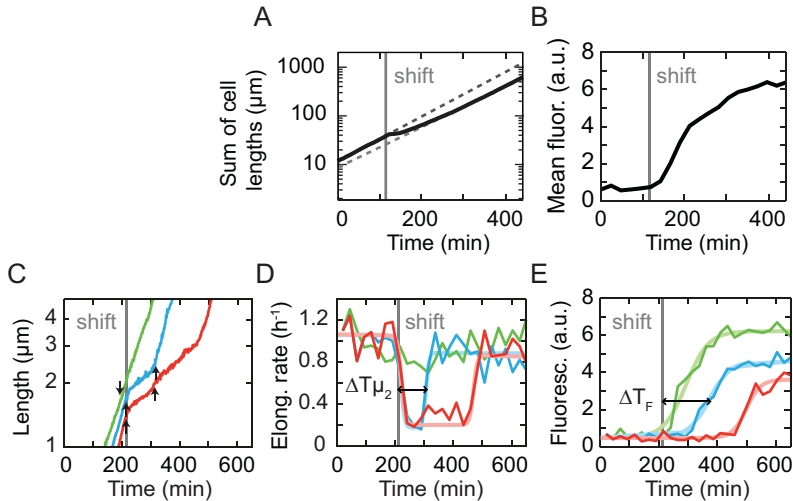


**Figure 3.2** Dynamics at the population level and in single cells. (A) Growth curve for a typical microcolony, indicating the sum of all cell lengths within the colony. (B) Mean fluorescence intensity (per unit area) within cells, averaged over a microcolony. (C) Single-cell length over time for three different lineages, representing cases with no growth rate decrease (green), a lag phase (blue) and a longer lag phase (red). Arrows indicate cell division events. The curves are vertically shifted for clarity. (D) Elongation rates obtained by exponential fits to the length data at sub-cell cycle resolution. Drawn lines are fitted parameterized functions.  $\Delta T_{\mu_2}$  is the time difference between the time of shift and the half maximum to growth recovery after shift. (E) Fluorescence levels for the three lineages in (C) and (D). Drawn lines are fitted parameterized functions.  $\Delta T_F$  is the time difference between the time of shift and the half maximum to induction after shift.

### 3.2.3 Correlations between growth and expression in single cells

We determined the mean fluorescence per unit area within single cells as a measure for the *lac* operon expression. The fluorescence versus time for individual lineages had a sigmoidal shape: a low level close to the background during growth on glucose, followed by a rise some time after the shift to lactose, until a constant steady-state level was achieved on the order of the doubling time (Fig. 3.2E). However, different lineages displayed significant variability. For instance, the fluorescence level at the end of the experiment varied by up to 40% (see Fig. 3.2E), reflecting heterogeneity in protein production between cells [40] as well as incomplete entry into steady state for some lineages. This final fluorescence level did not correlate significantly with the timing of induction ( $r^2 = 0.04$  and  $p$ -value = 0.003,  $N = 216$ ).

The timing of induction was also variable, as observed previously for the *ara* system [149]. The time between the shift and the moment at which fluorescence reaches half-maximum, which we here denote as  $\Delta T_p$ , was distributed with a width and shape similar to that of  $\Delta T_{\mu_2}$  (133 min on average) (Fig. 3.3C). We found  $\Delta T_F$  and  $\Delta T_{\mu_2}$  to be strongly correlated (Fig. 3.3D,  $r^2 = 0.85$ ,  $p$ -value < 0.001). This correlation is directly evident in the individual traces (Fig. 3.2C-E), where the red lineage displayed both a long growth arrest and a long induction delay, while the blue lineage with a smaller growth arrest exhibited a correspondingly smaller induction delay. The correlations also indicated that  $\Delta T_F$  was systematically larger than  $\Delta T_{\mu_2}$ , which we will address below. Overall, these data are consistent with a simple model in which the lag phase is caused by the *lac* operon being in the repressed state, and exit out of the lag phase is triggered by the stochastic *lac* induction.

However, this model did not explain the sustained growth. In particular, at the moment of glucose exhaustion ( $\Delta T_{\mu_1}$ ) the *lac* operon in these cells was still 'off', with expression at low repressed levels ( $N = 31$ , mean fluorescence 15 min after the time of shift:  $0.76 \pm 0.34$  (SD) a.u.). While we did not observe spatial heterogeneity of nutrients, for instance when using the fluorescent glucose, we cannot formally exclude that some spatial differences in the precise moment of glucose exhaustion occur. However, delayed glucose exhaustion should merely delay all events, including the moment at which the repressible effect of glucose is alleviated (catabolite repression). Hence, while spatial nutrient inhomogeneity could lead to growth arrests occurring at different times for different cells, it does not explain the absence of a growth arrest. The fluorescence traces also showed no sign of *lac* bistability, where the *lac* operon spontaneously switches between

repressed and induced expression levels, as has been observed for artificial inducers that are not metabolized [30, 32, 143]; bistability is thus also excluded as the cause of sustained growth. It has also been shown that the moment of *lac* induction upon a change in the artificial inducer TMG depends on the *lac* expression level before the change [30]. Hence we wondered whether the leaky stochastic expression of the repressed *lac* operon [40, 48], could underlie the variability in growth responses. If so, the *lac* expression level before the shift should correlate with  $\Delta T_F$ . However, such a correlation is difficult to detect, as the measured expression level during glucose growth is similar to the autofluorescence of wild-type cells. Nonetheless, the mean fluorescence 120 min before the shift did exhibit a weak but significant correlation with  $\Delta T_F$  ( $r^2 \approx 0.08$  and p-value  $< 0.001$ ,  $N = 216$ ). This result suggests that the sub-population of cells exhibiting sustained diauxic growth originated from pre-existing variations in expression that had developed stochastically during glucose growth.

While the data supported the idea that expression variability caused the observed differences in the growth dynamics of individual cells, a number of questions remained unanswered. For instance, how can the low leaky expression when glucose is exhausted be sufficient to maintain the growth rate at high levels, and why does growth restoration seem to precede induction? The latter is seen by  $\Delta T_F$  being systematically larger than  $\Delta T_{\mu_2}$  by up to hundreds of minutes (Fig. 3.2D), and hence cannot be explained by the  $\sim 10$  min GFP maturation time [149]. To address these questions we have developed a stochastic model, which is detailed in the next section.

### 3.2.4 Stochastic model of diauxic growth

Diauxic growth has been studied extensively using mathematical models [150-154]. With the aim to gain intuitive insight into the main features of observed heterogeneity, we developed a minimal stochastic model that focuses on key features and neglects various known details (Fig. 3.4A; see Appendix for complete description). For instance, for simplicity we considered the stochastic binding and dissociation of repressor at a single operator site and neglected other operator sites, as well as stochasticity arising from variabilities in the *lac* repressor levels [23]. The free and bound operator states yielded respectively a high and low rate of stochastic transcription events, with the latter resulting from brief partial repressor dissociations. Cellular metabolism and growth depended on *lac* expression through lactose import and metabolism, following deterministic Michaelis-Menten kinetics and using the experimentally determined dependence of growth

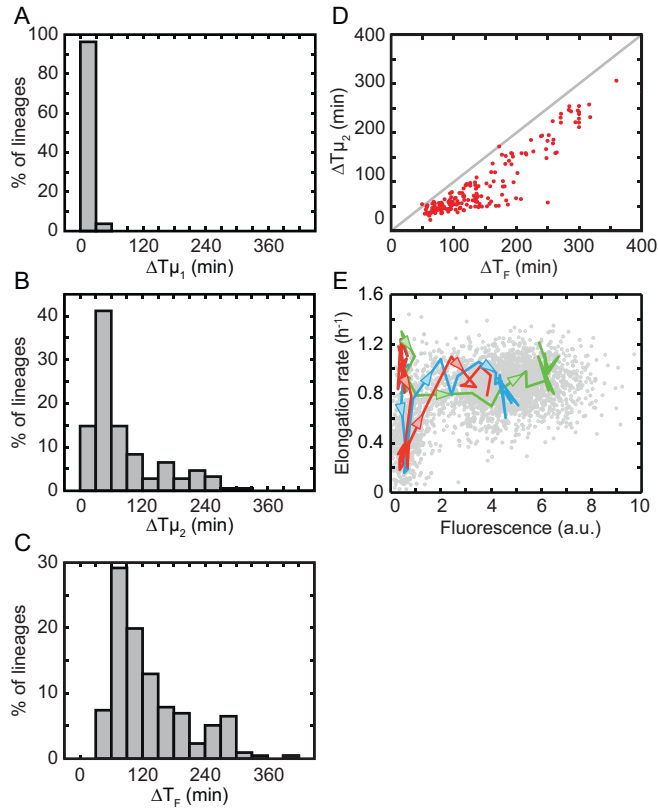


**Figure 3.3** Statistical analysis and correlation between expression and growth. (A) Distribution of growth decrease times  $\Delta T_{\mu_1}$ . (B) Distribution of growth recovery times  $\Delta T_{\mu_2}$ . (C) Distribution of fluorescence recovery times  $\Delta T_F$ .  $N = 216$  for all histograms. (D) Scatter plot of the delays in growth recovery versus delays in fluorescence increase for 185 cell lineages.  $r^2 = 0.85$ ,  $p$ -value  $< 0.001$ . The line drawn is  $\Delta T_{\mu_2} = \Delta T_F$ . (E) Elongation rate versus internal *lac* levels for all lineages (scatter plot, in grey) and the three lineages in Fig. 3.2C. Arrows are directed towards increasing time.

on glucose (Fig. 3.1C). In turn, *lac* expression depended on metabolism through the deactivation of free LacI repressors and random dissociation of DNA-bound repressors stimulated by intracellular lactose. Inducer exclusion and regulation by the cAMP pathway were modeled phenomenologically. Cells divided at a specified size, and their contents were randomly partitioned between the two daughters. Parameter values for the various reactions were, where possible, taken from direct experimental measurements; otherwise, these were inferred indirectly or fit to available experimental data (see Appendix for details). An initial population

of 100 cells was simulated for 210 min on both glucose and lactose, after which external glucose decreased exponentially (decay time  $\tau = 5$  min, Fig. 3.4B). Delay times  $\Delta T_{\mu_1}$ ,  $\Delta T_{\mu_2}$  and  $\Delta T_F$  were determined using the same criteria as for the experimental data. Overall, we found growth and lac expression dynamics to be similar to the experiments (Fig. 3.5A-C). While most cells showed sharply decreased growth around 20 min after the shift, a small fraction of the cells did not and instead maintained a high growth rate ( $\sim 15\%$  of cells, green trace, Fig. 3.5A). Note that the simulated growth rates do not account for random perturbations of the growth rate from other sources as observed in the experiments ( $\sim 20\%$  of the mean growth rate), and are thus artificially smooth. The moment of growth restoration was again highly variable, with  $\Delta T_{\mu_2}$  and  $\Delta T_F$  distributed similarly as for the experiments (Fig. 3.5C).

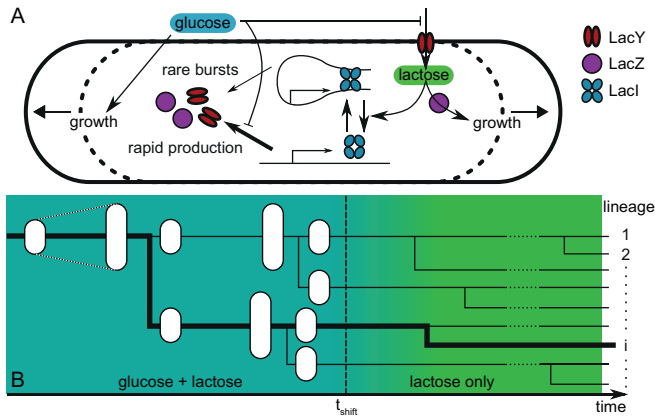


**Figure 3.4** Stochastic model. (A) Within each cell the concentrations of lactose, LacYZ and LacI are simulated, as well as the operator state. Lactose imported from the environment or glucose lead to cell growth. (B) Each cell is simulated until it reaches a specified length, at which point it divides to produce two daughter cells. The proteins of the parent cell are partitioned randomly between the two daughters. The daughters are then simulated until their subsequent division. Growth and fluorescence recovery times ( $T_F$  and  $T_{\mu}$ ) are extracted from the reconstructed cell lineages.

Analysis of the temporal dynamics revealed how growth rates could be maintained at high levels during diauxie. First, stochastic leaky expression of the *lac* proteins during glucose growth gave a fraction of cells a somewhat higher *lac* protein concentration just before the shift, while still at repressed levels [29, 48] (see Fig. 3.5B and D). The resulting comparatively high lactose import triggered

the start of induction of the *lac* operon. However, when external glucose becomes exhausted in these cells, the *lac* expression and hence the concentration of LacZ enzymes that can metabolize lactose is still near repressed levels. A non-linear dependence of growth on *lac* expression is therefore essential as a third ingredient, while metabolism of contaminants and residual glucose may also provide small contributions to the overall growth rate. The relation between cellular growth and expression can here be studied directly by plotting the fluorescence intensity against the concurrent instantaneous growth rate (Fig. 3.3E). The data after growth restoration shows that induction to just 20% of fully induced levels is sufficient to induce near maximal growth on lactose. Thus, even low *lac* levels can generate high growth rates, which is essential to sustaining growth at high levels during the transition. The steep dependence also explains the observed delays of induction with respect to growth for the cells with a lag phase (Fig. 3.3D): growth reaches a near-maximal rate as enzyme production is only beginning to be ramped up.

The inherent positive feedback in the system is crucial for the rapid escape from the lag phase: LacY permeases allow lactose to enter the cell, which in turn leads to *lac* induction and hence increased numbers of permeases. We find that the threshold level of transporters required to initiate this positive feedback is small, with just a few *lac* transporters at the time of shift sufficient for a rapid induction within  $\sim 90$  min (see Fig. 3.5D and Fig. 3.7). On the other hand, cells without permease at the time of shift exhibit a very broad distribution of induction delays (mean  $\Delta T_F \approx 180$  min), with a significant probability of not being induced at all within the time-frame of the simulations. The major component of this delay is waiting for a first stochastic burst of production caused by a partial repressor dissociation (mean waiting time of  $\sim 200$  min), consistent with a previous study of *lac* induction kinetics [29] and a recent theoretical model [155]. Dissociation of repressor typically follows rapidly (within about 20 min), such that expression can be induced to the threshold level (in about 50 min) (see for example Fig. 3.5A and B, red trace, around 250 min). We note that the high threshold for the number of *lac* transporters required for induction reported in a recent study [29] was related to the bistability of that system and the intermediate amounts of inducer that were added, which can explain the difference with our observations. We find that two mechanisms counter this escape from lag: metabolism of lactose and dilution of lactose by volume expansion both decrease its concentration, which tends to drive cells back towards the off expression state, and ultimately arrest of growth. However, both metabolism and dilution are comparatively slow during the lag phase, and hence even a small number of permeases can maintain an appreciable internal concentration of lactose. Once

full induction is achieved the import rate is sufficiently fast to support a high internal lactose concentration, making repressor rebinding rare, and the induced rapid growth state stable.

### 3.2.5 Genealogical relations

Our results indicated that expression history can determine the timing of future switching events. This non-genetic cellular ‘memory’ could result in correlated behavior between genealogically related cells [28]. To test this possibility we compared the delay in growth recovery ( $\Delta T_{\mu_2}$ ) of a recovering cell with the recovery delay of its sister (or, if this sister does not recover, the sister’s progeny). We find a weak but significant correlation ( $r^2 = 0.52$ , p-value  $< 0.001$ , Fig. 3.6A). A control with randomly picked pairs of recovering cells does not display any correlation ( $r^2 = 0.008$ , p-value = 0.47). The simulations also show a weak correlation between growth recovery times (Fig. 3.6B). One may wonder what causes this correlation between sister cells, as the gene expression bursts that underlie exit from the lag phase are stochastic, which should make them independent and uncorrelated. However, a newborn cell inherits *lac* enzymes expressed by the mother, intracellular lactose, as well as *lac* repressors, which all affect the escape probability from the *lac*-repressed state. In particular, both daughter cells will inherit a similar propensity for repressor dissociation and hence full induction. The persistence of correlations between sisters for lag times up to 250 min is surprisingly long, but consistent with the expected decorrelation time for protein concentrations, which are much longer in the lag phase due to the slow growth and volume expansion (the doubling time during lag phase can be up to 5 hours). Additionally, the time between the division event generating the two sisters and induction, which is the time available for decorrelation of the two sister lineages, can be much shorter than the overall lag time if the sister cells divided after the shift of medium. If a cell divides after a small production burst but before dissociation of the repressor, which typically takes tens of minutes after such a production burst, then both daughter cells are likely to inherit some of the *lac* proteins and a significant level of lactose. The two daughter cells will therefore both be induced shortly after division, resulting in very similar values of  $\Delta T_{\mu_2}$  for the two daughter lineages.



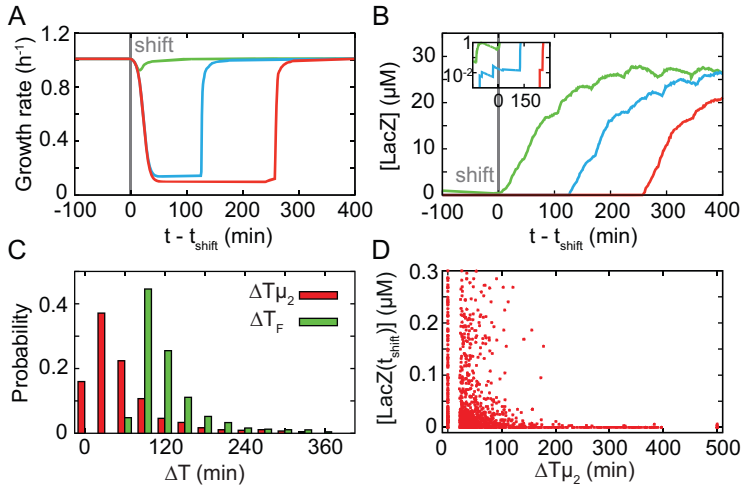


**Figure 3.5** Results of the stochastic model. (A) Example time-series of cell growth rate for a cell with fast (green), slow (blue) and very slow (red) response. (B) Fluorescence time-series for the cells shown in (A). Inset: The same data on a logarithmic scale, showing that cells with higher expression levels at the time of shift of medium tend to be induced more rapidly. (C) Histograms of growth (red) and fluorescence (green) recovery times,  $\Delta T_{\mu_2}$  and  $\Delta T_F$ . In panels (C) and (D), cells at  $\Delta T_{\mu_2} = 0$  showed a decrease in growth rate of less than 20%. (D) *Lac* expression of each lineage at  $t_{\text{shift}}$  plotted against growth recovery time. Cells which did not reach the induction threshold in the time of the simulations are placed at  $\Delta T_{\mu_2} = 500$  min. Cells with initial concentrations above  $\sim 10$  nM typically have a rapid recovery of growth rate. Note that the plot range does not represent the full range of initial expression levels.

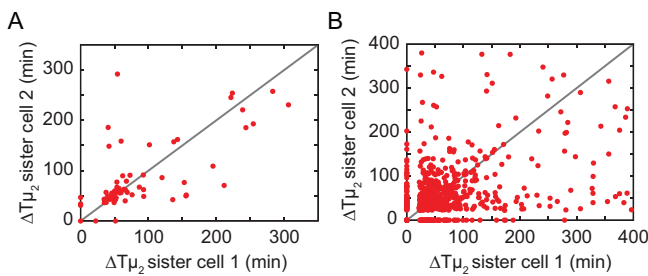


**Figure 3.6** Switching synchrony of sister cells. The growth recovery delays  $\Delta T_{\mu_2}$  are plotted for pairs of sister cells. (A) Data obtained from experiments.  $N = 75$ ,  $r^2 = 0.52$ ,  $p$ -value  $< 0.001$ . (B) Data resulting from simulations.  $N = 660$ ,  $r^2 \approx 0.13$  and  $p < 0.001$ . Note that in both cases lineages in which one cell switches but its sister or its progeny does not are not plotted (in total: 22 pairs for the experimental data, 146 pairs for the numerical data).

### 3.3 Discussion

Monod's original glucose-lactose diauxic growth assays have become the prototypical illustration of the regulation of gene expression. Not only did they reveal the underlying molecular mechanisms, but also how growth and survival in complex environments – the essential cause of their evolutionary origins – is impacted. In the last decade, novel methods to monitor single cells over time has highlighted the stochastic nature of gene expression and its causal molecular mechanisms, and has allowed us to begin uncovering its impact on signal propagation and differentiation [39, 55]. But how molecular stochasticity of biological systems affects their growth and survival remains poorly understood [156, 157]. Here we aimed to begin addressing this problem by interrogating how stochasticity in *lac* expression impacts the dynamics of growth, upon switch from glucose to lactose on single-cell level.

We found that although a population as a whole may display diauxic lag, a significant fraction of the cells within this population (~15%) does not and thus produces an immediate growth response. This result counters the common notion that the speed of the response to lactose changes is determined by the processes of *lac* operon induction, protein dilution and degradation [158]. While correct for the transcriptional response, this study shows that growth responses can be much faster. Our experiments showed cells maintaining a continuously high growth rate, uninterrupted by the switch from glucose to lactose detection and metabolism. Paradoxically, the expression of the *lac* enzymes importing and metabolizing lactose was repressed at the time of shift, and turning on their expression required of order 100 min – conditions that seems more consistent with an obligatory lag phase. However, stochastic simulations together with experimental correlations between expression and growth pointed to a plausible explanation: the stochastic basal *lac* expression before the shift provided some cells with limited but sufficient *lac* permeases to achieve rapid induction, which in turn yielded sufficient *lac* catabolic enzymes to support near-maximal growth rates on lactose by the time glucose was depleted. Limited permease levels were sufficient owing to the positive feedback between *lac* expression and the lactose import rate. Furthermore, the steep dependence of growth on *lac* enzyme concentration permits rapid growth shortly after induction and well before full expression levels are reached. We note that while this model accurately predicts the central experimental features, it is a minimal one, and additional mechanisms can be considered. For instance, one could imagine that growth during the switch is supported rather by other compounds such as acetate that are produced by me-

tabolism overflow during growth on glucose [154]. However, this seems unlikely as such compounds will be depleted at the same rate as glucose by the external flow. Growth could also be briefly supported by internally-buffered compounds [159], though this should not result in the observed heterogeneous growth dynamics.

While a minor fraction of cells continues to grow after the sugar switch, another fraction of the population displayed surprisingly long lag phases. Lag times often exceeded the doubling time as well as the population average lag time by several fold. We showed that these long delays are consistent with the experimentally-observed timescale of rare bursts of *lac* expression in the repressed state, combined with an expression threshold that must be crossed for the 'on' state to remain stable [29]. The stringent response has been shown to be involved in diauxic shifts [160, 161]. Thus stochasticity in cellular components associated with the stringent response, such as ribosomes, could be another source of variability in the growth response, in addition to variability originating from *lac* operon expression. Our results further put a different perspective on the gradual exit from stationary phase as observed at the population level. Exit from the lag phase is significantly more abrupt for individual cells, with the gradual exit seen in bulk assays stemming from averaging over cells with a wide distribution of lag times.

The findings have implications for competition and survival when resources are limited. In general, cells may follow various strategies in heterogeneous environments [156, 162]. One option is responsive switching, in which cells detect the changes in the environment and thus can change their phenotype appropriately. The advantage is that all cells within a population can deterministically exploit new opportunities, but at the cost of expressing a sensing machinery [140], and of time delays involved in changing a cellular phenotype. While the cellular response may be affected by noise in the sensing machinery during and after the environmental change, any cellular heterogeneity prior to the change does not play a role. In contrast, in the stochastic switching strategy [156], cells in constant conditions continually switch in a stochastic manner between phenotypes, and the population as a whole thus displays many different phenotypes. Here, cells are not burdened by sensing costs, yet some cells will be well-adapted directly and thus can act upon opportunities without delay. However, there are significant costs in spuriously expressing phenotypes that are not utilized, and not all cells within the population can exploit transient opportunities.

The data presented here suggest a hybrid third option, namely a stochastic sensing strategy, which overcomes the central tradeoffs. Here, a stochastic expression of the sensing machinery allows a fraction of the population to re-

respond deterministically, without delay, at minimal costs. While the *lac* repressor – a sensor in the *lac* system – is constitutively expressed in line with a responsive strategy, the *lac* transporter also plays a central sensing role, and it is expressed stochastically at low repressed levels in the absence of lactose. As a result, some cells respond immediately while others respond slowly as they wait until the expression of their sensing machinery randomly gets turned on. The costs for the rapidly responding cells are limited, as the sensing function of the *lac* enzymes – nutrient detection – requires just a fraction of transporters that are expressed at full induction. Note that while it is weak, a trade-off does remain, as the slowly responding cells express even less of the sensing machinery in glucose. Importantly, even the metabolic function of the *lac* enzymes – nutrient import and catalysis – initially requires just a fraction of full induction because of the non-linear expression-growth relation. This enables immediate growth responses with zero delay, despite the delays involved in turning expression up until fully induced levels. Rapid growth responses are particularly acute when competing for limited resources: those genotypes capable of responding rapidly may consume all resources before slow genotypes respond, and hence dramatically out-compete them. Stochasticity is an essential ingredient in this strategy, as it limits the burden of maintaining the responsive state to just a fraction of the population, and thus hedging its bets at minimal cost on future episodes when lactose becomes available.

## 3.4 Appendix

### 3.4.1 Supplementary figures

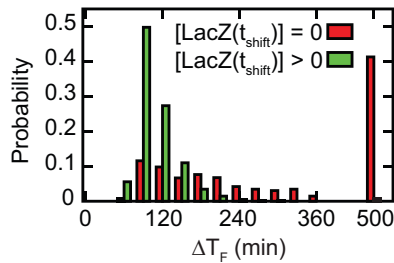


**Figure 3.7** Distribution of computed fluorescence induction times for cell lineages with (green) and without (red) permease present at the time of shift.

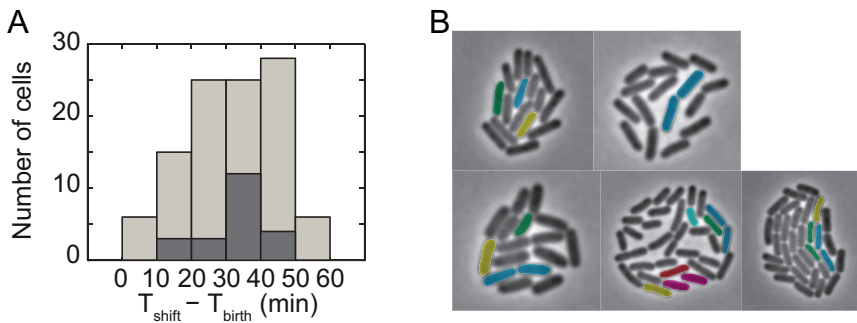


**Figure 3.8** Absence of lag phase is not due to cell cycle or spatial dependence. (A) Distributions of time of shift - time of birth for cells with growth arrest ( $N = 105$ , mean =  $27 \pm 12$  min (SD); light grey) and continuously growing cells ( $N = 22$ , mean =  $28 \pm 9.8$  min (SD); dark grey), showing that the two distributions are similar. (B) Phase contrast images of microcolonies at the time of shift. Continuously growing cells are colored. The colors were chosen randomly, but sister cells were given the same color.

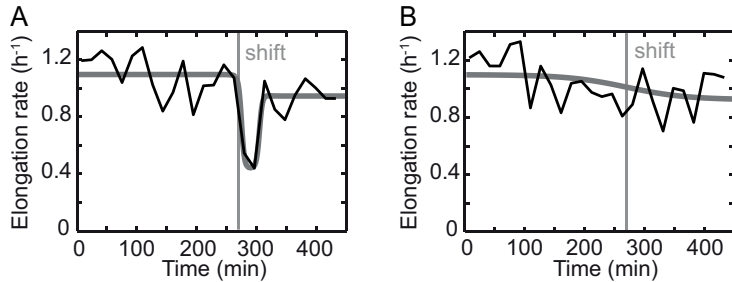


**Figure 3.9** Shift from a medium containing glucose and lactose to a medium containing lactose only. (A) Example of a growth traces showing a decrease upon shift to lactose. As in the main text, the fit is shown in thick lines. (B) Example of a growth traces showing no visible growth decrease. Continuously growing cells represent ~10% of the total lineages analyzed, which compares to the 15% obtained from glucose-only to lactose experiments.

### 3.4.2 Strain and media

All experiments were performed with the *E. coli* strain AB460 (created by A. Böhm and kindly provided by M. Ackermann). AB460 is a derivative of MG1655 (*rph-1 ilvG- rfb-50*). To measure the expression of the *lac* operon, *lacA* was replaced with *GFPmut2* [125] and chloramphenicol resistance using the protocol described by Datsenko and Wanner [126].

Cells were grown in M9 minimal medium with 0.2 mM uracil (as described in chapter 2), supplemented with 0.01% (w/v) glucose (Merck) or 0.1% (w/v) lactose (Fluka). The M9 medium supplemented with lactose also contained cells with a knocked-out *lac* operon (NCM520, obtained from the Coli Genetic Stock Center). These cells cannot grow on lactose but can grow on the contaminants present in the medium. NCM520 cells were inoculated from glycerol stock in M9 + 0.1% (w/v) glucose for growth overnight. The following day, cells were washed with M9 + 0.1% (w/v) lactose and transferred to the same medium to be used for experiments. To control for glucose depletion, the red fluorescent dye sulforhodamine 101 (0.01 mg.mL<sup>-1</sup>) was systematically added to the M9 medium containing glucose.

### 3.4.3 Parameterized functions used to fit the experimental data

Fluorescence time traces for individual cells were fitted by the following

parameterized function using the function:

$$f(t) = \frac{(b-a) \cdot \tanh\left(\left(\frac{t-t_0}{\tau}\right) + a + b\right)}{2}$$

where  $a$  is the lower asymptote,  $b$  is the upper asymptote,  $\tau$  is the characteristic time of fluorescence change,  $t_0$  is the time where fluorescence is at half its maximum ( $t_0 - t_{shift} = \Delta T_F$ ).

Similarly, elongation rates for individual cells were fitted by the following function:

$$g(t) = \left( \frac{a-b}{2} \cdot \tanh\left(\frac{t_0-t}{\delta}\right) + \frac{a+b-2c}{2} \right) \cdot \left( 0.5 + \frac{\tanh\left(\frac{\text{abs}(t-t_0)-\delta}{\tau}\right)}{2} \right) + c$$

where  $a$  is the growth rate before shift,  $b$  is the growth rate after shift,  $c$  is the depth of the dip,  $\delta$  is the duration of the lag phase,  $\tau$  is the characteristic time of growth rate change,  $t_0$  is the time at the middle of the lag phase.

### 3.4.4 Complete description of the stochastic model

Here we discuss in detail the stochastic model of the growth of *E. coli* and the expression of *lac* proteins during the switch of environmental conditions from glucose and lactose to lactose only. The model has been developed on the basis of a number of previously described models [150, 158, 163, 164], but some simplifications have been made in the dynamics of protein production and sugar metabolism with many reactions coarse-grained into a single effective reaction step. Parameter values were taken from experiments where possible, and elsewhere are largely consistent with those used in these models.

#### Operator dynamics and protein production

The multiple operator sites of the *lacZYA* operon and the multiple binding sites of the *LacI* repressor for both DNA and inducer mean that the chromosome-repressor-inducer complex can exist in many distinct binding states [165]. While it has been proposed that individual partial dissociation events can lead to observable changes in *lac* expression [29], it remains unclear which are the rele-

vant binding configurations in vivo and how expression and binding propensities vary between different binding states. We therefore consider a greatly simplified phenomenological model of a single lac operator which can exist in only two states: the operator can be either BOUND by repressor, in which case there is a slow rate of leaky protein production  $\kappa_B$ , or FREE of repressor, in which case protein production occurs at a rapid rate  $\kappa_F([\text{glu}] )$ . The regulatory effect of the cAMP pathway, which increases *lac* expression in environments lacking glucose, is represented through the dependence of the production rate from the FREE operator on the environmental glucose concentration, according to the relationship:

$$(1) \quad \kappa_F([\text{glu}]) = \frac{\kappa_{F,\text{max}}}{1 + [\text{glu}]/K_{\text{CAP}}}$$

The effective parameter  $K_{\text{CAP}}$ , the effective repression strength of glucose and the fold change in expression in the presence of CAP, incorporate a number of processes including cAMP expression, cAMP-CRP binding and binding of CAP to the DNA, and should not be interpreted as describing any specific molecular interaction. We do not include any effect of cAMP on the transcription rate in the BOUND state as we assume that the timescale of these bursts is determined primarily by partial dissociations of repressor in the actual system (see below), which we take to be independent of CAP binding. We additionally assume that the rate of protein production events is dependent on the growth rate of the cell, since under starvation conditions cells may be limited in their ability to synthesis proteins. Specifically, we assume that the rate of production events in a cell with growth rate  $\mu$  is modulated by a factor  $2\mu/(\mu_{\text{max}} + \mu)$ , where  $\mu_{\text{max}}$  is the maximal achievable rate of growth on glucose.

For simplicity we assume that all proteins in the *lac* operon are coexpressed, and represent the concentration of both LacZ and LacY proteins by  $[Z]$ . Protein concentrations are calculated from the copy number  $N_Z$  and cell length  $l$  assuming a cylindrical cell with a constant radius of  $r = 0.25 \mu\text{m}$ .

Statistics of *lac* protein production have been measured in [29, 48]. They described two types of production bursts. During small bursts the number of proteins produced,  $b$ , is exponentially distributed,

$$(2) \quad p(b) = \frac{e^{-b/\bar{b}}}{e^{1/\bar{b}} - 1}$$

with  $\bar{b} \sim 5$ . This was interpreted as the distribution of proteins produced from a single mRNA transcript. Larger bursts were also found, although their distribu-



tion was not characterized. We interpret these large bursts as resulting from many mRNA transcripts being produced in quick succession, such that the products of the individual transcripts cannot be resolved. Here, we assume that an individual gene transcription event, in either the BOUND or FREE operator state, gives rise to a number of proteins according to the distribution (2). The production characteristics in these two states differ only in the average rate of transcription events.

We assume that  $\text{Lacl}$  repressor proteins are produced at a rate  $\kappa_R$ . The concentration of repressors decreases only due to dilution, with no degradation. Repressors can be active or inactive; binding of inducer causes repressor deactivation. Since repressor-inducer binding and dissociation is fast ( $< 1$  s) we do not model (de)activation reactions explicitly but instead assume that this is a reversible reaction at equilibrium. The fraction of active repressors is then given by:

$$(3) \quad \frac{[R]^*}{[R]_T} = \frac{1}{1 + ([L]/K_R)^h}$$

where  $[R]_T = N_R/l$  is the total concentration of repressor proteins,  $N_R$  is the number of repressor proteins in the cell,  $[L]$  is the intracellular lactose concentration and  $K_R$  is the binding constant for lactose (or products of lactose metabolism) to the repressor. The Hill coefficient  $h$  allows for cooperativity in the deactivation of the repressor tetramer. The rate of association of repressor to the FREE operator depends on the concentration of active  $\text{Lacl}$ ,  $k_{F \rightarrow B}[R]^*$ . We assume that dissociation of  $\text{Lacl}$  from the operator is also enhanced by the presence of lactose. We assume that at any time a fraction  $\varphi = (1 + K'_R/[L])^{-1}$  of DNA-bound repressors is associated with inducer. The net dissociation rate of repressors from the operator is then taken to be  $k_{B \rightarrow F}(1 + k'\varphi)$ , where  $k'$  is the enhancement factor of dissociation for inducer-bound repressors. We emphasize that since we use a simplified two-state operator model, this enhancement of dissociation represents an effective action of lactose on repressor binding, which in reality could be due to a number of processes on a molecular level.

### Parameter values

The maximal rate of production bursts for the FREE operator is taken to be  $\kappa_{F,\max} = 15 \text{ min}^{-1}$ , comparable to the experimentally-determined rate of transcription initiation [166]. This leads to copy numbers of a few thousand molecules in fully induced cells, which is also consistent with data of [29]. For

the leaky production rate when the operator is BOUND we take the burst rate measured in [29, 48] for fully repressed cells,  $\kappa_B \sim 0.5$  per cell cycle  $\sim 0.005 \text{ min}^{-1}$ . The strength of cAMP-mediated transcriptional repression by glucose,  $K_{\text{CAP}} = 30 \text{ }\mu\text{M}$ , is chosen to fit the results to the experimental delay distributions.

The typical concentration of repressors is 10-50 nM, corresponding to  $\sim 1$ -20 per cell [167, 168]. We take a production rate  $\kappa_R = 5\mu$ , which gives a typical concentration of  $[R]_T \approx 20 \text{ nM}$ .

The choice of binding constant for inducer-inhibitor binding is complicated by the fact that it is allolactose, rather than lactose itself, which binds to the repressor, but our model does not include allolactose explicitly. However, in practice upon the addition of lactose cells rapidly reach a stable high lactose concentration  $> 1 \text{ mM}$ , and the precise value of the parameter  $K_R$  will have little effect on the dynamics provided that it is much smaller than this value. We simply take  $K_R = 10 \text{ }\mu\text{M}$ , comparable to measured values for allolactose and other strong inducers [169]. The effective Hill coefficient for deactivation of inhibitor has been estimated as  $h \approx 2$  [170]. For the binding constant for inducer and DNA-bound repressor we take  $K'_R = 200 \text{ }\mu\text{M}$ .

For the binding rate of repressor to the operator we use  $k_{F \rightarrow B} = 60 \text{ }\mu\text{M}^{-1} \text{ min}^{-1}$ , which gives a binding rate comparable to the association time measured in [167]. A dissociation rate of LacI from the operator of  $k_{B \rightarrow F} = 0.0005 \text{ min}^{-1}$  gives rise to an  $\sim 1100$ -fold difference between the mean expression levels in the repressed and fully-induced states, which is again consistent with the data of [29]. Experiments suggest that the enhancement of this dissociation rate by inducer for binding to a single operator fragment can be as large as a factor of 1000 [171]. Here we choose  $k' = 100$ , since in the presence of DNA looping with multiple operator binding sites not all dissociation events will lead to full release of the repressor.

### Intracellular lactose dynamics

We do not consider individual lactose molecules since these will be present in extremely high copy numbers within the cell. The rate of import of extracellular lactose into the cell depends on the concentration of permeases, which equals the concentration of LacZ, their activity, and the external lactose concentration:

$$(4) \quad v_{\text{import}} = \rho([\text{glu}]) \frac{[Z][L]_{\text{ex}}}{K_{\text{import}} + [L]_{\text{ex}}}$$

Following previous models [150, 164], inducer exclusion is implemented by making the import rate for an individual permease a decreasing function of the concentration,  $\rho([\text{glu}]) = \rho_{\max}/(1 + [\text{glu}]/K_{\text{excl}})$ . Intracellular lactose is diluted during growth. In addition, it is metabolized by LacZ. Since typically  $[L] \gg [Z]$ , the flux of this reaction is simply taken to be proportional to  $[Z]$ ,

$$(5) \quad v_{\text{consumption}} = \Delta \frac{[Z][L]}{K_L + [L]}$$

Finally, therefore, the overall lactose concentration within a cell follows:

$$(6) \quad \frac{d[L]}{dt} = v_{\text{import}} - v_{\text{consumption}} - \mu[L]$$

where  $\mu$  is the cell growth rate.

#### Parameter values

The maximal import rate of lactose is around  $\rho_{\max} = 2000 \text{ min}^{-1}$  [172, 173]. The critical glucose concentration for inducer exclusion is determined, together with  $K_{\text{CAP}}$ , by fitting the delay time distributions and is taken to be  $K_{\text{excl}} = 30 \text{ }\mu\text{M}$ . The lactose import saturation concentration is  $K_{\text{import}} = 400 \text{ }\mu\text{M}$  [172, 173]. The maximal rate of metabolism of lactose by a single  $\beta$ -galactosidase enzyme is set as  $\Delta = 3600 \text{ min}^{-1}$  [174]. The saturation coefficient for lactose conversion by  $\beta$ -galactosidase is  $K_L = 1.4 \text{ mM}$  [174].

#### Growth rate

There are three sources of growth in the experiments: glucose, lactose and contaminants, and these can all be present simultaneously. In order to model the combined metabolism of all three carbon sources at once we assume that these three sources contribute to the same effective metabolic flux,

$$(7) \quad \Phi = [\text{glu}] + \delta \frac{[Z][L]}{K_L + [L]} + \Phi_{\text{res}}$$

Here the first term is the concentration of glucose in the environment. The metabolism of glucose is not simulated in detail, and is simply assumed to be independent of the internal state of the cell. The second term in (7) is the flux of

lactose metabolism by LacZ. The parameter  $\delta$  weighs the relative contributions of glucose and lactose metabolism. Finally,  $\Phi_{\text{res}}$  is a constant residual flux due to contaminants.

This growth rate is then taken to be a Monod-function of the flux,

$$(8) \quad \mu = \mu_{\text{max}} \frac{\Phi}{\Phi + K_{\Phi}}$$

The parameter  $K_{\Phi}$  reflects the fact that growth is limited by other processes independent of metabolism, and therefore cannot be increased arbitrarily.

#### Parameter values

The parameters  $\mu_{\text{max}} = 1.02 \text{ h}^{-1}$ ,  $\Phi_{\text{res}} = 0.54 \text{ }\mu\text{M}$  and  $K_{\Phi} = 5.1 \text{ }\mu\text{M}$  can be found by fitting the growth rate as a function of glucose level in the absence of lactose. We choose  $\delta = 50$  to fit the experimental growth dynamics.

A consequence of assuming this form for the growth rate is that the maximal growth rate on lactose can approach the maximal growth rate on glucose if the lactose concentration  $L > K_L$  and  $\delta[Z] > K_{\Phi}$ . With the parameters listed above the maximal expression level is  $[Z] \approx 25 \text{ }\mu\text{M}$ , and hence the maximal growth rates on the two substrates are similar.

#### Cell division

The change in cell length over time follows:

$$(9) \quad \frac{dl}{dt} = \mu \cdot l$$

For a constant growth rate  $\mu$ , this corresponds to exponential growth. We assume that all cells divide when they reach a critical length  $l_{\text{div}}$ , which is independent of the growth rate or protein levels. Upon division a new cell is created with half of the length of the parent cell, which also has its length halved. The repressor and LacZ molecules in the parent cell are binomially-partitioned between the parent and daughter cells (i.e. each protein is moved into the new daughter cell with probability 0.5 or otherwise remains in the parent cell). Assuming that the number of lactose molecules is large and noise in partitioning can be neglected, the lactose concentration in the daughter cell is set to be the same as that of the parent cell. The daughter cell also inherits a copy of the operator which is in the

same state (BOUND or FREE) as the parent at the time of division.

Parameter values

$$l_{\text{div}} = 3 \mu\text{m}.$$

### Simulation protocol

The model is propagated with a constant time step  $\delta t$ . At each time step the active repressor and LacZ concentrations and the growth rate are recalculated according to the current cell length and lactose concentration.  $[L]$  and  $l$  are updated according to Eqs. (6) and (9) with a first-order difference scheme (i.e.  $l(t + \delta t) = l(t) + \delta t \cdot l'(t)$ ). Switching of operator can switch with probability  $\delta t \cdot k$ , where  $k$  is the relevant switching rate. Similarly, a protein production burst takes place with probability  $\delta t \cdot \kappa$ , where  $\kappa$  is the appropriate production rate for the current operator state. Errors due to this discretization will be negligible provided  $\delta t$  is chosen to be small enough. Here we take  $\delta t = 0.001$  min, which ensures that the probability for each stochastic reaction to occur during each time step is much less than 1.

First, an initialization simulation is performed. A population of 2000 cells is simulated in the presence of glucose only,  $[\text{glu}] = 555 \mu\text{M}$  and  $[L]_{\text{ex}} = 0$ , for a period of 10000 minutes. During this simulation only one of the daughter cells produced in each cell division event is retained, such that the population size is constant and each cell present at the end of the simulation is an independent sample of the steady-state distribution of cellular states.

Next, a sub-population of 100 cells is selected randomly from those present at the end of initialization simulation to form the initial population in the simulation of the experimental conditions. During the subsequent phases of simulation all daughter cells are retained and propagated to the end of the simulation period in order to preserve correlations between related lineages. This population of cells is then propagated as described above in an environment mimicking the experimental conditions of glucose,  $[\text{glu}] = 555 \mu\text{M}$ , and lactose,  $[L]_{\text{ex}} = 3 \text{mM}$ , until the shift time  $t_{\text{shift}} = 210$  min. After the shift time the concentration of glucose is decreased according to  $[\text{glu}](t) = \exp[-(t - t_{\text{shift}})/\tau] \cdot 555 \mu\text{M}$ , while lactose remains unchanged. The timescale  $\tau = 5$  min is chosen to match the experimentally-determined timescale for diffusion out of the flow chamber. The simulation continues until a time  $t = 610$  min.

For each cell, time series of the growth rate and expression level data are recorded, and subsequently used to recreate the trajectory of each cell lineage. The mean concentration in fully-induced cells in the presence of lactose is  $[Z] \approx 25 \mu\text{M}$ . Lineages which reach a concentration level of at least  $[Z] = 17 \mu\text{M}$  during the simulation are identified as becoming induced. For each such lineage the threshold LacZ concentration for calculating  $\Delta T_{\text{F}}$  is set at half the maximal concentration of the lineage. Lineages for which the growth rate never decreases below  $\mu = 0.82 \text{ h}^{-1}$  are designated as having no lag phase. For the remaining lineages, the time of growth decrease  $\Delta T_{\mu_1}$  is found as the time at which the growth rate trajectory crosses a threshold half-way between the maximal growth rate on glucose and the lowest growth rate after the shift of medium. The time of growth recovery  $\Delta T_{\mu_2}$  is similarly found as the time at which the growth rate crosses a threshold midway between the lowest growth rate after the shift and the highest subsequent growth rate.

*The mathematical model reported in this chapter was done by Filipe Tostevin.*

## Prolonged linear growth in single bacterial cells upon exposure to antibiotics

### 4

*Growth of bacterial cells is exponential: during the cell cycle new components are synthesized, which in turn help to synthesize other components. How growth is affected when this exponential growth is disrupted is not known. Here we investigate the response of individual cells growing on lactose only upon addition of the translation inhibitor tetracycline. We controlled the environment with a microfluidic device, and monitored cellular growth at sub-cycle resolution while also following the expression of several essential enzymes. We show that inhibition of lac synthesis leads to linear growth. In this growth regime, ribosomes synthesis is maintained at a lower rate. In addition, we find that the linear growth rate correlates with the size of cells at the moment of tetracycline addition, resulting in significant cell-to-cell variability. Further increase in antibiotic concentration allows growth to continue transiently, until ribosomes synthesis is suppressed. This study shows that in absence of lac protein synthesis, existing lac proteins are able to sustain cellular growth, and further underlies the importance of single-cell investigations of the effects of antibiotics.*

## 4.1 Introduction

A defining feature of continuous microbial growth is that it is exponential, with the number of cells within a population doubling each division cycle. Within the division cycle, bacterial growth laws have been the subject of debate. Cell size has been considered to increase either in bilinear [175], bilinear and trilinear [176], or exponential [177] fashion, while recent evidence has shown exponential mass increase in single cells [178, 179]. All models are non-linear however, with older cells on average growing more rapidly than young ones. The common explanation is that because older cells are larger, they contain more copies of active components such as metabolic enzymes and ribosomes, and hence increase size faster [180, 181]. This logic reflects the cycle inherent to self-replication, where active components help producing the building blocks that are required for their own synthesis (Fig. 4.1A).

The cyclical nature of biological growth raises the fundamental question how growth is affected by interrupting this cycle. Because of its essential nature, experimentally interrupting the cellular growth cycle poses challenges. For instance, knocking out components that form the cycle produces non-viable cells [182]. Here, we overcome this issue by directly observing the growth of individual *E. coli* cells as their protein synthesis becomes interrupted by the antibiotic tetracycline within a microfluidic chamber. In bulk experiments, tetracycline is known to inhibit translation and cause arrested growth, but the transient growth response in individual cells is not well understood. Here, we grow the cells on lactose, which is imported and catabolized by the LacY and LacZ enzymes respectively, which provides all the energy and carbon required for growth. The instantaneous growth rate of individual cells is quantified at sub-cell-cycle resolution, by taking phase contrast images at high acquisition rates and image analysis algorithms. The concentration of LacY and LacZ enzymes is quantified using GFP fused within the *lac* operon. With this approach, we can simultaneously follow both the synthesis of the first-acting enzymes and the resulting cellular growth rate. Using mCherry fusions, we also follow the expression dynamics of other components that are important to growth, including the ribosome and *gltA*, a central enzyme in the TCA cycle.

We found that when antibiotics were added to concentrations that fully blocked *lac* enzyme synthesis, the cells continued to grow in a linear fashion for over 12 hrs, until we stopped the experiment. Moreover, the antibiotics appeared to ‘freeze’ the cells in their current growth state: cells that were large at the shift time maintained a faster linear rate of growth than the small cells over



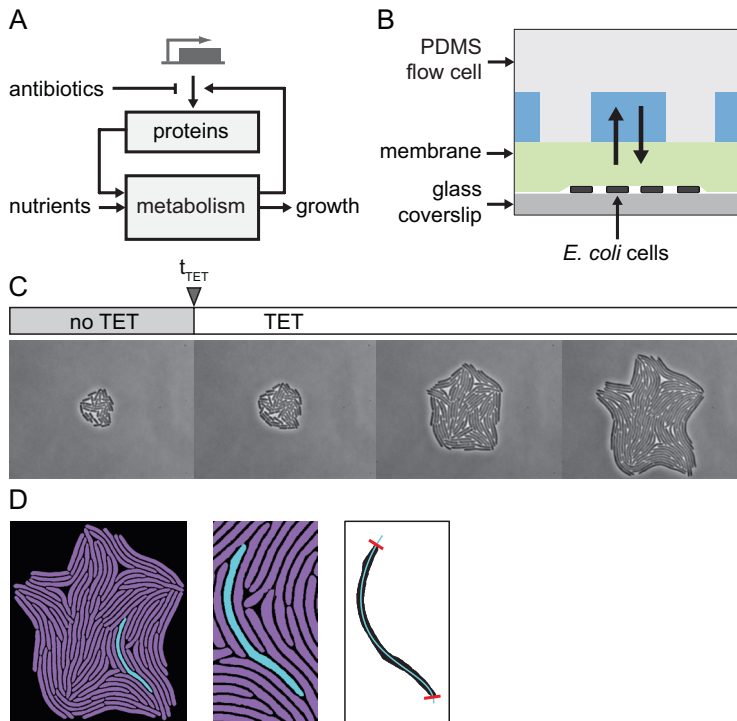


**Figure 4.1** Real-time observation of single-cell growth upon translation inhibition. (A) Schematic representation coupling nutrient import, metabolism and growth. (B) Cross-section of the used microfluidic device. The cells are growing on a glass coverslip and a polyacrylamide gel membrane. The medium that flows through the top channels reaches the cells by diffusion through the membrane. (C) Phase contrast images of a microcolony obtained by time-lapse microscopy. After a few generations of growth on lactose only, tetracycline is added to the environment. The images were taken 1 hr before addition of the drug, at the time of addition  $t_{TET}$ , and 6 hrs and 12 hrs afterwards. (D) Segmentation of phase contrast images using custom image analysis software. Contour of every cell within the microcolony (left). Cells are fitted with a polynomial to determine the cell length (right).

the timescale of the experiment. The results indicated that this linear mode of growth was supported by the *lac* enzymes present at the time of shift, while it did require renewed synthesis of ribosomes, at a rate of about one third of the level before the shift. Fully suppressing ribosome synthesis by increasing the antibiotic concentration did allow growth to proceed transiently after the shift, resulting in an approximate doubling of the cell size, but the rate of growth continued to decrease over time. The results show that cellular growth continues well beyond

the moment of translation inhibition, in a way that is masked in bulk measurements. This study demonstrates that antibiotics can be used to study metabolism and growth in the absence of the complicating factor of continuously renewed protein synthesis, in a manner that is complementary to *in vitro* assays. On the other hand, measurements of the instantaneous growth rate upon exposure to antibiotics can be an important new tool to understand the physiological effects of antibiotics [183], and to develop novel antibiotics.

## 4.2 Results

### 4.2.1 Linear growth upon inhibition of *lac* expression

Starting with a single cell, we monitored by time-lapse microscopy *E. coli* cells as they grew into microcolonies within a microfluidic device (Fig. 4.1B). After several generations of growth on lactose, we exposed the cells to a medium containing both lactose and the translation-inhibiting antibiotic tetracycline [184, 185] (Fig. 4.1C). We measured the expression of the *lac* genes with a GFP reporter (Fig. 4.2A and Methods). The total fluorescence of the microcolony is defined as the sum of the total fluorescence of each cell within the microcolony (Fig. 4.2B and Methods). The mean production rate of *lac* enzymes within the microcolony (Fig. 4.2C) was quantified by averaging the production rate of each cell in the microcolony (see Methods). Upon exposure of tetracycline at low concentrations (0.5  $\mu\text{M}$ ), the *lac* production rate decreased by about 30% (Fig. 4.2C) while the total fluorescence continued to increase exponentially (Fig. 4.2B, purple trace). At concentrations equal to 1  $\mu\text{M}$ , the *lac* production rate became zero within half an hour upon tetracycline exposure (Fig. 4.2C), and hence the total fluorescence remained constant (Fig. 4.2B). Further increasing the tetracycline concentration did not significantly alter the outcome (Fig. 4.2B-D). Note that the observed small differences in the total fluorescence at the time of shift is not relevant here, as it depends on the total number of cells that are present at the time of shift. Also, a minor decrease in the total fluorescence is observed about 100 min after the inhibition of *lac* protein synthesis (see Fig. 4.2B). This was due to photo bleaching of the GFP molecules, which was confirmed by the fact that microcolonies less frequently illuminated showed a correspondingly slower decrease.

Growth was followed by measuring the length of the cells over time. We observed no significant changes in cell width during the experiment (Fig. 4.5).

At low tetracycline concentrations where *lac* expression was only partially inhibited, exponential growth was maintained after the shift (Fig. 4.2E and F, purple trace). At the concentrations where *lac* protein synthesis became fully inhibited (1  $\mu\text{M}$  and 2  $\mu\text{M}$ ), the cells continued to elongate in a strikingly linear fashion for over 12 hrs until the experiment stopped. Division became highly infrequent and stopped completely within 400 min after addition of the drug, resulting in highly elongated cells that reached up to 10 times the size of a normally growing cell (Fig. 4.1C and Fig. 4.2E-F). This observation of long filamentous cell morphologies is consistent with previous studies on the effects of low concentrations of tetracycline [186]. At the highest tetracycline concentration (8  $\mu\text{M}$ ), the cells stopped to divide rapidly (within 30 min; Fig. 4.3E red trace), while the elongation rate of the microcolony continuously decreased without reaching steady state. We found that the moment where *lac* synthesis became arrested (Fig. 4.2C) corresponded to the moment at which exponential growth was no longer observed (Fig. 4.3E, grey arrow).

#### 4.2.2 Single-cell heterogeneity in linear growth rate

Within a microcolony, different lineages displayed significant variability in their response to tetracycline. One way we quantified this variability is by the distribution of cell lengths after 12 hours of growth in presence of the drug. Without antibiotic, the cell length was narrowly distributed around 2.6  $\mu\text{m}$  (Fig. 4.3A, black line). At 1  $\mu\text{M}$  tetracycline, the cell length ranged from  $\sim 3$   $\mu\text{m}$  to almost 20  $\mu\text{m}$  (10  $\mu\text{m}$  on average). Upon further increases in tetracycline concentration (up to 8  $\mu\text{M}$ ), the width of the distribution decreased again. This peaking of the distribution width can be explained by the concomitant increase in total cell length, resulting in constant coefficient of variation, both for all concentrations of tetracycline ( $\sim 24\%$ ) and the no- drug control ( $\sim 28\%$ ). These results indicate that translational inhibition does not introduce more length variation.

Next, we considered the growth dynamics of individual cells (Fig. 4.3B). The data confirmed that growth was linear also at the level of individual cells. Moreover, it showed a striking heterogeneity, with some cells having 2 times higher growth rate than others, and maintaining this difference of the entire course of the experiment (Fig. 4.3B). These differences could be explained within the rudimentary model in which non-linear growth arises from the fact that older cells have more active components and hence grow faster. It thus also suggests that cells that are older at the time of shift display a high linear growth, while younger cells display a low linear rate of growth (Fig. 4.3C). We indeed find that

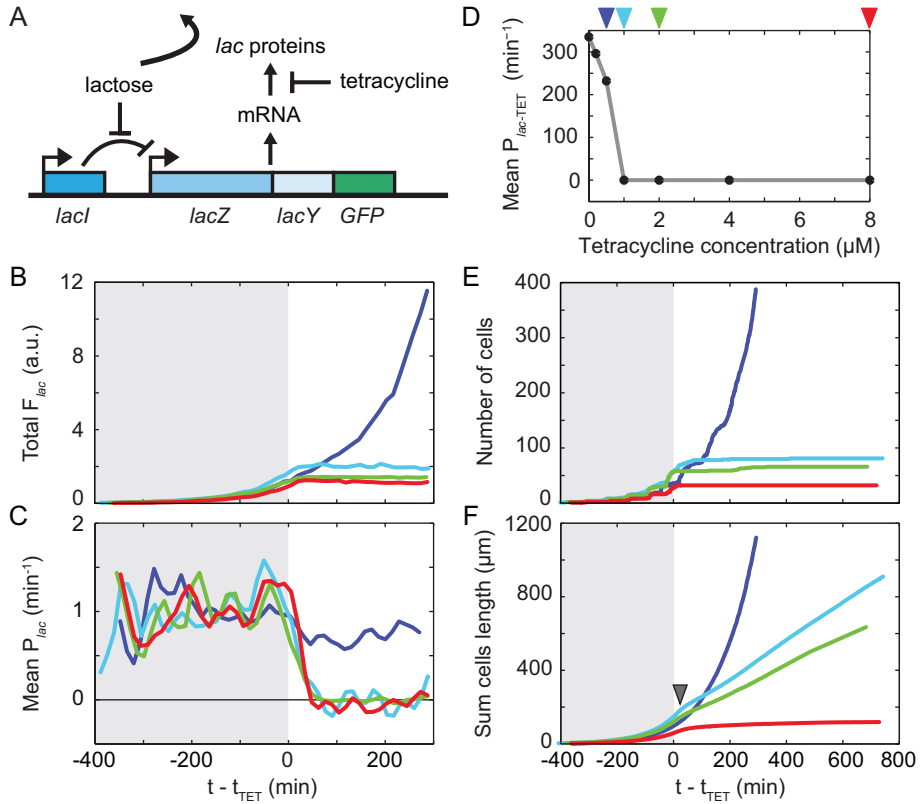


**Figure 4.2** Growth and *lac* expression of a microcolony. (A) Cells are growing exponentially on lactose as the sole carbon source. Expression of the *lac* genes is monitored with GFP. Addition of tetracycline causes inhibition of *lac* mRNA translation. (B-C) Total *lac* fluorescence (B) and mean production rate of the *lac* genes (C) at different tetracycline concentrations. The horizontal line corresponds to production rates of zero. (D) Mean production rate of the *lac* genes in presence of tetracycline  $P_{lac-TET}$  at different drug concentrations. The concentrations further used in this study are indicated by a colored arrow. (E-F) Number of cells (E) and growth curve (F) for a typical microcolony at different tetracycline concentrations as indicated in (D). The growth curve indicates the sum of all cell lengths within the colony. These concentrations represent three different regimes of growth: exponential (0.5  $\mu\text{M}$ ), linear (1 and 2  $\mu\text{M}$ ) and sub-linear (8  $\mu\text{M}$ ). The grey arrow indicates the time of *lac* synthesis arrest.

the linear elongation rate correlates as expected both with the time of birth (Fig. 4.3B inset) and with the cell size at the time of shift (Fig. 4.3D;  $r^2 = 0.42$ ,  $p\text{-value} < 0.001$ ). We also found a similar result at 8  $\mu\text{M}$  tetracycline (Fig. 4.6).

In addition, a similar correlation was found between elongation rate and

the number of ribosomes at the time of tetracycline addition ( $r^2 = 0.50$  and  $p$ -value  $< 0.001$ ,  $N = 26$ ). Since the correlation is rather weak, other sources of variability can be considered. For instance, antibiotics cause many physiological changes. It was shown that tetracycline induces cold-shock response [187]. Also the expression level of most genes changes, even at sub-inhibitory concentrations [188, 189]. Another cell response to inhibition of translation could be an attempt to restore protein synthetic capacity by increasing ribosome production and activating transcription of rRNA and ribosomal protein genes [67, 190]. However, another indirect effect of ribosome-targeting drugs is inhibition of ribosome assembly [191, 192], caused by excess of rRNA expression compared to ribosomal proteins [193, 194]. These different direct and secondary effects of the drug could thus affect the elongation rate of single cells.

### 4.2.3 Expression of ribosomes and a TCA cycle enzyme

The data indicated that cellular growth became linear when the production of *lac* enzymes was stopped. To investigate further requirements for linear growth, we aimed to monitor the expression of ribosomes, a gene involved in central metabolism, as well as a constitutively expressed protein (Fig. 4.4A). Ribosome synthesis was monitored with a translational fusion between mCherry and the ribosomal protein L31. From the enzymes acting in the TCA cycle, we chose to follow *gltA* by constructing a transcriptional fusion with GFP. To test expression of a constitutive protein, we made a construct with a transcriptional fusion between the promoter  $P_{N25}$  from T5 bacteriophage and mCherry (see Materials and methods). These constructs were interrogated during a switch to tetracycline at 1  $\mu$ M and to 8  $\mu$ M.

For 1  $\mu$ M, we found that the mean *gltA* production rate decreased rapidly down to zero upon tetracycline addition, and after about 200 min transition period it increased to a rate roughly equal to a third of the pre-drug level and remained constant afterwards (Fig. 4.4B, green trace). The mean production rate of ribosomes displayed a slow decrease down to about half the pre-drug level (Fig. 4.4B, yellow trace). The production rate of  $P_{N25}$  first stayed constant up to 300 min after tetracycline addition, after which it started to increase (Fig. 4.4B, blue trace). This increase suggests a change in the repartition of ribosomes activity.

At 8  $\mu$ M, the production rate of *gltA* decreased immediately upon tetracycline addition and was zero within 30 min (Fig. 4.4C, green trace). The production rate of  $P_{N25}$  first stayed constant for about 50 min, then decreased down to zero within the next 50 min (Fig. 4.4C, blue trace). Ribosome production

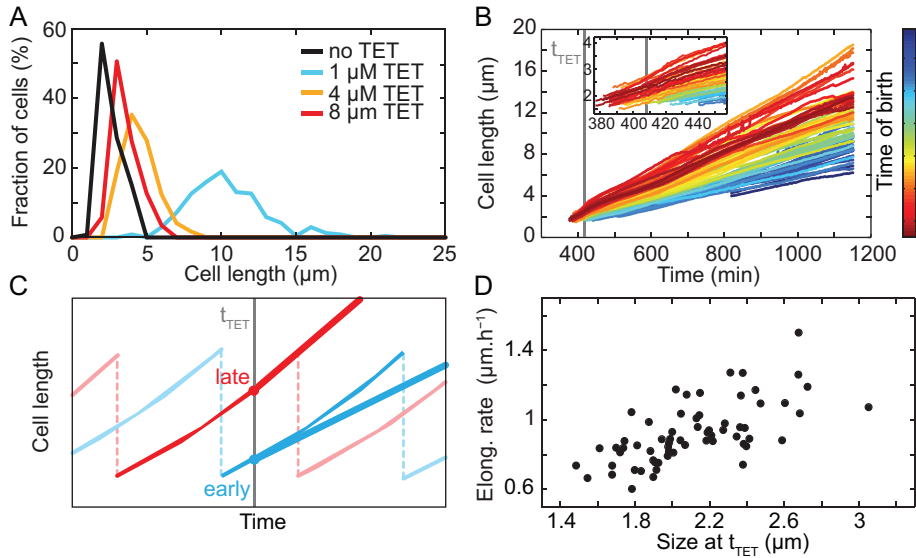


**Figure 4.3** Growth dynamics in single cells. (A) Distribution of cell lengths after 12 hours of growth in presence of 1  $\mu\text{M}$  tetracycline (blue; mean =  $10.34 \pm 2.57 \mu\text{m}$  (SD),  $N = 238$ ), 4  $\mu\text{M}$  tetracycline (yellow; mean =  $4.54 \pm 1.12 \mu\text{m}$  (SD),  $N = 122$ ), 8  $\mu\text{M}$  tetracycline (red; mean =  $3.58 \pm 0.85 \mu\text{m}$  (SD),  $N = 87$ ) and a control without tetracycline (black; mean =  $2.57 \pm 0.72 \mu\text{m}$  (SD),  $N = 133$ ). (B) Last generation of cells length in function of time for a microcolony at 1  $\mu\text{M}$  tetracycline. The colors correspond to the time of cell birth: cells born early relative to  $t_{\text{TET}}$  are red, cells born late are blue. Inset: zoom around  $t_{\text{TET}}$ . (C) Progression into the cell cycle as the main source of variability. Cells that are closer to their division at the time of tetracycline addition should grow faster (red) than cells at the beginning of their cycle (blue), continuing growth at the pre- $t_{\text{TET}}$  value. (D) Elongation rate in function of size at the time of addition of 1  $\mu\text{M}$  tetracycline.  $r^2 = 0.42$ ,  $p$ -value < 0.001,  $N = 64$ .

was maintained for about 5 hours though at a continuously decreasing rate (Fig. 4.4C, yellow trace), after which it became zero. These results suggest that maintenance of ribosome synthesis is required for continuous growth, in contrast to *lac* and *gltA* synthesis, whose expression was either zero or at low levels.

## 4.3 Discussion

Bacterial growth is characterized by various processes that all proceed continuously, including gene expression, metabolism, volume growth, and dilu-

tion. The cyclical nature of the cell cycle makes it difficult to disentangle each process separately. While metabolic reactions are catalyzed, the enzymes that catalyze these reactions continue to be expressed. Here we disrupted this cycle by inhibiting translation with the antibiotic tetracycline.

We found three regimes of growth depending on the drug concentration. At low concentrations, *lac* synthesis was partially blocked, and thus growth continued exponentially throughout the experiments. At intermediate concentrations, *lac* synthesis was completely blocked such that their number stayed constant. In that case, cells did not divide but elongated linearly for an extensive period of time. At the same time, ribosome synthesis continued at a constant rate. Synthesis of *gltA*, a TCA cycle gene, was almost fully inhibited, though some expression remained. This result indicates that metabolic activities and growth could continue with the existing *lac* enzymes. In addition, progression into the cell cycle, and the size of the cell at the time of tetracycline addition, contributed significantly to the variability in linear growth rates we observed in this regime.

At high concentrations of tetracycline, the elongation rate of the microcolony continuously decreased down to zero without reaching steady state. Here, both *gltA* and ribosome syntheses were completely shut down. Notably, the timing of synthesis arrest seemed to follow the steps of metabolism. First, the synthesis of the *lac* enzymes, precursors for the synthesis of all other components, was shut down. Then, further down the catabolic pathways, synthesis of central metabolism enzymes was arrested. Finally, ribosome synthesis, which involves anabolic processes, stopped and was followed by complete growth arrest a few hours afterwards. This could be a deliberate mechanism to make the most out

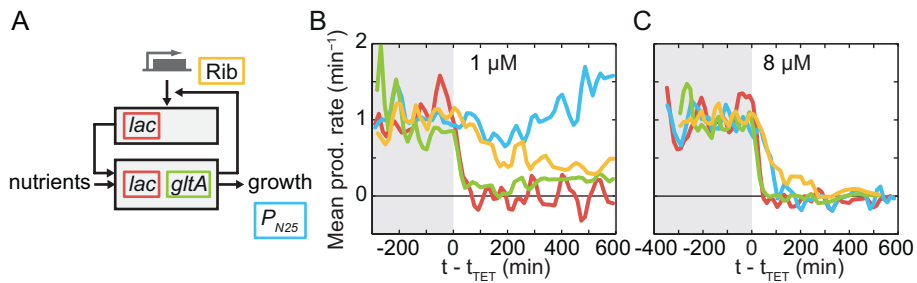


**Figure 4.4** Expression dynamics of other genes. (A) In addition of the *lac* genes (red), expression of ribosomes (yellow), the TCA cycle gene *gltA* (green) and the constitutively expressed protein  $P_{N25}$  were monitored. (B-C) Mean production rate over time of a microcolony before and after addition of 1  $\mu\text{M}$  tetracycline (B) and 8  $\mu\text{M}$  tetracycline (C).

of nutrients, as non-growing cells would experience a lag period before resuming growth.

Cells could reach sizes 20 times larger than normal after almost a day in presence of intermediate concentrations of tetracycline (data not shown). This observation indicates that no limits were imposed by diffusion, and also raises the question whether these cells were still viable. It was found for instance that the morphology of filamentous cells was reversible, and upon transfer to a fresh medium, division occurred [186]. This situation of growth at low densities might be closer to one *E. coli* cells experience in their natural environment compared to bulk cultures. Therefore, it could be relevant to bacterial resistance and activities in biofilms. In addition, it shows that single-cell growth rate measurements could be useful to develop novel antibiotics.

## 4.4 Materials and methods

### 4.4.1 Strains and media

Experiments were performed with different *E. coli* strains based on MG1655 (*rph-1 ilvG- rfb-50*). To measure expression of the *lac* operon, *lacA* was replaced with *GFPmut2* [125]. mCherry controlled by the constitutive promoter  $P_{N25}$  [195], and GFP controlled by *gltA* were inserted into the chromosome using the Datsenko & Wanner protocol [126].

Cells were grown in M9 minimal medium (as described in Chapter 2) supplemented with 0.1% (w/v) lactose (Sigma). Tetracycline (Fluka) solutions were made from powder stock, stored at -20°C in the dark and added as indicated.

Strain	Genotype	Origin
AB460	$\Delta lacA::gfp-Cam^R$	Created by A. Böhm
ASC631	$\Delta lacA::gfp-Cam^R, \Delta php::P_{N25}-mCherry-Kan^R$	This study
ASC666	$L31-mCherry-Kan^R, gltA-gfp-Cam^R$	This study

**Table 1** List of strains used in this study.



## 4.4.2 Microscopy and data analysis

Phase contrast images (300 ms exposure time with GIF filter) were taken every 70 sec; fluorescence images every 14 min (50 or 100 ms exposure). The total fluorescence and protein production rate were determined as described in Chapter 2. The production rate obtained was smoothed with the Matlab ‘smooth’ function using the ‘lowess’ method and a span of 4. The total fluorescence of the microcolony was quantified by adding the total fluorescence of each cell in the microcolony at each time point. The mean production rate of the microcolony is the mean of the production rate over all cells in the microcolony at each time point. This mean production rate was subsequently normalized to 1.

## 4.4.3 Supplementary figures

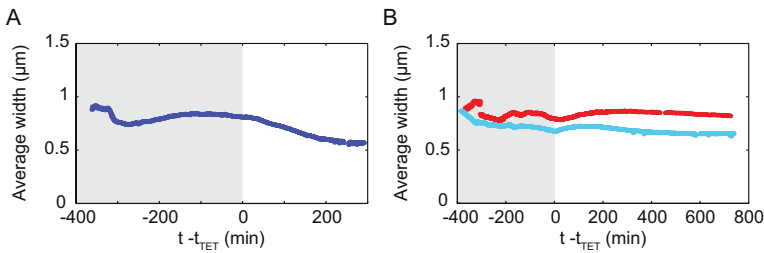


**Figure 4.5** Average width of microcolonies over time. (A) After addition of 0.5  $\mu\text{M}$  tetracycline and (B) after addition of 1  $\mu\text{M}$  (blue) or 8  $\mu\text{M}$  (red) tetracycline. While no significant change in width is observed at higher concentrations of the drug, the width decreased by 20% after addition of low amounts of tetracycline.

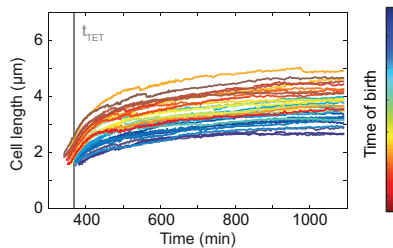


**Figure 4.6** Single-cell growth dynamics at 8  $\mu\text{M}$  tetracycline. The last generation of cells length in function of time is plotted for a particular microcolony. The colors correspond to the time of cell birth: cells born early relative to  $t_{\text{TET}}$  are red, cells born late are blue.



# **5** Noise propagation from enzyme expression to cellular growth, and back

## 5.1 Introduction

Elucidating the role of molecular stochasticity [196, 197] in cellular growth is central to understanding phenotypic heterogeneity [39, 41, 198] and the stability of cellular proliferation [199, 200]. The inherent stochasticity of metabolic reaction events [201] should have negligible effect, because of averaging over the many reactions contributing to growth. Indeed, metabolism and growth are often considered to be constant for fixed conditions [202, 203]. However, stochastic fluctuations in the expression level [40, 57, 196, 197, 204] of metabolic enzymes could produce significant variations in catalytic activity. Whether such internal fluctuations are suppressed by regulatory mechanisms [205-207] or by the secretion [208] and buffering [209, 210] of excess metabolites is unclear. Here, we used time-lapse microscopy to measure fluctuations in the expression of *lac* enzymes and in the instantaneous growth rate of single *E. coli* cells, and quantified their time-resolved cross-correlations. We found that fluctuations in the expression of a catabolically active enzyme propagate to growth, with the transmission strength depending on the mean enzyme concentration. Growth fluctuations in turn perturb expression, mediated by general growth factors rather than specific regulatory interactions. Remarkably, expression noise in one enzyme was found to transmit to other unrelated genes via growth. The results indicate that molecular noise is propagated not only by cascades of regulatory proteins [54, 55], but also by sequential metabolic reactions. Furthermore, they suggest that interplay between noise in gene expression and in metabolic activity governs the stability of cellular growth, and that growth noise is a generic source of cellular heterogeneity.

## 5.2 Results and discussion

To investigate the dynamics of cellular growth, we followed individual *Escherichia coli* cells growing on different nutrients. In particular, we used the synthetic sugar lactulose [211], which is imported and catabolized by the LacY and LacZ enzymes like its analog lactose, but unlike lactose does not induce *lac* operon expression (Fig. 5.1A). Mixtures of lactulose and the gratuitous inducer IPTG thus allowed us to vary the mean *lac* expression level independently and hence to explore different regimes of noise transmission. We determined the instantaneous growth rate  $\mu(t)$  of individual cells within microcolonies at sub-cell-

cycle resolution for various growth conditions, using time-lapse microscopy [54] at high acquisition rates and automated image analysis (see Methods in Chapter 2). We found that  $\mu(t)$  varied significantly in time, both within one cell cycle and between different cell cycles (Fig. 5.1B-C), with noise intensities (standard deviation over the mean) ranging between 0.2 and 0.4 (Fig. 5.1D). To quantify the timescales of the growth variations we computed autocorrelation functions:

$$R_{\mu\mu}(\tau) = \frac{\langle \delta\mu(t)\delta\mu(t+\tau) \rangle}{\langle \delta\mu(t) \rangle^2}$$

where  $\delta\mu(t)$  denotes the deviation of  $\mu(t)$  from the population mean  $\overline{\mu(t)}$  and angle brackets represent averaging over the branched lineage structure (Fig. 5.5). The  $R_{\mu\mu}(\tau)$  curves decreased mono-exponentially down to zero (Fig. 5.1E), with a characteristic time that was somewhat smaller than the mean cellular doubling time (Fig. 5.1F). Such a correlation time that scales with the mean doubling time is typical for concentration fluctuations of long-lived proteins, as their variations are set by volume growth and dilution [121]. Thus, the data indicated that the cells exhibited growth limitations that fluctuate randomly in time, and suggested they could be caused by variations in concentrations of cellular components.

In order to study the relation between the growth fluctuations and enzyme expression, we quantified the latter using a fluorescent protein (GFP) fused into the *lac* operon (Fig. 5.1A). The concentration of *lac* enzymes  $E(t)$ , as determined by the cellular fluorescence per unit area (Fig. 5.1G), also displayed fluctuations with autocorrelation times that scaled with the mean doubling time (Fig. 5.1H-I). Cross-correlation between *lac* expression and growth were examined by computing:

$$R_{E\mu}(\tau) = \frac{\langle \delta E(t)\delta\mu(t+\tau) \rangle}{\langle \delta E(t) \rangle \langle \delta\mu(t) \rangle}$$

$R_{E\mu}(\tau)$  quantifies whether  $E$ -fluctuations that occur now are correlated with  $\mu$ -fluctuations that occur time  $\tau$  later, and can thus inform on delays, the direction of signal transmission between  $E$  and  $\mu$ , and hence the underlying network topology [56, 57]. In addition, we quantified the production rate of *lac* enzymes  $p(t)$ , by taking the time-derivative of the total fluorescence integrated over the entire cell, and used it to determine  $R_{p\mu}(\tau)$ . When growing on lactulose, both  $R_{E\mu}(\tau)$  and  $R_{p\mu}(\tau)$  showed positive correlations regardless of the IPTG concentration (Fig. 5.2A-C,  $p < 0.02$ ). Their shapes and symmetries did depend on IPTG however. At low and intermediate IPTG,  $R_{E\mu}(\tau)$  was nearly symmetric around  $\tau = 0$  while  $R_{p\mu}(\tau)$  was asymmetric with larger weight at positive  $\tau$  (Fig. 5.2A-

B). This would indicate that  $p$  fluctuations on average correlated more strongly with  $\mu$  fluctuations that occur later. Such a delay in  $\mu$  is consistent with the idea that  $lac$  expression fluctuations produce variations in lactulose catabolism, which in turn propagate through the metabolic network and perturb growth.

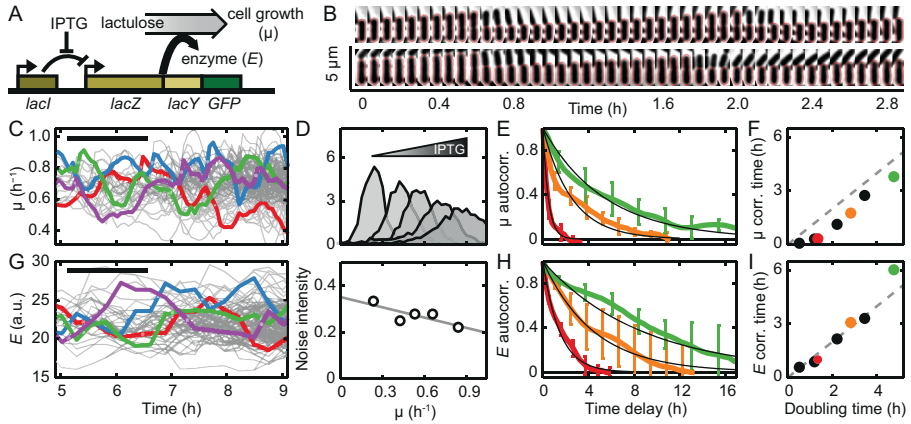


**Figure 5.1** Growth rate variability in single *E. coli* cells. (A) Lactulose is metabolized by the *Escherichia coli lac* enzymes, but does not induce  $lac$  expression. The mean  $lac$  expression can hence be varied independently by the inducer IPTG, which is not metabolized. (B) Phase contrast kymographs for two lineages. Microcolonies grew on polyacryl pads (0.1% lactulose and 200  $\mu\text{M}$  IPTG) for 8 to 9 generations. Up to 48 images were taken per hour. Red line: cell boundary from image analysis (Fig. 2.9). (C) Instantaneous growth rate against time  $\mu(t)$ , determined by fitting exponentials to the cellular length (see Fig. 2.9). Four lineages are colored for clarity. Black bar: mean division time. Light points: division events. (D) Top: Histograms of  $\mu$  values for different IPTG levels. Bottom: Noise intensity (standard deviation over the mean). (E) Autocorrelation function of  $\mu(t)$  for low (4  $\mu\text{M}$ , green), intermediate (6  $\mu\text{M}$ , ochre), and high (200  $\mu\text{M}$ , brown) IPTG levels. For clarity, error bars denoting twice the standard deviation are indicated only for a fraction of the points. Black lines: exponential fits that provide the correlation time. (F)  $\mu(t)$  correlation time versus mean doubling time. Colors are as in (E), black points are for growth on defined rich, lactose, succinate, and acetate (in order of increasing doubling time). (G-I) As panels (C), (E), and (F), but for the fluorescence intensity reporting for  $E(t)$  within single cells.

At high IPTG,  $R_{E\mu}(\tau)$  became asymmetric, and displayed a peak at negative  $\tau$  (Fig. 5.2C). These correlations at negative times indicate that  $E$  fluctuations correlate more strongly with  $\mu$  fluctuations occurring earlier, which suggests that fluctuations transmitted predominantly from growth to  $lac$  expression rather than the other way around. Such a growth-to-expression coupling could be caused by specific regulatory interactions [60, 67, 212], or they could arise more

generally when increased growth yields increased abundance of components that are required for transcription and translation. Overall, the data suggested that noise not only propagated forward, from expression to growth, but also backward, from growth to expression.

To determine whether a back and forth transmission of noise could explain the correlations we developed a minimal stochastic model. A black-box approach was followed, in which noise propagation is represented by phenomenological transmission coefficients that do not specify molecular details (Fig. 5.2D). Analytical solutions for the cross-correlation functions revealed all the contributing transmission pathways from noise source to observable ( $p$ ,  $E$ , and  $\mu$ ) through the looped network structure (see Appendix). The analysis showed the system is described by just a few noise transmission modes that generate cross-correlations of distinct shape and symmetry, and contribute additively to the overall correlations (Fig. 5.2E-G). The first two modes respectively described the transmission of expression noise to growth by *lac* catabolism, and the transmission of common noise to both growth and expression, while a third expressed the transmission of growth noise to expression by volume expansion and dilution. Despite the simplicity of the model, it reproduced detailed features of the data (Fig. 5.2H-J).

The model indicated the cross-correlation differences are explained by altered intensities of the modes. The *lac* catabolism mode (Fig. 5.2E) dominated at low and intermediate IPTG (Fig. 5.2H-I), but diminished towards higher IPTG because of decreasing strength of transmission from  $E$  to  $\mu$ . This decrease is plausible, as catalyzed reactions should become less dependent on catalyst when the latter becomes abundant. Consistently, when the population-mean *lac* enzyme concentration increased by induction, the mean growth rate initially rose steeply and then leveled off (Fig. 5.2K). On the other hand, the intensity of the common-noise mode (Fig. 5.2F) was almost constant for all IPTG concentrations, as seen by the rather constant  $R_{p\mu}(0)$  (Fig. 5.2A-C). To investigate which factors affect the transmission from common noise to expression in this mode we genetically modified different aspects of our construct. We found the coupling to remain present when we knocked-out the *lac* repressor, changed the GFP position within the operon, altered the type of fluorescent protein, or used an exogenous constitutive promoter (Fig. 5.8-10, Appendix). These data suggest that common noise couples to expression in general, though it does not exclude that additional coupling is mediated by specific regulatory interactions.

To critically assess the properties and validity of our model, we tested its ability to predict the correlations when altering the network. The model asserts that *lac* catabolism is responsible for the positively weighed  $p$ - $\mu$  correlations

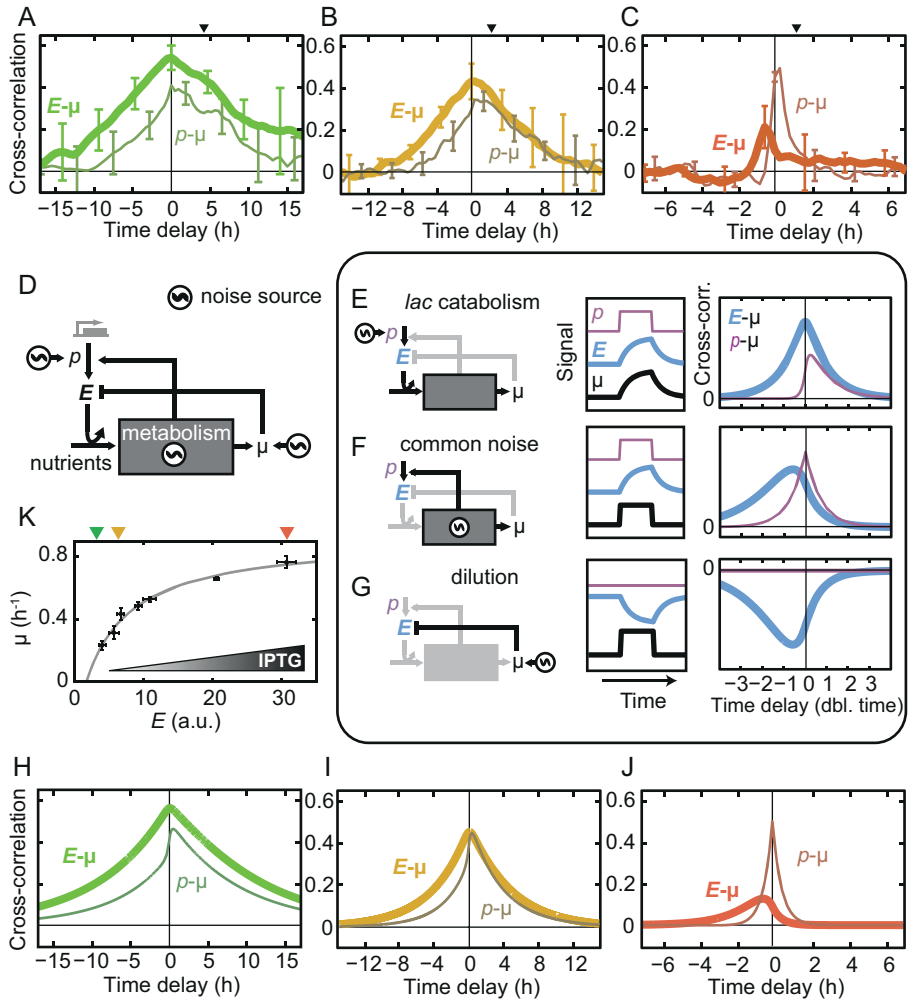


**Figure 5.2** Cross-correlation functions and mathematical model. (A-C) Cross-correlation functions  $R_{p\mu}(\tau)$  for the enzyme production rate  $p(t)$  and growth rate  $\mu(t)$  (thin line), as well as  $R_{E\mu}(\tau)$  for the enzyme concentration  $E(t)$  and  $\mu(t)$  (thick line, see Appendix). Growth is on lactulose (0.1 %) with IPTG: 4  $\mu\text{M}$  (A), 6  $\mu\text{M}$  (B), 200  $\mu\text{M}$  (C). Top triangles indicate mean division time. Error bars denoting twice the standard deviation are indicated for some data points only. The main features were robust to changing the growth determination method and taking the cell width into account (Fig. 5.6). Growth and expression differences typically did not correlate with location within the microcolony (Fig. 5.7). (D) Model for coupling between expression and growth noise. Two noise sources are specific to  $p$  and  $\mu$ , one is common to both  $p$  and  $\mu$ . (E-G) Classes of noise transmission modes resulting from theoretical analysis (see Appendix). Left: example noise source and transmission pathway. Middle:  $\mu$ ,  $p$ , and  $E$  signals in response to a block-wave emit-



ted from the noise source. The block-wave illustrates the mode dynamics; colored noise is emitted in the actual model. Right: corresponding cross-correlations. (H-J) Fits to the experimental data (panels (A-C) and Appendix). (K) The mean growth rate within microcolonies versus the mean expression level within colonies, as measured for different levels of IPTG induction. Line: fit to a Monod growth model.

when the cells are weakly induced and grow slowly (Fig. 5.2A-B). Thus, when growth is similarly slow but carbon enters central metabolism via another pathway, these correlations should become more symmetric (Fig. 5.3A). Growth on acetate also yielded slow growth (0.22 vs. 0.23 h<sup>-1</sup>).  $R_{p\mu}(\tau)$  indeed became nearly symmetric while  $R_{E\mu}(\tau)$  turned from approximately symmetric to negatively weighed (Fig. 5.3B), as predicted (Fig. 5.3A). Growth on other carbon sources allowed further probing of the nature of the observed delays. The model indicates they reflect the timescale at which  $E$  can vary, which is limited by dilution and thus much slower than other possible causes of delay such as chemical reactions. Consistently, for acetate growth, the peak-width of  $R_{E\mu}$  (Fig. 5.3A) that quantifies the delay is indeed of the same order as the doubling time (on the order of hours). Decreasing the doubling time should lead to narrower peaks, which we indeed observed when going from slow nutrients such as acetate (Fig. 5.3B) to faster ones such as lactose (Fig. 5.3D) and various other carbon sources (Fig. 5.4).

Second, the network structure implied a noise cancelling mechanism: upward fluctuations from the common noise source cause *increases* in  $E$  because of transmission via  $p$ , but at the same time they cause *decreases* in  $E$  because of transmission via  $\mu$  (Fig. 5.2D). This balance offers a direct prediction: if the positive pathway dominates,  $R_{E\mu}(\tau)$  should be positive, as is the case for all the data so far. But, if the negative pathway dominates,  $R_{E\mu}(\tau)$  should become negative (Fig. 5.3E). One cannot manipulate how volume changes affect dilution in the negative pathway. So, to tilt the balance, we looked for constructs with a weaker transmission from common noise to  $p$  in the positive pathway, which is measured by  $R_{p\mu}(0)$ . A constitutively expressed mCherry that displayed a two-fold lower  $R_{p\mu}(0)$  indeed displayed negative  $R_{E\mu}(\tau)$  at negative times (Fig. 5.3F), as predicted (Fig. 5.3E). Thus, two parallel antagonistic pathways that together form a so-called incoherent feed-forward network motif [213] can partially cancel noise. The effects of this noise cancelling is further seen in  $R_{E\mu}(0)$ , which is low at high induction despite the high  $R_{p\mu}(0)$  (Fig. 5.2C and 5.3D). Interestingly, the positive  $R_{E\mu}(\tau)$  values for *lac* expression contrasts with the observed negative dependence between the population average  $\bar{E}$  and  $\bar{\mu}$ , when  $\bar{\mu}$  is varied by growing on different carbon sources (Fig. 5.12), as has been reported previously

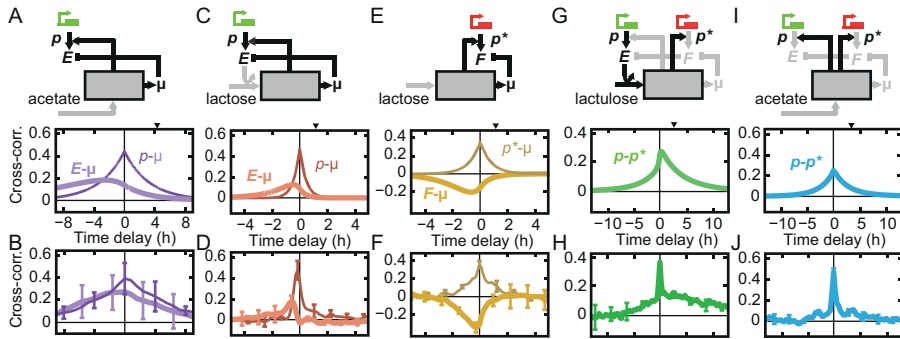


**Figure 5.3** Model predictions and experimental tests. Top: re-wired noise transmission networks with predicted dominant pathways (black). Colored genes indicate labeling with GFP and mCherry. Middle: predicted cross-correlation with mean doubling time (triangle). Bottom: measured cross-correlation. (A-B) Altered metabolic pathway due to growth on acetate. (C-D) Increased population growth rate (compared to (A-B), see also Fig. 5.4) leads to narrowing, confirming the prediction that dilution is the delay cause. (E-F) Decreased coupling from common noise to expression, leading to dominant dilution. (G-H) Transmission from the *lac* genes to another gene *via* growth. (I-J) When the *lac* genes do not transmit because cells grow on acetate, the correlation is symmetric.

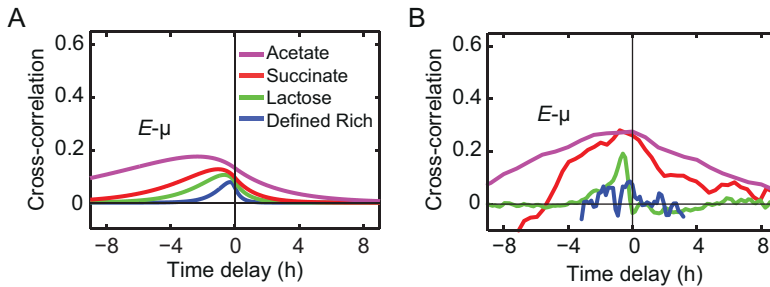


**Figure 5.4** Cross-correlations for growth on different carbon sources, in the absence of noise transmission from *lac* enzymes to growth, with growth rates ranging from 0.25 to 2 doublings per hour. (A) Theoretical cross-correlations obtained by using the parameters during growth on lactulose and changing exclusively the population average growth rate to the experimentally measured value. This prediction displays a positive asymmetric peak toward negative time and a width scaling with the average growth rate. (B) Corresponding measured cross-correlations.

[60, 67]. These opposing dependencies show that different mechanisms must play a role at different timescales.

Finally, if *lac* enzymes transmit to growth and growth transmits to expression in general, then *lac* enzymes should also transmit to other genes. To test this we studied a chromosomally inserted mCherry gene under the control of a constitutive promoter that has no known functional interaction with the GFP-labeled *lac* system. If noise in the GFP expression rate  $p(t)$  transmits to the mCherry expression rate  $p^*(t)$ ,  $R_{pp^*}(\tau)$  should display a positive peak weighing more heavily at positive  $\tau$  (Fig. 5.3G). When we grew these cells on lactulose and low IPTG, we indeed observed positively weighed GFP-mCherry correlations (Fig. 5.3H) that agreed with the predictions based on previously determined parameters (Fig. 5.3G). In contrast,  $R_{pp^*}(\tau)$  should be symmetric for growth on acetate, because the *lac* genes then do not transmit to growth (Fig. 5.3I). We indeed found  $R_{pp^*}(\tau)$  to become symmetric under these conditions (Fig. 5.3J and Fig. 5.11). Noise in *lac* expression can thus couple to other proteins without specific regulatory interactions.

Our study shows that noise in a single gene can affect the entire growth machinery of a cell, and in turn, growth noise affects the expression of potentially all other genes. This entanglement between growth and expression noise reflects the inherent cyclical nature of the reaction pathways that power self-replicating systems: metabolic enzymes catalyzing these reactions help synthesizing the building blocks for their own synthesis. The results raise the question how different fluctuating metabolic activities within the cell are coordinated, and which regulatory mechanisms are involved. Noise in metabolic systems may constitute a generic source of cellular heterogeneity [21], but also prevent optimal growth [213] and limit efficient biosynthesis. Novel approaches are required to incorporate noise transmission within the current theoretical framework of metabolism.

## 5.3 Appendix

### 5.3.1 Strains and media

Growth experiments were performed using derivatives of *E. coli* MG1655 (*rph-1 ilvG- rfb-50*), see Table 5.1. To measure expression of the *lac* operon, *lacA* was replaced with *GFPmut2* [125]. *mCherry* and *GFPmut2* controlled by the constitutive promoter  $P_{N25}$  [195] was inserted into the chromosome at different

locations using the Datsenko & Wanner protocol [126]. *LacZ-GFPmut2* fusion was performed using the Hamilton *et al.* protocol [215].

Cells were grown in M9 minimal medium with 0.2 mM uracil (as described in Chapter 2). As carbon and energy source either 0.1% lactulose (= 2.9 mM), 0.1% lactose (= 2.9 mM), 0.1% glucose (= 5.6 mM), 0.1% succinate (= 8.5 mM) or 0.12% acetate (= 20 mM) was added. When indicated, IPTG was added to the medium (0-200  $\mu$ M). Rich medium consisted of MOPS EZ Rich Defined from Teknova (Hollister, CA, USA), with 0.2% glucose as carbon source.

Strain	Genotype	Origin
AB460	$\Delta lacA::gfp-Cam^R$	Created by A. Böhm
ASC631	$\Delta lacA::gfp-Cam^R, \Delta php::P_{N25}-mCherry-Kan^R$	This study
ASC636	$\Delta lacA::gfp-Cam^R, \Delta CheZ::P_{N25}-mCherry-Kan^R$	This study
ASC638	$\Delta CheZ::P_{N25}-gfp-Kan^R$	This study
ASC639	$\Delta lacA::gfp-Cam^R, \Delta lacI::Kan^R$	This study
ASC662	<i>lacZ-gfp</i>	This study
MG22	$\Delta intC PL -lacO1::yfp$	Elowitz <i>et al.</i>
NCM520	$\Delta lacAYZ$	Coli Genetic Stock Center

**Table 5.1** List of strains used in this study.

### 5.3.2 Cell growth

Cells from -80°C glycerol stock were grown at 37°C in TY medium until they reached 0.02-0.50 OD (optical density at 600 nm, 1 cm path length). These cells were transferred at different dilutions into flasks containing M9 with glucose for growth O/N. The following day cells from a culture in exponential growth

(OD < 0.2) were diluted in their respective experimental medium and grown for at least another 11 hours, while taking care that cells did not reach stationary phase. Subsequently 1  $\mu\text{L}$  of diluted cells (OD  $\approx$  0.005) was applied on a small pre-warmed polyacrylamide gel and covered with a pre-warmed coverslip, resulting in sparsely distributed cells each growing into a single layered microcolony of about 500 cells before forming a second layer. The gel pad was placed inside a glass cavity slide containing sufficient oxygen for prolonged cell growth, and sealed in a tight sealing metal clamp to avoid drying of the sample.

Polyacrylamide gels were made by pouring 900  $\mu\text{L}$  of polyacrylamide mix (1.25 ml 40% acrylamide, 3.7 mL water, 50  $\mu\text{L}$  fresh 10% ammonium persulfate, and 5  $\mu\text{L}$  TEMED) into a cavity glass slide, covering it with a 24 mm x 60 mm silanized coverslip and letting it polymerize at room temperature for half an hour. The gel was cut in pieces of 5 mm x 10 mm, and washed with water to remove unpolymerized chemicals. Before an experiment, the gel was filled with the designated media by transferring it every few hours to large volumes of the media. Despite thorough washing of glassware and using distilled water, our gels contained organic contamination as observed by slow but significant cell growth on minimal M9 media without sugar. Such organic contaminations have also been observed for growth in batch cultures [145, 216, 217]. To make sure that cells would not use these contaminants as carbon source in experiments at low growth rate, we first grew cells with a knocked-out lac operon on the gel (strain NCM520), as to consume the organic contaminants before the actual experiment.

### 5.3.3 Correlation along lineages

We calculated how two signals correlate over time using a temporal cross-correlation. For each lineage in a microcolony, discrete time signals of growth rate ( $\mu$ ), protein concentration ( $E$ ) and protein production ( $p_E$ ) were extracted (see Fig. 5.1E-G). We made sure that correlation analysis was performed in steady-state conditions, i.e. population averages of these three signal was stationary over time. A microcolony consists of  $M$  lineages, each containing  $N$  data values separated by sampling interval  $\Delta t$ , such that data value  $n$  originates from time point  $t = n \cdot \Delta t$ . We calculated the noise in these signals as the difference between the signal and the population mean:

$$(1) \quad \tilde{\mu}_n = \mu_n - \frac{1}{M} \sum_{m=1}^M \mu_{n,m}, \quad \tilde{E}_n = E_n - \frac{1}{M} \sum_{m=1}^M E_{n,m}, \quad \tilde{p}_{E_n} = p_{E_n} - \frac{1}{M} \sum_{m=1}^M p_{E_{n,m}}$$

The cross-covariance between two signals within a single lineage at time-lag  $\tau = r \cdot \Delta t$  is defined by (shown here for  $E$  and  $\mu$ ) [131]:

$$(2) \quad C_{E\mu}(r\Delta t) = \begin{cases} \frac{1}{N-r} \sum_{n=1}^{N-r} (\tilde{E}_n \tilde{\mu}_{n+r}) & \text{if } r \geq 0 \\ C_{\mu E}(-r\Delta t) & \text{if } r < 0 \end{cases}$$

The cross-correlation within a lineage is calculated by normalizing the covariance by the product of the standard deviation ( $\sigma$ ) of the signals, which equals their auto-covariance at  $r = 0$ :

$$(3) \quad R_{E\mu}(r\Delta t) = \frac{C_{E\mu}(r\Delta t)}{\sqrt{C_{EE}(0)C_{\mu\mu}(0)}}$$

Multiple lineages can be combined into a composite cross-covariance:

$$(4) \quad C_{E\mu}(r\Delta t) = \begin{cases} \frac{1}{M} \frac{1}{N-r} \sum_{m=1}^M \sum_{n=1}^{N-r} (\tilde{E}_{n,m} \tilde{\mu}_{n+r,m}) & \text{if } r \geq 0 \\ C_{E\mu}(-r\Delta t) & \text{if } r < 0 \end{cases}$$

As our lineages are extracted from a branched data set, many data points are used multiple times in this composite cross-covariance. In order to get a composite cross-correlation that best estimates the real underlying process, it is essential to only use comparisons between unique pairs of measurement points. To correct for unequal contributions we weigh each pair of data points based on the number of lineages the data points are used in ( $\lambda$ ). Multiple contributions of the same pair of data points can be corrected using the weighing factor:

$$w_{n,m,r} = \frac{1}{\lambda_{(n+r),m}}$$

effectively resulting in the same calculation as in Dunlop *et al.* [56]). We used a weighing factor that also corrects for contributions where a single data point is used in pairs with many other data points (see Fig. 5.5):

$$(5) \quad w_{n,m,r} = \frac{1}{2\lambda_{n,m}} + \frac{1}{2\lambda_{(n+r),m}}$$

This weighing is used in the branch-corrected composite cross covariance:

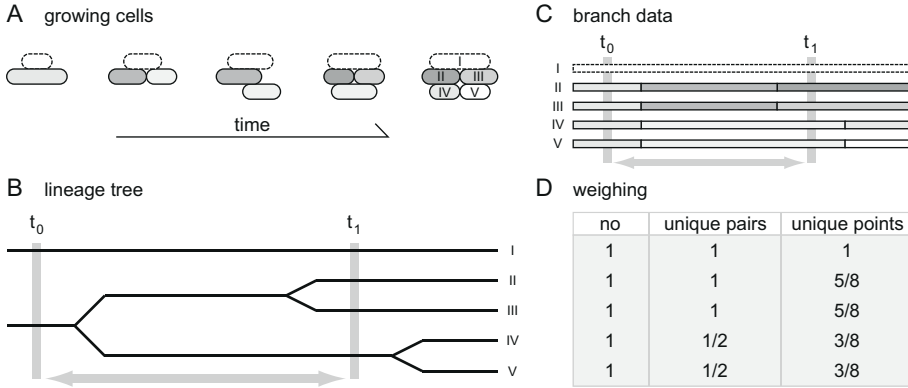


**Figure 5.5** Extracting and weighing lineages from a branched dataset. (A) Depiction of a growing microcolony over time, starting with 2 cells on the left and growing into 5 cells on the right. (B) A lineage tree of the data shown in (A). The tree starts with two lines (left), indicating the two starting cells, and at each division the line splits, resulting in five cells at the end (right). (C) Five lineages can be extracted from the data. Note that most lineages share part of their data. When correlating data points from  $t_0$  with  $t_1$ , one pair consists from completely independent data points (lineage I). Two lineages provide exactly the same pairs of data points (lineages IV and V), and two lineages only share a data point at  $t_0$  (lineages II and III). (D) Different types of weighing for the correlation of data points from  $t_0$  with  $t_1$  as used in Equation 6 in the Modelling section. No: each lineage is weighed equally. Unique pairs: weighing such that only comparisons between unique data pairs are used. Unique points: Lineages II and III are not completely independent, which can be corrected for by this weighing from Equation 5.

$$(6) \quad C_{E\mu}^M(r\Delta t) = \begin{cases} \frac{1}{w_{tot}(r)} \sum_{m=1}^M \sum_{n=1}^{N-r} (E_{n,m} \mu_{n+r,m} w_{n,m,r}) & \text{if } r \geq 0 \\ C_{\mu E}^M(-r\Delta t) & \text{if } r < 0 \end{cases}$$

$$\text{with } w_{tot}(r) = \sum_{m=1}^M \sum_{n=1}^{N-r} w_{n,m,r}$$

We calculated correlation error bars by pruning microcolony lineage trees at the stem until 4 independent branches remained. Composite correlations within these independent trees were calculated separately, and then combined to calculate the mean correlation and its standard deviation.

### 5.3.4 Modelling

#### Analytical expression of the correlations

We note  $E$  the enzyme concentration,  $p$  its production rate and  $\mu$  the rate of increase of volume. Given that enzymes are long-lived compared to the cell cycle time:

$$(1) \quad \dot{E} = p - \mu \cdot E$$

The rates  $p$  and  $\mu$  can vary due to fluctuations in the concentration or the activity of global factors (such as ribosomes, ATP, amino-acids or common regulatory elements) or due to fluctuations of specific factors, such as lacI repressor binding to the *lac* operon or enzymes catalyzing cell wall production. Hence we consider three independent noise sources:  $N_G$  is the effect of common components,  $N_E$  and  $N_\mu$  are components specific respectively to  $E$  and  $\mu$ . These  $N_X$  are modeled as independent colored noises:

$$(2) \quad \dot{N}_X = \theta_X - \beta_X N_X$$

with decay rate  $\beta_X$  and a white noise source of amplitude  $\theta_X$ . We computed analytical solutions for the time-correlations under a linear response approximation, which is suited to probe quantitatively the short term response of the network when fluctuations are of sufficiently limited amplitude. We defined the perturbed variables  $\delta X(t) = X(t) - X_0$  (where  $X_0$  is the mean of  $X$ ) and logarithmic gains  $T_{XY}$  representing how a variable  $X$  responds to the fluctuations of a source  $Y$ . Given the network of noise coupling interactions described in the main text (Fig. 5.2D), we write the following additional relations between variables  $p$ ,  $E$ , and  $\mu$ , and the noise sources  $N_G$ ,  $N_E$ , and  $N_\mu$ :

$$(3) \quad \frac{\delta \mu}{\mu_0} = T_{\mu E} \cdot \frac{\delta E}{E_0} + T_{\mu G} \cdot N_G + N_\mu$$

$$(4) \quad \frac{\delta p}{E_0 \cdot \mu_0} = T_{pE} \cdot \frac{\delta E}{E_0} + T_{pG} \cdot N_G + N_E$$

A first order development of (1) gives:

$$(5) \quad \frac{\delta E}{E_0 \cdot \mu_0} + \frac{\delta E}{E_0} = \frac{\delta p}{E_0 \mu_0} + T_{E\mu} \cdot \frac{\delta \mu}{\mu_0}$$



where the transmission of dilution fluctuations is denominated as  $T_{E\mu} = -1$ . Fourier transforms of (3-5) ( $\tilde{X}$  indicates the Fourier transform of  $X$ ) result in a linear system for  $E$  and  $\mu$  fluctuations in the frequency domain:

$$(6) \quad \begin{cases} \frac{\tilde{\delta E}}{E_0} = \frac{\mu_0}{\mu_E + i\omega} \left[ \tilde{N}_E + (T_{EG} + T_{E\mu} T_{\mu G}) \cdot \tilde{N}_G + T_{E\mu} \tilde{N}_\mu \right] \\ \frac{\tilde{\delta \mu}}{\mu_0} = \frac{\mu_0}{\mu_E + i\omega} T_{\mu E} \cdot \left[ \tilde{N}_E + (T_{EG} + T_{E\mu} T_{\mu G}) \cdot \tilde{N}_G + T_{E\mu} \tilde{N}_\mu \right] + T_{\mu G} \cdot \tilde{N}_G + \tilde{N}_\mu \end{cases}$$

where the rate  $\mu_E = \mu_0(1 - T_{E\mu} T_{\mu E} - T_{EE})$  sets the timescale of  $E$  fluctuations. Let:

$$R(\tau) = \int_{-\infty}^{+\infty} \frac{E(t)}{E_0} \frac{\mu(t+\tau)}{\mu_0} d\tau$$

be the cross-covariance between  $E$  and  $\mu$  normalized by their mean,  $A_E$  and  $A_\mu$  their respective auto-covariance. In the frequency domain we have:

$$(7) \quad \tilde{R}_{\mu E} = \left\langle \frac{\tilde{\delta \mu}}{\mu_0} \cdot \frac{\tilde{\delta E}^*}{E_0} \right\rangle \quad \tilde{R}_E = \left\langle \frac{\tilde{\delta E}}{E_0} \cdot \frac{\tilde{\delta E}^*}{E_0} \right\rangle \quad \tilde{R}_{\mu\mu} = \left\langle \frac{\tilde{\delta \mu}}{\mu_0} \cdot \frac{\tilde{\delta \mu}^*}{\mu_0} \right\rangle$$

Using the independence between noise sources (2) together with (6-7), cross-covariance in the time domain is:

$$(8) \quad \begin{aligned} R_{\mu E}(\tau) = & 1 \cdot T_{\mu E} \cdot S_E(\tau) + (T_{EG} + T_{E\mu} T_{\mu G}) \cdot T_{\mu E} (T_{EG} + T_{E\mu} T_{\mu G}) \cdot S_G(\tau) + \\ & T_{E\mu} \cdot T_{\mu E} T_{E\mu} \cdot S_\mu(\tau) + (T_{EG} + T_{E\mu} T_{\mu G}) \cdot T_{\mu G} \cdot A_G(\tau) + T_{E\mu} \cdot 1 \cdot A_\mu(\tau) \end{aligned}$$

Each term of the sum on the right-hand side of equality (8) is the product of three factors separated by dots respectively representing: fluctuations transferred to  $E$ , fluctuations transferred to  $\mu$ , and a  $\tau$ -dependent function quantifying delayed correlation arising from a particular noise source. We find these functions have one of two forms:  $S_X$  (symmetric) or  $A_X$  (asymmetric, negatively delayed), which are inverse Fourier transforms of the frequency dependent components of the cross-correlation (obtained following the method described in details in [56]):

$$(9) \quad S_X(\tau) = \theta_X^2 \frac{\mu_0^2}{2(\beta_X^2 - \mu_E^2)} \left( \frac{e^{-\text{sgn}(\tau) \cdot \mu_E \tau}}{\mu_E} - \frac{e^{-\text{sgn}(\tau) \cdot \beta_X \tau}}{\beta_X} \right)$$

$$(10) \quad A_X(\tau) = \begin{cases} \theta_X^2 \left( \frac{\mu_0}{(\beta_X^2 - \mu_E^2)} e^{\mu_E \tau} - \frac{\mu_0}{2\beta_X(\beta_X - \mu_E)} e^{\beta_X \tau} \right) & \text{if } \tau < 0 \\ \theta^2 \frac{\mu_0}{2\beta_X(\beta_X - \mu_E)} e^{-\beta_X \tau} & \text{if } \tau \geq 0 \end{cases}$$

The first three terms of (8) correspond to the symmetric modes generated by direct transmission fluctuations from  $E$  to  $\mu$ , originating from  $N_E$ ,  $N_G$  and  $N_\mu$  (Fig. 5.2E). These modes thus depend on *lac* catabolism (they disappear when  $T_{\mu E} = 0$ ), and are hence named ‘*lac* catabolism’ modes (see Fig. 5.2E). The fourth term represents the asymmetric contribution arising from the joint dependence of protein synthesis and cell volume increase on noise in common factors, and was hence named the ‘common noise’ mode (see Fig. 5.2F). The fifth term is the asymmetric contribution originating from the effect of volume growth on enzyme concentration by dilution ( $T_{E\mu} = -1$ ), and was thus termed the ‘dilution’ mode (see Fig. 5.2G). Similarly, we obtain analytical expressions for the auto-covariance for  $\tau \geq 0$ :

$$(11) \quad R_{EE}(\tau) = S_E(\tau) + (T_{EG} + T_{E\mu} T_{\mu G})^2 \cdot S_G(\tau) + T_{E\mu}^2 \cdot S_\mu(\tau)$$

$$(12) \quad \begin{aligned} R_{\mu\mu}(\tau) &= T_{\mu E}^2 \cdot A_E(\tau) + 2 \frac{\mu_E}{\mu_0} T_{\mu E} (T_{EG} + T_{E\mu} T_{\mu G}) \cdot S_G(\tau) + \\ &2 \frac{\mu_E}{\mu_0} T_{\mu E} T_{E\mu} \cdot S_\mu(\tau) + T_{\mu G} \cdot B_G(\tau) + B_\mu(\tau) \end{aligned}$$

$$\text{where } B_X(\tau) = \frac{\theta_X^2}{2\beta_X} e^{-\beta_X \tau}$$

The cross-covariance function between the production rate and growth rate is obtained in the same way:

$$(13) \quad \begin{aligned} R_{p\mu}(\tau) &= T_{EG} \cdot T_{\mu G} \cdot B_G(\tau) + T_{EE} \cdot T_{\mu E} \cdot \left[ S_E(\tau) + (T_{EG} + T_{E\mu} T_{\mu G})^2 S_G(\tau) + T_{E\mu}^2 S_\mu(\tau) \right] + \\ &T_{EE} (T_{EG} + T_{E\mu} T_{\mu G}) \cdot T_{\mu G} \cdot A_G(-\tau) + T_{EG} \cdot T_{\mu E} (T_{EG} + T_{E\mu} T_{\mu G}) \cdot A_G(\tau) + \\ &T_{EE} T_{E\mu} \cdot 1 \cdot A_\mu(-\tau) + 1 \cdot T_{\mu E} \cdot A_E(\tau) \end{aligned}$$

In the case of a second constitutively expressed gene  $F$ , we computed similarly the different types of correlation functions, assuming the response of the production rate  $p^*$  to be:

$$(14) \quad \frac{\delta p^*}{F_0 \cdot \mu_0} = T_{FE} \cdot \frac{\delta E}{E_0} + T_{FG} \cdot N_G + N_F$$

## Fitting parameters for growth experiments on lactulose

Parameters of the model are the average growth rate  $\mu_0$ , the characteristics of the noise sources  $\{\theta_E, \beta_E, \theta_\mu, \beta_\mu, \theta_G, \beta_G\}$  and the transfer coefficients  $\{T_{\mu E}, T_{EE}, T_{EG}, T_{\mu G}, T_{E\mu}\}$ .  $T_{E\mu} = -1$  accounts for physical dilution. As  $T_{EG}$  and  $T_{\mu G}$  are determined modulo a renormalization constant of the amplitude of  $N_G$ , we arbitrarily set  $T_{\mu G} = 1$ . All the other parameters were determined from experimentally measured timescales, noise intensities and correlations at  $t = 0$  as detailed below, with the exception of  $T_{EG}/T_{\mu G}$  (ratio of the response the *lac* operon promoter and  $\mu$  to common noise  $N_G$ ), which could be set to a unique value of 1.3 to match the shape of all the time-correlation functions across all experiments.

More specifically, the population average growth rate  $\mu_0$  was measured experimentally. Timescales  $1/\beta_\mu$  and  $1/\beta_G$  (growth and global noise sources) were taken equal to the measured autocorrelation time of growth rate fluctuations. Transfer coefficient  $T_{\mu E}$  for fluctuations from  $E$  to  $\mu$  was taken from the average slope of the clouds of Fig. 5.13. Feedback of  $E$  on itself  $T_{EE}$ , which only impacts the characteristic time of  $E$  fluctuations (see Equation (6)), was taken to match  $\mu_E$  the experimental decay rate of  $E$  autocorrelation. The amplitudes of the noise sources  $\{\theta_E, \theta_\mu, \theta_G\}$  were determined from the experimentally measured triplet  $\{R_{EE}(0), R_{\mu\mu}(0), R_{\mu E}(0)\}$  by solving the linear system obtained from equations (8, 11, 12) in real time space at  $t = 0$ . Timescale for specific noise of *lac* enzyme production ( $1/\beta_E$ ) was tuned to fit  $R_{\mu\mu}(0)$  and corresponded to timescales already reported for gene specific noise (-9 min in doubling units [54]). Parameter values are summarized in Table 5.2.

## Predictions for rewired networks

Prediction for the lactose experiment (Fig. 5.3C) has been taken identical to the fit for lactulose at high induction (Fig. 5.2J). For the other conditions of Fig. 5.3, average growth rate  $\mu_0$  was measured directly. Following the trends observed on lactulose experiments, we took  $\beta_\mu = \beta_M = 2\mu_0$  and  $1/\beta_E = 9$  min. For  $T_{\mu E}$  and  $T_{EE}$ , we took the values found for lactulose experiments at the same induction level, otherwise zero when the enzyme was in excess or inactive. We considered  $T_{EG}/T_{\mu G}$  to be promoter specific and kept the value of 1.3 for the *lac* operon. We found  $T_{CG}/T_{\mu G} = 0.7$  for the exogenous constitutive promoter independently of the genomic location of its chromosomal insertion.  $\theta_E$ ,  $\theta_\mu$  and  $\theta_G$

were fitted to reproduce the experimentally measured values  $R_{EE}(0)$ ,  $R_{\mu\mu}(0)$  and  $R_{p\mu}(0)$ . In all cases, the cross-correlation between growth rate and gene concentration was fully predicted.

	lactulose + 4 $\mu$ M IPTG	lactulose + 6 $\mu$ M IPTG	lactulose + 200 $\mu$ M IPTG	acetate	lactose, P <sub>N25</sub>	lactulose + 6 $\mu$ M IPTG (2 colors)	acetate (2 colors)
	<i>Fig. 5.2H</i>	<i>Fig. 5.2I</i>	<i>Fig. 5.2J and 3.3C</i>	<i>Fig. 5.3A</i>	<i>Fig. 5.3E</i>	<i>Fig. 5.3G</i>	<i>Fig. 5.3I</i>
$\mu$ (h <sup>-1</sup> )	<b>0.16</b>	<b>0.29</b>	<b>0.58</b>	<b>0.15</b>	<b>0.63</b>	<b>0.24</b>	<b>0.20</b>
$\beta_p = \beta_M$ (h <sup>-1</sup> )	0.23	0.40	2.24	0.31	1.26	0.49	0.40
$\beta_E$ (h <sup>-1</sup> )	3.90	4.20	5.10	4.85	4.85	4.85	4.85
$\eta_E$	1.03	0.78	0.48	-	-	0.78	0.60
$\eta_\mu$	0.16	0.12	0.03	0.07	0	0.12	0.07
$\eta_G$	0.22	0.19	0.22	0.24	0.17	0.19	0.24
$T_{EE}$	1	0.68	-0.23	0	-	0.68	0
$T_{\mu E}$	0.7	0.5	0	0	-	0.5	0
$T_{EG}$	1.3	1.3	1.3	1.3	-	1.3	1.3
$\eta_F$	-	-	-	-	0.3	0.3	0.3
$T_{FE}$	-	-	-	-	0	0.5	0
$T_{FG}$	-	-	-	-	0.7	0.7	0.7

**Table 5.2** Parameters value used to fit the data obtained during growth on lactulose for different IPTG concentrations (first 3 columns corresponding to model fits Fig. 5.2A-C represented on Fig. 5.2H-J) and for the predictions of the rewiring experiments (Fig. 5.3 ACEGI). Population average growth rate is measured and indicated in bold. Grey boxes correspond to parameters inferred from other experiments with similar conditions, as explained above. The noise sources amplitudes are expressed as the standard deviation of the random variable  $N_x$  which corresponds to  $\eta_x = \theta_x / \sqrt{2\beta_x}$

The correlation between the production rates  $p$  of *lac* enzyme and  $p^*$  of mCherry under a constitutive promoter (Fig. 5.3G and I) were fully predicted: we took the parameters already obtained from the experiments on the same growth medium, assumed that noise transmission from the *lac* catabolism affected similarly the production rate of *lac* and the production rate of the constitutive gene ( $T_{CE} = T_{EE}$ ), and arbitrarily took the same noise level  $\eta_F$  for the constitutive promoter as measured on lactose.

### 5.3.5 Supplementary figures

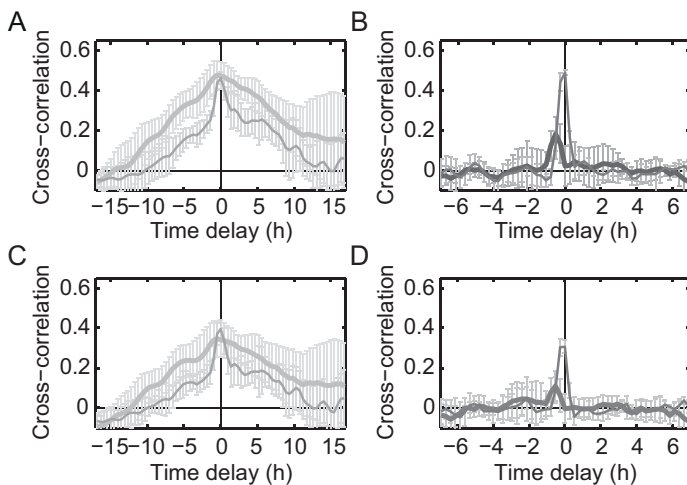


**Figure 5.6** Cross-correlations based on different methods of growth-rate determination. (A) Cross-correlations for lactulose growth at low IPTG (4  $\mu\text{M}$ ), with growth rate determined as follows:  $S(t)$  is the surface area of the cell silhouette vs. time (see Fig. 2.9). The growth rate is the time derivative of  $S(t)$ . (B) Idem, for lactulose growth at high IPTG (200  $\mu\text{M}$ ). (C) Cross-correlations for lactulose growth at low IPTG (4  $\mu\text{M}$ ), with growth rate determined as follows:  $S(t)$  is the surface area of the cell silhouette vs. time,  $L(t)$  is the length of the cell silhouette vs. time. The growth rate is the derivative of  $L(t) \cdot (S(t)/L(t))^2$ . Note that  $S(t)/L(t)$  is taken as a measure for the width of the cell, and the width squared times the length as a measure for the cell volume. (D) Idem, for lactulose growth at high IPTG (200  $\mu\text{M}$ ). These cross-correlations display the same shape and symmetry as in Fig. 5.2A and C, where the growth rate is determined as the derivative of the length of the cell silhouette. Hence the central features are robust to different methods of growth rate determination.

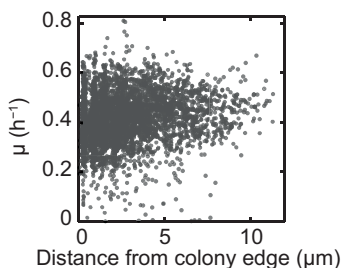


**Figure 5.7** Scatter plot of instantaneous growth rate and cell position within the microcolony. The cell position was calculated as the minimal distance of the center of a cell to the edge of the microcolony. Data obtained during growth on laculose at intermediate IPTG induction (6  $\mu\text{M}$ ).

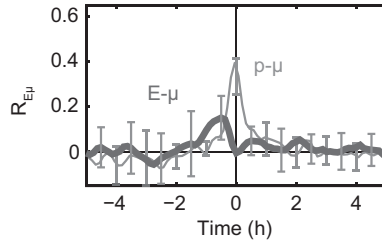


**Figure 5.8** Cross-correlation functions after knocking out the *lac* repressor LacI, at high *lac* expression (lactose minimal medium). The data is similar as before the knock-out at high expression (Fig. 5.2C), showing that the correlations are not mediated by *lac* repressor regulation.

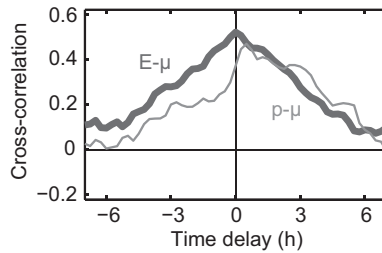


**Figure 5.9** Cross-correlation functions after changing the position of the GFP gene within the *lac* operon, at intermediate *lac* expression (0.1% lactulose and 6  $\mu$ M of IPTG). Here GFP is fused translationally to *LacZ*. The data is similar as before changing the GFP position (Fig. 5.2B), showing that the position within the operon is not critical.

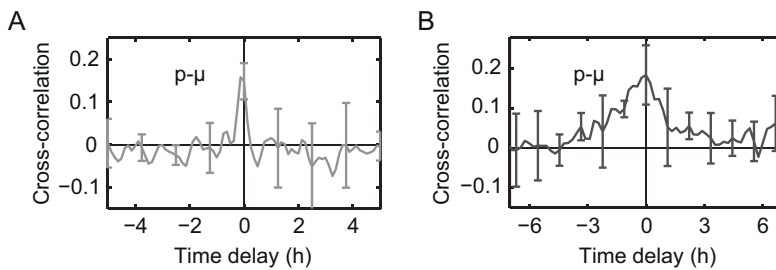


**Figure 5.10** Cross-correlation functions for two different constructs: (A) For an exogenous constitutive promoter ( $P_{N25}$ ) driving the production of GFP, inserted in the *CheZ* locus. Growth is on minimal medium with lactose. (B) For a *lac* promoter driving the production of YFP, inserted in the *intC* locus. Growth is on minimal medium with maltose. Both experiments show the presence of a coupling from common noise to expression.

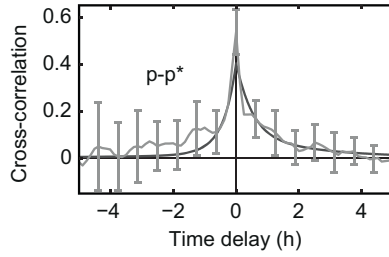


**Figure 5.11** Cross-correlation between GFP production rate ( $p$ ), reporting for the *lac* expression rate, and the mCherry production rate ( $p^*$ ). Growth is on minimal medium with 0.1% lactose. Model (black line) and experiment (green). The prediction is similar as in Fig. 5.3I, as the transmission by *lac* metabolism is low at high IPTG because *lac* enzymes are in excess.

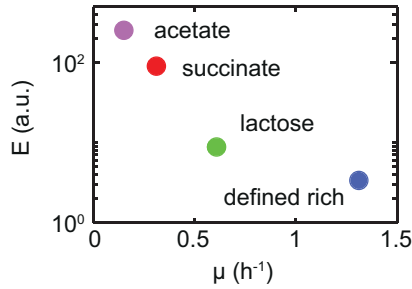


**Figure 5.12** Population average *lac* enzyme concentration versus the population average growth rate on minimal medium supplemented with varying carbon sources.

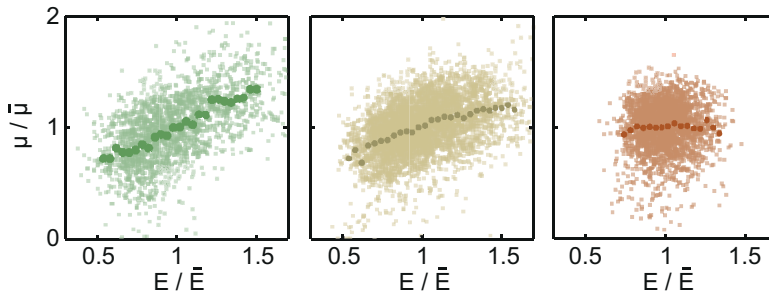


**Figure 5.13** Scatter plots of the growth rate and the enzyme concentration normalized by their average. Darker dots indicate the  $\mu$  average over bins of  $E$ . These plots have been obtained for increasing IPTG induction levels on minimal medium and lactulose 0.1%: from left to right, IPTG = 4  $\mu\text{M}$ , 6  $\mu\text{M}$  and 200  $\mu\text{M}$ .

*The mathematical model reported in this chapter was done by Philippe Nghe.*



## Transient dynamics during nutrient shifts

### 6

*Sensing of the availability of external nutrients and adjusting the genetic expression is of crucial importance for bacterial survival and growth in fluctuating environments. Despite decades of investigation of growth limitations and environmental shifts, several aspects of growth regulation and the underlying regulatory mechanisms remain unclear. This chapter is a preliminary study of the transient dynamics of growth and ribosomes synthesis during adaptation to a new steady-state, from limiting to non-limiting glucose and vice-versa. We use a single-cell approach combined with microfluidics to monitor accurately the growth rate of cells while controlling precisely the environment. The data show that adaptation to a higher growth rate is slow while adaptation to a lower growth rate is comparatively faster. To our knowledge, no mechanism has been put forward to explain the observed slow dynamics of growth rate increase, and further work could aim to that direction.*

## 6.1 Introduction

Bacterial cells possess genetic and metabolic regulatory systems that allow them to adjust their growth rate when environmental conditions change. Because they depend on external nutrients to maintain and expand their cellular machinery, our understanding of physiological regulation in bacteria has progressed thanks many studies both in steady-state conditions of growth and in changing nutritional conditions [68, 218-220]. The starting point was perhaps the work of Schaechter *et al.* fifty years ago, who established that the macromolecular composition of cells (amount of DNA, RNA and proteins) depends only on the growth rate and not on the details of the composition of media [218]. As a result, the growth rate dependence of a large number of parameters has been measured in *Escherichia coli* [221]. A question then arises: how do cells transition from one steady-state to the other? This is what Schaechter *et al.* investigated in another paper [68]. They performed a shift-up from slow to fast growth and a downshift from fast to slow growth rate, and measured how DNA, RNA and proteins changed with growth rate. In these experiments, cells were transferred or washed to a very different medium, which can be a complication when elucidating the interplay between regulatory mechanisms of the cell and its physiology. In addition, it is difficult to determine precisely the growth rate in these experiments, and only cell mass can be inferred from optical density (OD) measurements. Chemostats were invented in 1950 to cultivate cells in a well-defined, constant and controllable environment. This bulk technique was used in multiple areas of microbiology, to study evolution [222], selection [223], nutrient limitations [224, 225], kinetics of growth [226] and microbial ecology [227, 228] in various species. In practice, the use of chemostats can be complicated by problems of mixing [229]. Though chemostats made it possible to modulate the growth rate without changing the growth medium but simply by changing the quantity of nutrient [230], they give information at the population level, which can mask the true dynamics because of cell-to-cell variability. In general, growth rate regulation at the single-cell level and the underlying regulatory mechanisms has remained an important issue. Hence, new techniques are needed to study single cells.

Growth regulation is closely coupled to the control of ribosome synthesis which, in turn, determines the rate of protein synthesis. In *E. coli* for instance, the number of ribosomes in the cell correlates linearly with the growth rate [221]. This chapter is a preliminary work, where we studied the transition dynamics between limited nutrient and excess of nutrient in a microfluidic device. We moni-

tored simultaneously the growth rate of single cells and ribosome synthesis. We found that, during upshift, adaptation to the new growth rate was very slow and spanned 4 generations, corresponding to 5 hours. Production rate of ribosomes increased to the new rate within roughly the same time. However, the transition from high to low growth rate was faster and the new steady-state for growth and ribosome synthesis was reached after 2 generations only, or 3 hours. In both cases however, the response of single cells to nutrient shifts was quite homogeneous.

## 6.2 Results and discussion

### 6.2.1 Cellular growth response to glucose upshift

We started with a single cell and after a few generations of growth on a minimal medium containing a limiting concentration of glucose (2.77  $\mu\text{M}$ ), we switched to a minimal medium with abundant glucose (5.55 mM). Having previously determined the dependence of growth rate on glucose concentration (see Chapter 3), we chose these glucose concentrations in order to get a twofold change in growth rate upon nutrient shift, from a doubling time of 120 min to one of 60 min. We monitored expression of the exogenous constitutive promoter  $P_{N25}$  using GFP labeling, and the expression of ribosomes using mCherry labeling (Material and methods).

Bacteria are bigger when they grow faster, and in the case of *E. coli*, both the length and the width, and hence the volume, change upon nutrient shift [218]. Here we examined the dynamics of length, width and volume increase during the shift-up at the single-cell level. The lengths of the cells were determined using phase contrast images acquired every 1 to 2 min, and custom image analysis software (see Methods and Chapter 2). Width was calculated by dividing the cell's area by its length. Volume was calculated with the hypothesis that the cells are perfectly rod-shaped (detailed in Methods). First we considered the sum of the length of all cells in the microcolony, as well as the summed width and volume (Fig. 6.1A). Before the shift, all three parameters increased exponentially, resulting in straight lines on the log plot, except for the width that increased with steps, corresponding to cellular divisions. In addition, all parameters increased at roughly the same rate, indicating steady-state growth. Upon shift, these parameters adapted to the new rate with different delays. Fitting exponentials through the length trace at steady-state before and after the shift, indicated a doubling

time of 100 min and 70 min respectively. Surprisingly, the length responded immediately with first a transient decrease in rate that lasted 40 min followed by a gradual adaptation to the new rate. The origin of this decrease is unclear. The volume and the width continued to increase at the old rate for about 120 min after the shift, at which point the old rate changed abruptly to the new rate. Similarly, the rate of cell division, inferred by the number of cells over time (Fig. 6.1B), remained approximately constant for more than 200 min after the upshift. This rate maintenance of cell division is a well understood phenomenon and has been observed for nutrient upshifts in batch cultures [68]. It is the sum of C and D periods, which corresponds to the time for new initiations of DNA replication to be associated with new cell divisions. Here the delay is longer than the sum of C and D periods (about 100 min, see [231]), suggesting that other mechanisms are involved.

These delays can also be seen on Fig. 6.1C where the mean length, width and volume over time are plotted for the microcolony. Note that the width decrease at the beginning of the experiment is a phase contrast imaging artefact: cells that have neighbors appear thinner than those that do not, and they become more dominant over time. The length and volume saw-tooth patterns are due to the cells being in synchrony at the beginning of the experiment. This synchrony was slowly lost over time, resulting in the loss of these patterns. We are however interested in the trend on top of these oscillations. All three parameters exhibited transient dynamics, followed by a leveling-off indicating that steady-state was reached 200 to 300 min after shift-up. The mean width increased from 0.50  $\mu\text{m}$  to 0.58  $\mu\text{m}$ , while the mean volume increased from 0.50 to 0.66  $\mu\text{m}^3$ . In addition, the width seemed to increase more slowly than the length. We did not observe any immediate decrease in mean cell length or width upon shift-up, as might have been caused by the rise in osmolarity when switching to higher glucose concentration (from 275 to 280  $\text{mOsm}\cdot\text{L}^{-1}$ ). Upon a threefold change in growth rate in batch cultures [232], both mean cell length and width, determined from electron micrographs, reached their new steady-state value in about 2 and 3 hours respectively. This is in agreement with our findings, though contrary to this study we did not observe any overshoot in cell length upon shift-up. A possible explanation is detailed below.

The most striking observation is that it took the cells considerable amount of time to reach the new faster growth rate (Fig. 6.1D). Indeed, steady-state growth was achieved only 300 min after the time of shift, corresponding to 4 generations. This result is however in line with a previous study where cells growing in a chemostat with limited glucose were shifted to an excess of glucose [233]. A possible explanation is that the growth dynamics depends on the chemi-

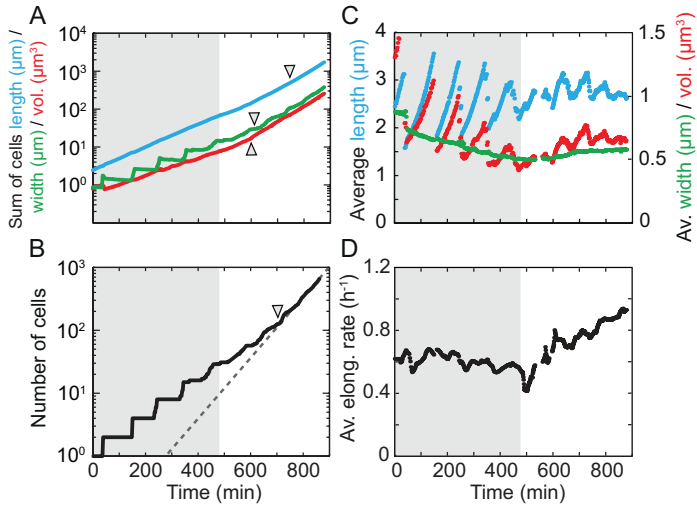


**Figure 6.1** Growth dynamics during upshift at the population level. (A) Sum of cells length (blue), width (green) and volume (red) over time of one microcolony. Note that the volume trace has been slightly shifted vertically for clarity. Arrows indicate when the new steady-state rate was reached. (B) Number of cells of the microcolony over time. The dashed line is added to guide the eye. (C) Mean cell length (blue), width (green) and volume (red) over time of the microcolony. (D) Mean elongation rate of the microcolony over time. The time of shift is indicated by the transition from grey to white background.

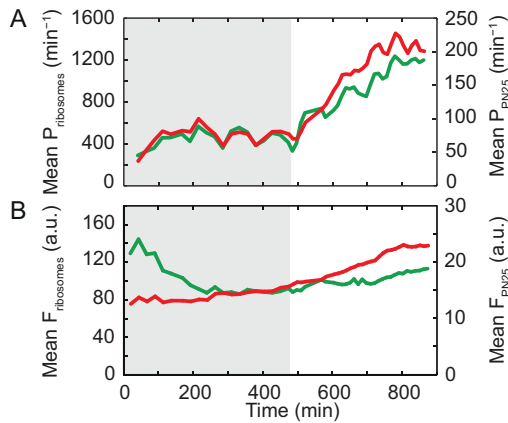


**Figure 6.2** Expression dynamics of ribosomes and of a constitutive gene during upshift. (A) Mean production rate of ribosomes (red) and  $P_{N25}$  (green) of the microcolony. (B) Mean fluorescence of ribosomes (red) and  $P_{N25}$  (green) of the microcolony.

cal composition of the different media [70]. In most nutrient upshifts in batch cultures, it is the quality of the nutrient that is changed [68, 70, 71, 72, 232, 234]. It involves reorganization of biosynthetic pathways and synthesis of essential enzymes. The rate of cell mass increase, as inferred by OD measurements, adapted to the new rate almost immediately upon shift-up, while the rate of cell division was maintained for roughly 1 hr before increasing abruptly to the new steady-state rate. Note that in our experiments we measure cell volume instead of cell mass, and during the transition between two steady-states these two quantities are not necessarily coordinated.

Our results also differ from glucose pulse experiments in chemostats, where the glucose concentration is transiently increased on a very short time scale (a few minutes). In these studies, a threefold immediate (less than 1 min) increase in growth rate was reported [235, 236]. It is not clear why cells respond differently to glucose pulse compared to a prolonged excess of glucose. This would suggest that cells growing at low rates contain sufficient enzymes to transiently grow at a faster rate, but they would still need a few hours to reach a steady-state of growth.

## 6.2.2 Transient dynamics of ribosome synthesis during upshift

Because ribosomes are known to be a major growth-limiting resource in continuous culture bulk experiments [237], we followed ribosome synthesis to get insight into the slow growth dynamics observed. The total fluorescence of each cell was determined by extracting the pixels that were within the cell outline. The ribosome production rate was then measured by taking the slope of the best linear fit over the total fluorescence signal over three consecutive time points. The cell mean fluorescence is determined as the mean of pixels within the cell outline (see Materials and methods). Note that the cell volume plays a role in the determination of ribosome concentration, but not in the production rate.

During slow growth at the lower glucose concentration, the mean ribosome production rate of the microcolony was constant at about  $400 \text{ min}^{-1}$ . Upon shift-up, the production rate increased steeply by more than twofold after a delay of roughly 30 min (Fig. 6.2A, red trace). After this first fast increase, the production rate continued to rise slowly and continuously until the new steady-state value of  $1300 \text{ min}^{-1}$ , which was reached 250 min after the time of shift. The mean fluorescence of the microcolony, corresponding to the mean ribosome concentration, followed different dynamics (Fig. 6.2B, red trace). Upon shift-up, ribosome

concentration increased slowly and reached its new steady-state value about 1 hr later than the production rate (Fig. 6.1B). A previous study in a chemostat [238] found that, upon upshift in dilution rate (from 0.2 to 0.6 h<sup>-1</sup>), ribosome concentration gradually increased and reached a stable concentration in about 6 hrs, which is in line with our results. Overall, the ribosome concentration increased by a factor 1.8 compared to the pre-shift value, which corresponds to a 2.5-fold increase in the number of ribosomes given the volume increase, which is also consistent with previous measurements [221].

As a control, we also monitored the expression of a constitutive promoter, P<sub>N25</sub>. The mean P<sub>N25</sub> production rate, as the ribosome production rate, had a low constant value of approximately 60 min<sup>-1</sup> during slow growth on low glucose (Fig. 6.2A, green trace). Upon shift-up, the P<sub>N25</sub> production rate increased immediately and gradually until steady-state. Both ribosome and P<sub>N25</sub> production rates increased by the same factor 3 compared to their respective pre-shift values.

Before the shift the mean P<sub>N25</sub> fluorescence showed an initial decrease, likely due to adaptation to growth in the microfluidic device, before reaching a steady-state value. Upon upshift, the fluorescence increased slightly and remained rather constant until the end of the experiment. Note that even though the production rate trends of ribosome and P<sub>N25</sub> are quite the same, for the concentration trends are quite different. While the ribosome concentration follows expected trends (positive correlation with growth rate), the results for P<sub>N25</sub> seem to be at odds with a recent theoretical study that found that the concentration of constitutive genes decreases when the growth rate increases [60]. This difference is unclear.

### 6.2.3 Single-cell dynamics during upshift

We next investigated the response of growth and ribosomes at the single-cell level (Fig. 6.3). Qualitatively, the single-cell responses to nutrient shift are rather similar to the population response. Fig. 6.3B represents the distribution of the ribosome production rate at three different time points. First, a few minutes before the time of shift (top), during the transition to the new rate (middle), and at the end of the experiment when steady-state was reached (bottom). The shape of the histograms was quite similar, with no bimodality observed. In addition, the coefficient of variation (Fig. 6.3C) stayed at a constant value of about 0.25 throughout the experiment. Oscillations at the beginning of the experiment are due to the low number of cells. A similar shape for distributions and coefficient of variation value over time of 0.20 was obtained for elongation rate (data not

shown). These results confirm the rather homogeneous response of single cells to the nutrient upshift.

#### 6.2.4 Correlation between growth rate and ribosome production rate

Since ribosomes are considered to be growth-limiting and the growth rate is determined primarily by ribosome concentration (and their rate of translation), the next logical step is to look at correlations between growth and ribosomes. Fig. 6.4A is a scatter plot of elongation rate versus ribosome production rate, where each point represents a cell cycle and cells are colored according to their generation number. Elongation rate and ribosome production rate are well correlated ( $r^2 = 0.50$ ,  $p$ -value  $< 0.001$ ,  $N = 655$ ). Note that significant random variability is observed before (blue clouds) and after the transition (red cloud). However, these variations in elongation rate and ribosome production rate are only weakly correlated (e.g.  $r^2 = 0.10$ ,  $p$ -value  $< 0.001$ ,  $N = 177$ ; for cells in generation 9). One implication is that some cells grow at the maximal growth rate at a ribosome production rate of about  $2000 \text{ min}^{-1}$  while other cells achieve the same growth rate with half that ribosome production rate.

We found that the increase in growth rate was tightly correlated with the ribosome production rate (Fig. 6.5B-C). If cells needed to produce more ribosomes to increase their growth rate, we could have expected growth to increase after ribosome production rate. Here, it is not clear whether changes in ribosome production rate precede changes in growth rate, or vice versa, as both seem to increase simultaneously.

#### 6.2.5 Cellular growth response to glucose downshift

We next investigated the cells response to nutrient downshift. After a few generations of growth on a minimal medium containing abundant glucose ( $55.5 \mu\text{M}$ ), we switched to a minimal medium containing limiting glucose ( $2.77 \mu\text{M}$ ). We should get a twofold change in the doubling time, from 60 min to 120 min, which is similar to the nutrient upshift.

We started by evaluating changes in cell dimensions and growth. Fig. 6.5A represents the sum of cells length, width and volume over time of one microcolony. Before the downshift, all three parameters increased at the same steady-state rate, which is similar to the upshift experiment. Upon nutrient shift,



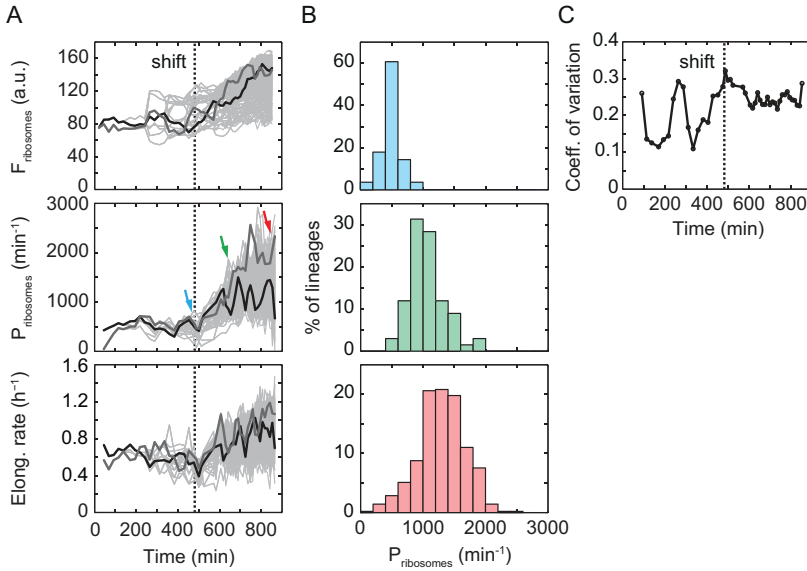


**Figure 6.3** Transient dynamics during upshift at the single-cell level. (A) Ribosome fluorescence (top), ribosome production rate (middle) and elongation rate (bottom) over time of all lineages within the microcolony. The two thick lines highlight two particular lineages. (B) Histogram of ribosome production rate a few minutes before the shift-up (top,  $N = 28$ ), during the transition period (middle,  $N = 67$ ) and at steady-state (bottom,  $N = 490$ ) as indicated by the colored arrows on (A). (C) Coefficient of variation of the ribosome production rate over time. Note that the first cell cycle is not taken into account here. The vertical line indicates the time of shift.

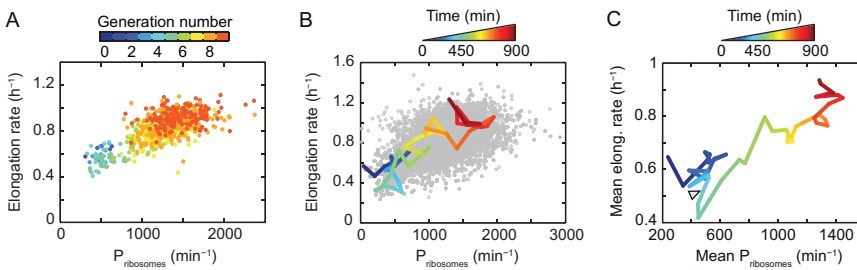


**Figure 6.4** Correlation between elongation rate and ribosome production rate. (A) In this scatter plot, one point represents one cell cycle. Note that only cells that finished their cell cycle are used here. Cells are colored according to their generation number. Here, the shift-up occurred during generation 4-5. (B) In this scatter plot, each point represents single elongation rate and ribosome production rate at one point in time. A particular trajectory, or lineage, is shown in color, where the color represents time. (C) Mean elongation rate versus mean ribosome production rate. As in (B), the color represents time. The arrow indicates the time of shift.

adaptation to the new rate proceeded with different delays. The rate of length increase was maintained at its pre-shift value for 15 min, and decreased slowly until steady-state was reached 120 min after the time of shift. The width and volume continued to increase at the pre-shift rate for about 50 and 20 min respectively, after which they both adjusted abruptly to the new rate. The delays observed here are 2 to 4 times shorter than those observed in nutrient upshifts. The rate of cell division, inferred by the number of cells over time (Fig. 6.5.B), remained approximately constant for about 40 min after the downshift. We observed this rate maintenance in nutrient upshifts (see Fig. 6.1B), and it has been shown in bulk as well [239].

The mean length and volume (Fig. 6.5B) showed the same saw-tooth patterns that we observed in upshifts. Here also we are interested in the trend on top of these oscillations. Upon downshift, both gradually decreased and leveled off. 120 min after downshift near equilibrium was reached. The mean width started to decrease slowly 40 min after downshift, but did not reach steady-state by the end of the experiment (Fig. 6.5B, green trace). The mean width effectively decreased from  $0.70\ \mu\text{m}$  to  $0.56\ \mu\text{m}$ , while the mean volume changed from  $0.76$  to  $0.37\ \mu\text{m}^3$ . Overall, these results are qualitatively similar to those obtained for the nutrient upshift, but inverted.

The mean elongation rate showed an immediate decrease upon nutrient downshift (Fig. 6.5C). This decrease continued gradually until a steady-state value was reached less than 200 min after downshift. Both the dimensional and growth adjustments were faster during downshift than during upshift. Adaptation to the new growth rate spanned 4 generations, or 5 hours, in the nutrient upshift while it spanned 2 generations, or 3 hours, in the nutrient downshift. The upshift gave rise to a 1.4-fold change in growth rate, compared to a 2.5-fold change in the downshift. As a result, the absolute values of mean width and volume were different between upshift and downshift, and although the change in width was comparable in both shifts, the change in volume was 1.5 larger in the downshift than in the upshift.

### 6.2.6 Transient dynamics of ribosomes synthesis during downshift

The mean ribosome production rate was approximately constant and high during the first phase of high growth (Fig. 6.6A, red trace), equal to  $1500\ \text{min}^{-1}$  on average, which is comparable to value measured at high growth rate during the upshift. Upon downshift, the production rate first decreased abruptly

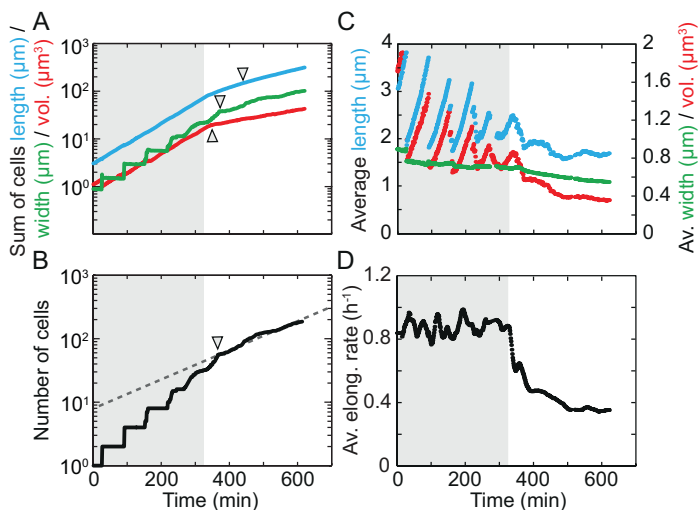


**Figure 6.5** Growth dynamics during downshift at the population level. (A) Sum of cells length (blue), width (green) and volume (red) over time of one microcolony. Note that the volume trace has been slightly shifted vertically for clarity. Arrows indicate the time of the new steady-state rate. (B) Number of cells of the microcolony over time. The dashed line is added to guide the eye. (C) Mean cell length (blue), width (green) and volume (red) over time of the microcolony. (D) Mean elongation rate of the microcolony over time.

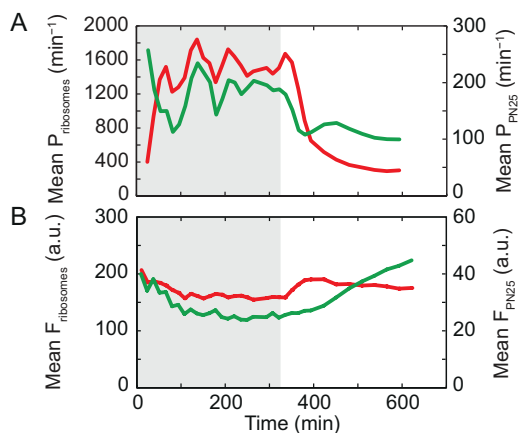


**Figure 6.6** Expression dynamics of ribosomes and of a constitutive gene during downshift. (A) Mean production rate of ribosomes (red) and  $P_{N25}$  (green) of the microcolony. (B) Mean fluorescence of ribosomes (red) and  $P_{N25}$  (green) of the microcolony.

by more than twofold with a delay of 20 min. Afterwards the rate continued to decrease but more slowly until steady-state was reached. The ribosome concentration immediately increased upon downshift, and then decreased to a value slightly higher than the pre-shift concentration (Fig. 6.6B, red trace). Both ribosome production rate and concentration adjusted to their new value within the same time of 200 min, which is faster than the 250 to 300 min measured in the nutrient upshift. The increase almost immediately after the shift indicates that the volume decreases faster than the number of ribosomes following glucose depletion. A study found that upon downshift in dilution rate (from 0.6 to 0.2 h<sup>-1</sup>), the ribosome concentration reached steady-state almost 8 hrs after the shift [238], which is considerably longer than what we observe in our experiments. This could be because of the larger change in growth rate in this study compared to our experiments.

The mean production rate of P<sub>N25</sub> decreased immediately upon downshift by half its pre-shift value, after which it fluctuated around its new rate (Fig. 6.6A, green trace). The mean fluorescence remained constant for 1 hr after the shift, and then increased significantly (Fig. 6.6B, green trace). At the end of the experiment, though the mean fluorescence had doubled compared to the pre-shift value, it was not at steady-state yet. The increase in concentration of constitutively expressed proteins is consistent with previous results [60].

### 6.2.7 Single-cell dynamics during downshift

As observed for the nutrient upshift experiment, the growth and ribosome production rate response to downshift seemed to be rather homogeneous for all cells in the microcolony. Fig. 6.7B represents the distributions of the ribosome production rate at three different time points: a few minutes before the shift (top), during the transition to the new steady-state (middle) and at the end of the experiment when the new steady-state rate was established (bottom). Here again all distributions had a similar bell-shape with no bimodality, suggesting the uniform response of single cells to the shift. We characterized the variability further by plotting the coefficient of variation of the ribosome production rate distributions over time (Fig. 6.7C). Before the shift, the coefficient of variation fluctuated around 0.2 and increased slightly after the shift, though a sharp increase up to 0.5 was observed the last hundred minutes of the experiment. This result suggests that a significant fraction of the population had a lower (or higher) production rate and growth rate than the mean.

### 6.2.8 Correlation between growth rate and ribosome production rate

The correlation that we saw between elongation rate and ribosome production rate in the nutrient upshift is conserved here too (Fig. 6.8A): overall, when the production rate decreases, the elongation rate decreases as well. At steady-state, the correlation between elongation rate and ribosome production rate is almost lost (for instance at generation 7,  $r^2 = 0.12$  and  $p\text{-value} = 0.007$ ). On Fig. 6.8B is also plotted the elongation rate versus ribosome production rate, with a particular lineage highlighted and colored according to time. The curve is seen to take a detour, with the growth rate decreasing first, followed by the production rate. This trend is also evident in the population mean curve (Fig. 6.8C). It also contrasts with the observations in the upshift experiments, where ribosome production rate and growth rate increased at the same time.

## 6.3 Conclusions and outlook

For the first time, we could accurately monitor simultaneously ribosome production rate and growth rate in single cells during nutrient shifts. Previous studies in bulk measured the number of cells over time, or the OD over time, from which the cell mass was inferred. However, OD measurements cannot properly distinguish between cell elongation and number increase. In addition, while these studies could measure the amount of RNA over time, this is not a direct measurement of ribosome production rate. The preliminary results shown here are not in conflict with previous data obtained with batch cultures or chemostats. Indeed, both in upshifts and downshifts, we observed the ‘rate maintenance’ phenomenon. In addition, the timescale of dimensional rearrangements is similar in our experiments and these studies.

Surprisingly, during nutrient upshift, it took the cells considerable amount of time to reach the new faster growth rate. It remains unclear what limits growth, and ribosome synthesis, when increasing the glucose concentration. Further investigations would thus be needed to propose a mechanism. It could be that because ribosomes are the rate-limiting step in their own synthesis, ribosome synthesis takes time to ramp up. However, that should also be the case in batch cultures where cells were shifted from poor to rich media. There, adaptation is comparatively faster, as RNA synthesis for instance adapted to the new rate immediately. Perhaps glucose uptake itself could be limiting. The main glucose

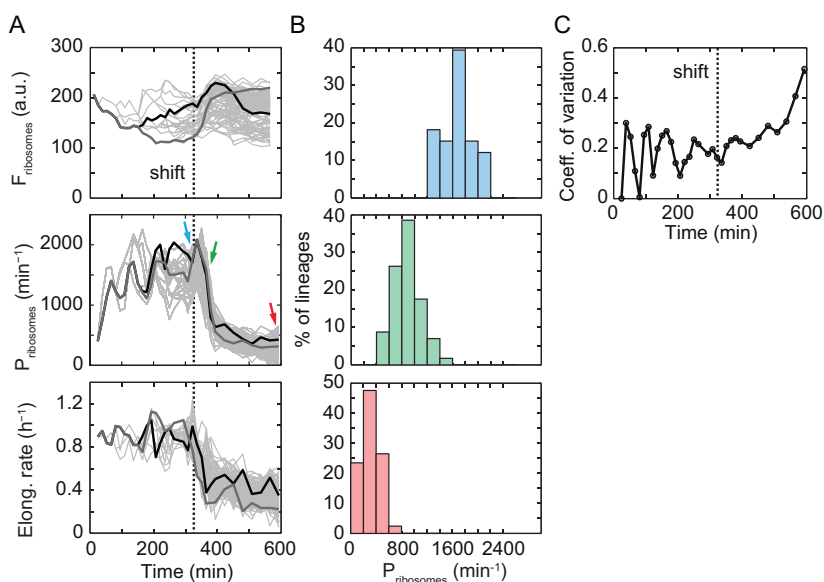


**Figure 6.7** Transient dynamics during downshift at the single-cell level. (A) Ribosome fluorescence (top), ribosome production rate (middle) and elongation rate (bottom) over time of all lineages within the microcolony. The two thick lines highlight two particular lineages. (B) Histogram of ribosome production rate a few minutes before the shift-up (top,  $N = 33$ ), during the transition period (middle,  $N = 57$ ) and at steady-state (bottom,  $N = 171$ ) as indicated by the colored arrows on (A). (C) Coefficient of variation of the ribosome production rate distributions over time. The vertical line indicates the time of shift.

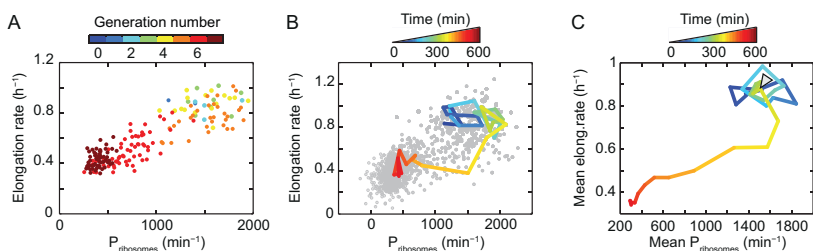


**Figure 6.8** Correlation between elongation rate and ribosome production rate. (A) In this scatter plot, one point represents one cell cycle. Note that only cells that finished their cell cycle are used here. Cells are colored according to their generation number. Here, the downshift occurred during generation 5. (B) In this scatter plot, each point represents single elongation rate and ribosome production rate at one point in time. A particular trajectory, or lineage, is shown in color, where the color represents time. For clarity, the first cell cycle is not plotted. (C) Mean elongation rate versus mean ribosome production rate. As in (B), the color represents time. The first cell cycle is not plotted. The arrow indicates the time of shift.

uptake system in *E. coli* under conditions of glucose excess is the PTS system. When glucose is limiting, the glucose-PTS system has been shown to remain the main uptake system (and thus the main contributor to growth) but is used together with the mannose-PTS and maltose and galactose high-affinity transporters [240]. Hence, monitoring not only ribosome synthesis but glucose assimilation could be of interest. We did not see an immediate response of the elongation rate upon upshift. Since all the enzymes were present and nutrient was limiting, a higher flux and faster cell wall growth could well have been possible. However, some internal adjustments seem required to grow faster. The measurements suggest that this could be ribosome adjustment, given the tight correlation between the growth rate and ribosome production rate, though other adjustments could also be causal.

The rather homogeneous timing of adaptation within single cells upon nutrient shift could also be worth further investigation, as it is also surprising since it could be expected that cells starting with different ribosome production rates and growth rates would adapt with different delays to nutrient shifts.

## 6.4 Materials and methods

### 6.4.1 Strain and media

Experiments were performed with the *E. coli* strain ASC659 ( $\Delta Che::HR-gfp + P_{N25}-Cam^R, L31-mCherry-Kan^R$ ) based on MG1655 (*rph-1 ilvG- rfb-50*). Cells were grown in M9 minimal medium supplemented with uracil (as described in Chapter 2) and the appropriate amount of glucose (Sigma). The microfluidic device used in the same as described in other chapters.

### 6.4.2 Microscopy and data analysis

Phase contrast images (300 ms exposure time with GIF filter) were taken every 70 sec; fluorescence images every 10 min at high growth, 20 min at low growth (50 or 150 ms exposure).

The total fluorescence of each cell and the protein production rate were determined as described in Chapter 2. The production rate obtained was smoothed with the Matlab 'smooth' function using the 'lowess' method and a

span of 4. The mean production rate of the microcolony is the mean of the production rate over all cells in the microcolony at each time point.

The cell volume  $v$  was calculated by assuming that the cell has the shape of a cylinder capped by two half-spheres. The resulting formula follows:

$$v = \frac{\pi \cdot w^2 \cdot \left( l - \frac{w}{3} \right)}{4}$$

where  $w$  is the cell's width and  $l$  the cell's length.

Fits to determine the mean cell width and volume were performed on a time window of 100 min before the shift, and the last 100 min of the experiment.



## Bibliography

1. Luria SE, Delbrück M (1943) Mutations of bacteria from virus sensitivity to virus resistance. *Genetics* 28: 491-511.
2. Avery OT, MacLeod CM, McCarty M (1944) Studies on the chemical nature of the substance inducing transformation of Pneumococcal types: induction of transformation by a desoxyribonucleic acid fraction isolated from Pneumococcus Type III. *The Journal of Experimental Medicine* 79: 137-158.
3. Watson JD, Crick FHC (1953) Genetical implications of the structure of deoxyribonucleic acid. *Nature* 171: 964-967.
4. Watson JD, Crick FHC (1953) Molecular structure of nucleic acids. A structure for deoxyribose nucleic acid. *Nature* 171: 737-738.
5. Jacob F, Monod J (1961) Genetic regulatory mechanisms in the synthesis of proteins. *J Mol Biol* 3: 318-356.
6. Stent GS (1968) That was the molecular biology that was. *Science* 160: 390- 395.
7. Bruggeman FJ, Westerhoff HV (2007) The nature of systems biology. *Trends Microbiol* 15: 45-50.
8. Garfinkel D, Garfinkel L, Pring M, Green SB, Chance B (1970) Computer applications to biochemical kinetics. *Annu Rev Biochem* 39: 473-498.
9. Heinrich R, Rapoport SM, Rapoport TA (1977) Metabolic regulation and mathematical models. *Prog Biophys Mol Biol* 32: 1-82.
10. Metzker ML (2010) Sequencing technologies - the next generation. *Nat Rev Genet* 11: 31-46.
11. Schena M, et al. (1998) Microarrays: biotechnology's discovery platform for functional genomics. *Trends Biotechnol* 16: 301-306.
12. Reaves ML, Rabinowitz JD (2011) Metabolomics in systems microbiology. *Curr Opin Biotechnol* 22: 17-25.
13. Angel TE, et al. (2012) Mass spectrometry-based proteomics: existing capabilities and future directions. *Chem Soc Rev* 41: 3912-3928.
14. Baker MD, Wolanin PM, Stock JB (2006) Systems biology of bacterial chemotaxis. *Curr Opin Microbiol* 9: 187-192.
15. Kollmann M, Løvdok L, Bartholomé K, Timmer J, Sourjik V (2005) Design principles of a bacterial signalling network. *Nature* 438: 504-507.
16. Alon U (2007) Network motifs: theory and experimental approaches.

- Nat Rev Genet* 8: 450-461.
17. Zeng L, *et al.* (2010) Decision making at a subcellular level determines the outcome of bacteriophage infection. *Cell* 141: 682-691.
  18. Kuchina A, *et al.* (2011) Temporal competition between differentiation programs determines cell fate choice. *Mol Syst Biol* 7: 755.
  19. Veening JW, *et al.* (2008) Bet-hedging and epigenetic inheritance in bacterial cell development. *Proc Natl Acad Sci U S A* 105: 4393-4398.
  20. Raser JM, O'Shea EK (2005) Noise in gene expression: origins, consequences, and control. *Science* 309: 2010-2013.
  21. Balázsi G, van Oudenaarden A, Collins JJ (2011) Cellular decision making and biological noise: from microbes to mammals. *Cell* 144: 910-925.
  22. Maheshri N, O'Shea EK (2007) Living with noisy genes: how cells function reliably with inherent variability in gene expression. *Annu Rev Biophys Biomol Struct* 36: 413-434.
  23. Davidson CJ, Surette MG (2008) Individuality in bacteria. *Annu Rev Genet* 42: 253-268.
  24. Laub MT, McAdams HH, Feldblyum T, Fraser CM, Shapiro L (2000) Global analysis of the genetic network controlling a bacterial cell cycle. *Science* 290: 2144-2148.
  25. Cookson NA, Cookson SW, Tsimring LS, Hasty J (2010) Cell cycle-dependent variations in protein concentration. *Nucleic Acids Res* 38: 2676-2681.
  26. Huh D, Paulsson J (2011) Non-genetic heterogeneity from stochastic partitioning at cell division. *Nat Genet* 43: 95-100.
  27. Barker MG, Walmsley RM (1999) Replicative ageing in the fission yeast *Schizosaccharomyces pombe*. *Yeast* 15: 1511-1518.
  28. Kaufmann BB, Yang Q, Mettetal JT, van Oudenaarden A (2007) Heritable stochastic switching revealed by single-cell genealogy. *PLoS Biol* 5: e239.
  29. Choi PJ, Cai L, Frieda K, Xie XS (2008) A stochastic single-molecule event triggers phenotype switching of a bacterial cell. *Science* 322: 442-446.
  30. Robert L, *et al.* (2010) Pre-dispositions and epigenetic inheritance in the *Escherichia coli* lactose operon bistable switch. *Mol Syst Biol* 6: 357.
  31. Bigger JW (1944) Treatment of staphylococcal infections with penicillin by intermittent sterilization. *Lancet* 2: 497-500.
  32. Novick A, Weiner M (1957) Enzyme induction as an all-or-none

- phenomenon. *Proc Natl Acad Sci U S A* 43: 553-566.
33. Cox J, Mann M (2011) Quantitative, high-resolution proteomics for data-driven systems biology. *Annu Rev Biochem* 80: 273-299.
  34. Gagarinova A, Emili A (2012) Genome-scale genetic manipulation methods for exploring bacterial molecular biology. *Mol Biosyst* 8: 1626-1638.
  35. Wang D, Bodovitz S (2010) Single cell analysis: the new frontier in 'omics'. *Trends Biotechnol* 28: 281-290.
  36. Locke JC, Elowitz MB (2009) Using movies to analyse gene circuit dynamics in single cells. *Nat Rev Microbiol* 7: 383-392.
  37. Süel GM, Garcia-Ojalvo J, Liberman LM, Elowitz MB (2006) An excitable gene regulatory circuit induces transient cellular differentiation. *Nature* 440: 545- 550.
  38. Süel GM, Kulkarni MP, Dworkin J, Garcia-Ojalvo J, Elowitz MB (2007) Tunability and noise dependence in differentiation dynamics. *Science* 315: 1716-1719.
  39. Eldar A, Elowitz MB (2010) Functional roles for noise in genetic circuits. *Nature* 467: 167-173.
  40. Elowitz MB, Levine AJ, Siggia ED, Swain PS (2002) Stochastic gene expression in a single cell. *Science* 297: 1183-1186.
  41. Balaban NQ, Merrin J, Chait R, Kowalik L, Leibler S (2004) Bacterial persistence as a phenotypic switch. *Science* 305: 1622-1625.
  42. Levine AJ, Puzio-Kuter AM (2010) The control of the metabolic switch in cancers by oncogenes and tumor suppressor genes. *Science* 330: 1340-1344.
  43. Arkin A, Ross J, McAdams HH (1998) Stochastic kinetic analysis of developmental pathway bifurcation in phage  $\lambda$ -infected *Escherichia coli* cells. *Genetics* 149: 1633-1648.
  44. Raj A, van Oudenaarden A (2008) Nature, nurture, or chance: stochastic gene expression and its consequences. *Cell* 135: 216-226.
  45. Paulsson J (2004) Summing up the noise in gene networks. *Nature* 427: 415- 418.
  46. Ozbudak EM, Thattai M, Kurtser I, Grossman AD, van Oudenaarden A (2002) Regulation of noise in the expression of a single gene. *Nat Genet* 31: 69-73.
  47. Thattai M, van Oudenaarden A (2001) Intrinsic noise in gene regulatory networks. *Proc Natl Acad Sci U S A* 98: 8614-8619.
  48. Cai L, Friedman N, Xie XS (2006) Stochastic protein expression in individual cells at the single molecule level. *Nature* 440: 358-362.

49. Yu J, Xiao J, Ren X, Lao K, Xie XS (2006) Probing gene expression in live cells, one protein molecule at a time. *Science* 311: 1600-1603.
50. Golding I, Paulsson J, Zawilski SM, Cox EC (2005) Real-time kinetics of gene activity in individual bacteria. *Cell* 123: 1025-1036.
51. Gandhi SJ, Zenklusen D, Lionnet T, Singer RH (2011) Transcription of functionally related constitutive genes is not coordinated. *Nat Struct Mol Biol* 18: 27-34.
52. So LH, *et al.* (2011) General properties of transcriptional time series in *Escherichia coli*. *Nat Genet* 43: 554-560.
53. Raj A, Peskin CS, Tranchina D, Vargas DY, S. T (2006) Stochastic mRNA synthesis in mammalian cells. *PLoS Biol* 4: e309.
54. Rosenfeld N, Young JW, Alon U, Swain PS, Elowitz MB (2005) Gene regulation at the single-cell level. *Science* 307: 1962-1965.
55. Pedraza JM, van Oudenaarden A (2005) Noise propagation in gene networks. *Science* 307: 1965-1969.
56. Dunlop MJ, Cox RS, Levine JH, Murray RM, Elowitz MB (2008) Regulatory activity revealed by dynamic correlations in gene expression noise. *Nat Genet* 40: 1493-1498.
57. Munsky B, Neuert G, van Oudenaarden A (2012) Using gene expression noise to understand gene regulation. *Science* 336: 183-187.
58. Brauer MJ, *et al.* (2008) Coordination of growth rate, cell cycle, stress response, and metabolic activity in yeast. *Mol Biol Cell* 19: 352-367.
59. Pedersen S, Bloch PL, Reeh S, Neidhardt FC (1978) Patterns of protein synthesis in *E. coli*: a catalog of the amount of 140 individual proteins at different growth rates. *Cell* 14: 179-190.
60. Klumpp S, Zhang Z, Hwa T (2009) Growth rate-dependent global effects on gene expression in bacteria. *Cell* 139: 1366-1375.
61. Guido NJ, *et al.* (2006) A bottom-up approach to gene regulation. *Nature* 439: 856-860.
62. Baumgartner BL, *et al.* (2011) Antagonistic gene transcripts regulate adaptation to new growth environments. *Proc Natl Acad Sci U S A* 108: 21087-21092.
63. Youk H, van Oudenaarden A (2009) Growth landscape formed by perception and import of glucose in yeast. *Nature* 462: 875-880.
64. Airoidi EM, *et al.* (2009) Predicting cellular growth from gene expression signatures. *PLoS Comput Biol* 5: e1000257.
65. Tan C, Marguet P, You L (2009) Emergent bistability by a growth-modulating positive feedback circuit. *Nat Chem Biol* 5: 842-848.
66. Zaslaver A, *et al.* (2009) Invariant distribution of promoter activities in

- Escherichia coli*. *PLoS Comput Biol* 5: e1000545.
67. Scott M, Gunderson CW, Mateescu EM, Zhang Z, Hwa T (2010) Interdependence of cell growth and gene expression: origins and consequences. *Science* 330: 1099-1102.
  68. Kjeldgaard NO, Maaloe O, Schaechter M (1958) The transition between different physiological states during balanced growth of *Salmonella typhimurium*. *J Gen Microbiol* 19: 607-616.
  69. Winslow RM (1971) A consequence of the *rel* gene during a glucose to lactate downshift in *Escherichia coli*. *J Biol Chem* 246: 4872-4877.
  70. Kubitschek HE (1990) Cell volume increase in *Escherichia coli* after shifts to richer media. *J Bacteriol* 172: 94-101.
  71. Brunschede H, Dove TL, Bremer H (1977) Establishment of exponential growth after a nutritional shift-up in *Escherichia coli* B/r: accumulation of deoxyribonucleic acid, ribonucleic acid, and protein. *J Bacteriol* 129: 1020- 1033.
  72. Sloan JB, Urban JE (1976) Growth response of *Escherichia coli* to nutritional shift-up: immediate division stimulation in slow-growing cells. *J Bacteriol* 128: 302-308.
  73. Nazar RN, Tze-Fei Wong J (1969) Inhibitor-induced shift-downs in *Escherichia coli*. *J Bacteriol* 100: 956-961.
  74. Weibel DB, Diluzio WR, Whitesides GM (2007) Microfabrication meets microbiology. *Nat Rev Microbiol* 5: 209-218.
  75. El-Ali J, Sorger PK, Jensen KF (2006) Cells on chips. *Nature* 442: 403-411.
  76. Khademhosseini A, Langer R, Borenstein J, Vacanti JP (2006) Microscale technologies for tissue engineering and biology. *Proc Natl Acad Sci U S A* 103: 2480-2487.
  77. Walker GM, Zeringue HC, Beebe DJ (2004) Microenvironment design considerations for cellular scale studies. *Lab Chip* 4: 91-97.
  78. Breslauer DN, Lee PJ, Lee LP (2006) Microfluidics-based systems biology. *Mol Biosyst* 2: 97-112.
  79. Whitesides GM (2006) The origins and the future of microfluidics. *Nature* 442: 368-373.
  80. Balagaddé FK, You L, Hansen CL, Arnold FH, Quake SR (2005) Long-term monitoring of bacteria undergoing programmed population control in a microchemostat. *Science* 309: 137-140.
  81. Groisman A, *et al.* (2005) A microfluidic chemostat for experiments with bacterial and yeast cells. *Nat Methods* 2: 685-689.
  82. Leclerc E, Sakai Y, Fujii T (2003) Cell culture in 3-Dimensional

- microfluidic structure of PDMS (polydimethylsiloxane). *Biomed Microdevices* 5: 109-114.
83. Walters EM, Clark SG, Beebe DJ, Wheeler MB (2004) Mammalian embryo culture in a microfluidic device. *Methods Mol Biol* 254: 375-382.
  84. Ben-Yakar A, Chronis N, Lu H (2009) Microfluidics for the analysis of behavior, nerve regeneration, and neural cell biology in *C. elegans*. *Curr Opin Neurobiol* 19: 561-567.
  85. Hung PJ, Lee PJ, Sabounchi P, Lin R, Lee LP (2005) Continuous perfusion microfluidic cell culture array for high-throughput cell-based assays. *Biotechnol Bioeng* 89: 1-8.
  86. Bennett MR, *et al.* (2008) Metabolic gene regulation in a dynamically changing environment. *Nature* 454: 1119-1122.
  87. Sia SK, Whitesides GM (2003) Microfluidic devices fabricated in poly(dimethylsiloxane) for biological studies. *Electrophoresis* 24: 3563-3576.
  88. McDonald JC, Whitesides GM (2002) Poly(dimethylsiloxane) as a material for fabricating microfluidic devices. *Acc Chem Res* 35: 491-499.
  89. Lee JN, Jiang X, Ryan D, Whitesides GM (2004) Compatibility of mammalian cells on surfaces of poly(dimethylsiloxane). *Langmuir* 20: 11684-11691.
  90. Danino T, Hasty J, Tsimring LS, Mather W, Mondrago O (2010) Streaming instability in growing cell populations. *Phys Rev Lett* 208101: 1-4.
  91. Cho H, *et al.* (2007) Self-organization in high-density bacterial colonies: efficient crowd control. *PLoS Biol* 5: e302.
  92. Regehr KJ, *et al.* (2009) Biological implications of polydimethylsiloxane-based microfluidic cell culture. *Lab Chip* 9: 2132-2139.
  93. Engler AJ, Sen S, Sweeney HL, Discher DE (2006) Matrix elasticity directs stem cell lineage specification. *Cell* 126: 677-689.
  94. Driessen R, Galajda P, Keymer JE, Dekker C (2009) Bacterial growth and motility in sub-micron constrictions. *Proc Natl Acad Sci U S A* 106: 14861-14866.
  95. Drury JL, Mooney DJ (2003) Hydrogels for tissue engineering: scaffold design variables and applications. *Biomaterials* 24: 4337-4351.
  96. Choi NW, *et al.* (2007) Microfluidic scaffolds for tissue engineering. *Nat Mater* 6: 908-915.

97. Elowitz MB, Leibler S (2000) A synthetic oscillatory network of transcriptional regulators. *Nature* 403: 335-338.
98. Tran PT, Paoletti A, Chang F (2004) Imaging green fluorescent protein fusions in living fission yeast cells. *Methods* 33: 220-225.
99. Sulston JE, Horvitz HR (1977) Post-embryonic cell lineages of the nematode, *Caenorhabditis elegans*. *Dev Biol* 56: 110-156.
100. Podbilewicz B, Gruenbaum Y (2006) Live Imaging of *Caenorhabditis elegans*: preparation of samples. *CSH Protoc* 2006: pii: pdb.prot4601.
101. Ducret A, *et al.* (2009) A microscope automated fluidic system to study bacterial processes in real time. *PLoS One* 4: e7282.
102. Wong I, *et al.* (2010) An agar gel membrane-PDMS hybrid microfluidic device for long term single cell dynamic study. *Lab Chip* 10: 2710-2719.
103. Takeuchi S, DiLuzio WR, Weibel DB, Whitesides GM (2005) Controlling the shape of filamentous cells of *Escherichia coli*. *Nano Lett* 5: 1819-1823.
104. Moffitt JR, Lee JB, Cluzel P (2012) The single-cell chemostat: an agarose-based, microfluidic device for high-throughput, single-cell studies of bacteria and bacterial communities. *Lab Chip* 12: 1487-1494.
105. Bringmann H (2011) Agarose hydrogel microcompartments for imaging sleep- and wake-like behavior and nervous system development in *Caenorhabditis elegans* larvae. *J Neurosci Methods* 201: 78-88.
106. Ahmed T, Shimizu TS, Stocker R (2010) Bacterial chemotaxis in linear and nonlinear steady microfluidic gradients. *Nano Lett* 10: 3379-3385.
107. Chi WJ, Chang YK, Hong SK (2012) Agar degradation by microorganisms and agar-degrading enzymes. *Appl Microbiol Biotechnol* 94: 917-930.
108. Pelham RJ, Jr., Wang YI (1997) Cell locomotion and focal adhesions are regulated by substrate flexibility. *Proc Natl Acad Sci U S A* 94: 13661-13665.
109. Tse JR, Engler AJ (2010) Preparation of hydrogel substrates with tunable mechanical properties. *Curr Protoc Cell Biol* Chapter 10:Unit 10.
110. Tanaka Y, Fukao K, Miyamoto Y (2000) Fracture energy of gels. *Eur J Phys E* 3: 395-401.
111. Bonn D, Kellay H, Prochnow M, Ben-Djemaa K, Meunier J (1998) Delayed fracture of an inhomogeneous soft solid. *Science* 280: 265-267.
112. Kwon HJ, Rogalsky AD, Kim DW (2011) On the measurement of fracture toughness of soft biogel. *Polym Eng Sci* 51: 1078-1086.
113. Isenberg BC, Dimilla PA, Walker M, Kim S, Wong JY (2009) Vascular smooth muscle cell durotaxis depends on substrate stiffness gradient



- strength. *Biophys J* 97: 1313-1322.
114. Mih JD, *et al.* (2011) A multiwell platform for studying stiffness-dependent cell biology. *PLoS One* 6: e19929.
  115. Zaari N, Rajagopalan P, Kim SK, Engler AJ, Wong JY (2004) Photopolymerization in microfluidic gradient generators: microscale control of substrate compliance to manipulate cell response. *Adv Mater* 16: 2133- 2137.
  116. Liu J, Yang S, Lee CS, DeVoe DL (2008) Polyacrylamide gel plugs enabling 2-D microfluidic protein separations via isoelectric focusing and multiplexed sodium dodecyl sulfate gel electrophoresis. *Electrophoresis* 29: 2241-2250.
  117. Brahmasandra SN, Ugaz VM, Burke DT, Mastroangelo CH, Burns MA (2001) Electrophoresis in microfabricated devices using photopolymerized polyacrylamide gels and electrode-defined sample injection. *Electrophoresis* 22: 300-311.
  118. Charvin G, Cross FR, Siggia ED (2008) A microfluidic device for temporally controlled gene expression and long-term fluorescent imaging in unperturbed dividing yeast cells. *PLoS One* 3: e1468.
  119. Cheng SY, *et al.* (2007) A hydrogel-based microfluidic device for the studies of directed cell migration. *Lab Chip* 7: 763-769.
  120. Andersen KB, von Meyenburg K (1980) Are growth rates of *Escherichia coli* in batch cultures limited by respiration? *J Bacteriol* 144: 114-123.
  121. Austin DW, *et al.* (2006) Gene network shaping of inherent noise spectra. *Nature* 439: 608-611.
  122. Piel M, Tran PT (2009) Cell shape and cell division in fission yeast. *Curr Biol* 19: R823-R827.
  123. Höög JL, *et al.* (2011) Electron tomography reveals a flared morphology on growing microtubule ends. *J Cell Sci* 124: 693-698.
  124. Leifer AM, Fang-Yen C, Gershow M, Alkema MJ, Samuel AD (2011) Optogenetic manipulation of neural activity in freely moving *Caenorhabditis elegans*. *Nat Methods* 8: 147-152.
  125. Cormack BP, Valdivia RH, Falkow S (1996) FACS-optimized mutants of the green fluorescent protein (GFP). *Gene* 173: 33-38.
  126. Datsenko KA, Wanner BL (2000) One-step inactivation of chromosomal genes in *Escherichia coli* K-12 using PCR products. *Proc Natl Acad Sci U S A* 97: 6640-6645.
  127. Jensen KF (1993) The *Escherichia coli* K-12 “Wild Types” W3110 and MG1655 have an *rph* frameshift mutation that leads to pyrimidine starvation due to low *pyrE* expression levels. *J Bacteriol* 175: 3401-3407.



128. Beg QK, *et al.* (2007) Intracellular crowding defines the mode and sequence of substrate uptake by *Escherichia coli* and constrains its metabolic activity. *Proc Natl Acad Sci U S A* 104: 12663-12668.
129. Brenner S (1974) The genetics of *Caenorhabditis elegans*. *Genetics* 77: 71-94.
130. Crank J (1956) The mathematics of diffusion (Oxford University Press).
131. Young JW, *et al.* (2011) Measuring single-cell gene expression dynamics in bacteria using fluorescence time-lapse microscopy. *Nat Protoc* 7: 80-88.
132. Itan E, Carmon G, Rabinovitch A, Fishov I, Feingold M (2008) Shape of nonseptated *Escherichia coli* is asymmetric. *Phys Rev E Stat Nonlin Soft Matter Phys* 77: 061902.
133. Monod J (1949) The growth of bacterial cultures. *Annu Rev Microbiol* 3: 371-394.
134. Loomis WF, Magasanik B (1967) Glucose-lactose diauxie in *Escherichia coli*. *J Bacteriol* 93: 1397-1401.
135. Magasanik B (1961) Catabolite repression. *Cold Spring Harb Symp Quant Biol* 26: 249-256.
136. Molin S, von Meyenburg K, Maaloe O, Hansen MT, Pato ML (1977) Control of ribosome synthesis in *Escherichia coli*: analysis of an energy source shift-down. *J Bacteriol* 131: 7-17.
137. Johnsen K, Molin S, Karlstrom O, Maaloe O (1977) Control of protein synthesis in *Escherichia coli*: analysis of an energy source shift-down. *J Bacteriol* 131: 18-29.
138. Marr AG (1991) Growth rate of *Escherichia coli*. *Microbiol Rev* 55: 316-333.
139. de Jong IG, Haccou P, Kuipers OP (2011) Bet hedging or not? A guide to proper classification of microbial survival strategies. *Bioessays* 33: 215-223.
140. Dekel E, Alon U (2005) Optimality and evolutionary tuning of the expression level of a protein. *Nature* 436: 588-592.
141. Longo D, Hasty J (2006) Dynamics of single-cell gene expression. *Mol Syst Biol* 2:64.
142. Bennett MR, Hasty J (2009) Microfluidic devices for measuring gene network dynamics in single cells. *Nat Rev Genet* 10: 628-638.
143. Ozbudak EM, Thattai M, Lim HN, Shraiman BI, Van Oudenaarden A (2004) Multistability in the lactose utilization network of *Escherichia coli*. *Nature* 427: 737-740.
144. Novick A, Weiner M (1957) Enzyme induction as an all-or-non

- phenomenon. *Proc Natl Acad Sci U S A* 43: 553-566.
145. Shehata TE, Marr AG (1971) Effect of nutrient concentration on the growth of *Escherichia coli*. *J Bacteriol* 107: 210-216.
  146. van Hoek MJA, Hogeweg P (2006) In silico evolved *lac* operons exhibit bistability for artificial inducers, but not for lactose. *Biophys J* 91: 2833-2843.
  147. Dreisigmeyer DW, Stajic J, Nemenman I, Hlavacek WS, Wall WE (2008) Determinants of bistability in induction of the *Escherichia coli lac* operon. *IET Syst Biol* 2: 293-303.
  148. Zaslaver A, et al. (2006) A comprehensive library of fluorescent transcriptional reporters for *Escherichia coli*. *Nat Methods* 3: 623-628.
  149. Megerle JA, Fritz G, Gerland U, Kirsten J, Radler JO (2008) Timing and dynamics of single cell gene expression in the arabinose utilization system. *Biophys J* 95: 2103-2115.
  150. Wong P, Gladney S, Keasling JD (1997) Mathematical model of the *lac* operon: inducer exclusion, catabolite repression, and diauxic growth on glucose and lactose. *Biotechnol Prog* 13: 132-143.
  151. Covert MW, Schilling CH, Palsson B (2001) Regulation of gene expression in flux balance models of metabolism. *J Theor Biol* 213: 73-88.
  152. Kremling A, et al. (2001) The organization of metabolic reaction networks. III. Application for diauxic growth on glucose and lactose. *Metab Eng* 3: 362-379.
  153. Mahadevan R, Edwards J, Doyle F (2002) Dynamic flux balance analysis of diauxic growth in *Escherichia coli*. *Biophys J* 83: 1331-1340.
  154. Kotte O, Zaugg JB, Heinemann M (2010) Bacterial adaptation through distributed sensing of metabolic fluxes. *Mol Syst Biol* 6:355.
  155. Hermesen R, Erickson DW, Hwa T (2011) Speed, sensitivity, and bistability in auto-activating signaling circuits. *PLoS Comput Biol* 7: e1002265.
  156. Acar M, Mettetal JT, van Oudenaarden A (2008) Stochastic switching as a survival strategy in fluctuating environments. *Nat Genet* 40: 471-475.
  157. Tănase-Nicola S, ten Wolde PR (2008) Regulatory control and the costs and benefits of biochemical noise. *PLoS Comput Biol* 4: e1000125.
  158. Kalisky T, Dekel E, Alon U (2007) Cost-benefit theory and optimal design of gene regulation functions. *Phys Biol* 4: 229-245.
  159. Kartal O, Mahlow S, Skupin A, Ebenhöf O (2011) Carbohydrate-active enzymes exemplify entropic principles in metabolism. *Mol Syst Biol* 7:542.

160. Fischer D, Teich A, Neubauer P, Hengge-Aronis R (1998) The general stress sigma factor  $\sigma^S$  of *Escherichia coli* is induced during diauxic shift from glucose to lactose. *J Bacteriol* 180: 6203-6206.
161. Chang DE, Smalley DJ, Conway T (2002) Gene expression profiling of *Escherichia coli* growth transitions: an expanded stringent response model. *Mol Microbiol* 45: 289-306.
162. Kussell E, Leibler S (2005) Phenotypic diversity, population growth, and information in fluctuating environments. *Science* 309: 2075-2078.
163. Yildirim N, Mackey MC (2003) Feedback regulation in the lactose operon: a mathematical modeling study and comparison with experimental data. *Biophys J* 84: 2841-2851.
164. Santillán M, Mackey MC (2004) Influence of catabolite repression and inducer exclusion on the bistable behavior of the *lac* operon. *Biophys J* 86: 1282-1292.
165. Oehler S, Eismann ER, Krämer H, Müller-Hill B (1990) The three operators of the *lac* operon cooperate in repression. *EMBO J* 9: 973-979.
166. Kennell D, Riezman H (1977) Transcription and translation initiation frequencies of the *Escherichia coli lac* operon. *J Mol Biol* 114: 1-21.
167. Elf J, Li GW, Xie XS (2007) Probing transcription factor dynamics at the single-molecule level in a living cell. *Science* 316: 1191-1194.
168. Gilbert W, Müller-Hill B (1966) Isolation of the *lac* repressor. *Proc Natl Acad Sci U S A* 56: 1891-1898.
169. Barkley MD, Riggs AD, Jobe A, Bourgeois S (1975) Interaction of effecting ligands with *lac* repressor and repressor-operator complex. *Biochemistry* 14: 1700-1712.
170. Yagil G, Yagil E (1971) On the relation between effector concentration and the rate of induced enzyme synthesis. *Biophys J* 11: 11-27.
171. Dunaway M, *et al.* (1980) Kinetic studies of inducer binding to *lac* repressor-operator complex. *J Biol Chem* 255: 10115-10119.
172. Wright JK, Riede I, Overath P (1981) Lactose carrier protein of *Escherichia coli*: interaction with galactosides and protons. *Biochemistry* 20: 6404-6415.
173. Lolkema JS, Carrasco N, Kaback HR (1991) Kinetic analysis of lactose exchange in proteoliposomes reconstituted with purified *lac* permease. *Biochemistry* 30: 1284-1290.
174. Martinez-Bilbao M, Holdsworth RE, Edwards LA, Huber RE (1991) A highly reactive beta-galactosidase (*Escherichia coli*) resulting from a substitution of an aspartic acid for Gly-794. *J Biol Chem* 266: 4979-4986.

175. Cullum J, Vicente M (1978) Cell growth and length distribution in *Escherichia coli*. *J Bacteriol* 134: 330-337.
176. Reshes G, Vanounou S, Fishov I, Feingold M (2008) Cell shape dynamics in *Escherichia coli*. *Biophys J* 94: 251-264.
177. Schaechter M, Williamson JP, Hood JR, Koch AL (1962) Growth, cell and nuclear divisions in some bacteria. *J Gen Microbiol* 29: 421-434.
178. Godin M, *et al.* (2010) Using buoyant mass to measure the growth of single cells. *Nat Methods* 7: 387-390.
179. Mir M, *et al.* (2011) Optical measurement of cycle-dependent cell growth. *Proc Natl Acad Sci U S A* 108: 13124-13129.
180. Koch AL (1993) Biomass growth rate during the prokaryote cell cycle. *Crit Rev Microbiol* 19: 17-42.
181. Cooper S (2006) Distinguishing between linear and exponential cell growth during the division cycle: single-cell studies, cell-culture studies, and the object of cell-cycle research. *Theor Biol Med Model* 23: 3-10.
182. Chien AC, Hill NS, Levin PA (2012) Cell size control in bacteria. *Curr Biol* 22: R340-R349.
183. Kohanski MA, Dwyer DJ, Collins JJ (2010) How antibiotics kill bacteria: from targets to networks. *Nat Rev Micro* 8: 423-435.
184. Wilson DN (2009) The A–Z of bacterial translation inhibitors. *Crit Rev Biochem Mol Biol* 44: 393–433.
185. Chopra I, Roberts M (2001) Tetracycline antibiotics: mode of action, applications, molecular biology, and epidemiology of bacterial resistance. *Microbiol Mol Biol Rev* 65: 232-260.
186. Pulvertaft RJV (1952) The effect of antibiotics on growing cultures of *Bacterium coli*. *J Pathol* 64: 75-89.
187. VanBogelen RA, Neidhardt FC (1990) Ribosomes as sensors of heat and cold shock in *Escherichia coli*. *Proc Natl Acad Sci U S A* 87: 5589-5593.
188. Goh EB, *et al.* (2002) Transcriptional modulation of bacterial gene expression by subinhibitory concentrations of antibiotics. *Proc Natl Acad Sci U S A* 99: 17025–17030.
189. Sabina J, *et al.* (2003) Interfering with different steps of protein synthesis explored by transcriptional profiling of *Escherichia coli* K-12. *J Bacteriol* 185: 6158–6170.
190. Harvery RJ, Koch AL (1980) How partially inhibitory concentrations of chloramphenicol affect the growth of *Escherichia coli*. *Antimicrob Agents Chemother* 18: 323-337.
191. Shen V, Bremer H (1977) Chloramphenicol-induced changes in the synthesis of ribosomal, transfer, and messenger ribonucleic acids in

- Escherichia coli* B/r. *J Bacteriol* 130: 1098–1108.
192. Midgley JE, Gray WJ (1971) The control of ribocleic acid synthesis in bacteria. The synthesis and stability of ribonucleic acid in chloramphenicol-inhibited cultures of *Escherichia coli*. *Biochem J* 122: 149-159.
  193. Siibak T, *et al.* (2009) Erythromycin- and chloramphenicol-induced ribosomal assembly defects are secondary effects of protein synthesis inhibition. *Antimicrob Agents Chemother* 53: 563-571.
  194. Dodd J, Kolb JM, Nomura M (1991) Lack of complete cooperativity of ribosome assembly in vitro and its possible relevance to in vivo ribosome assembly and the regulation of ribosomal gene expression. *Biochimie* 73: 757-767.
  195. Knaus R, Bujard H (1988) PL of coliphage lambda: an alternative solution for an efficient promoter. *EMBO J* 7: 2919-2923.
  196. McAdams HH, Arkin A (1997) Stochastic mechanisms in gene expression. *Proc Natl Acad Sci U S A* 94: 814-819.
  197. Wilkinson DJ (2009) Stochastic modelling for quantitative description of heterogeneous biological systems. *Nat Rev Genet* 10: 122-133.
  198. Brock A, Chang H, Huang S (2009) Non-genetic heterogeneity--a mutation-independent driving force for the somatic evolution of tumours. *Nat Rev Genet* 10: 336-342.
  199. Kitano H (2004) Biological robustness. *Nat Rev Genet* 5: 826-837.
  200. Vander Heiden MG, Cantley LC, Thompson CB (2009) Understanding the Warburg effect: the metabolic requirements of cell proliferation. *Science* 324: 1029-1033.
  201. Lu HP, Xun L, Xie XS (1998) Single-molecule enzymatic dynamics. *Science* 282: 1877-1882.
  202. Fell D (1997) Understanding the control of metabolism (Portland, London).
  203. Herrgård MJ, Covert MW, Palsson BØ (2004) Reconstruction of microbial transcriptional regulatory networks. *Curr Opin Biotechnol* 15: 70-77. 204.
  204. Ferguson ML, *et al.* (2012) Reconciling molecular regulatory mechanisms with noise patterns of bacterial metabolic promoters in induced and repressed states. *Proc Natl Acad Sci U S A* 109: 155-160.
  205. Neidhardt FC, Ingraham JL, Schaechter M (1990) Physiology of the bacterial cell : a molecular approach (Sinauer Associates, Sunderland, Mass.).

206. Rodríguez M, Good TA, Wales ME, Hua JP, Wild JR (2005) Modeling allosteric regulation of *de novo* pyrimidine biosynthesis in *Escherichia coli*. *J Theor Biol* 234: 299-310.
207. Hart Y, et al. (2011) Robust control of nitrogen assimilation by a bifunctional enzyme in *E. coli*. *Mol Cell* 41: 117-127.
208. el-Mansi EM, Holms WH (1989) Control of carbon flux to acetate excretion during growth of *Escherichia coli* in batch and continuous cultures. *J Gen Microbiol* 135: 2875-2883.
209. Wilson WA, et al. (2010) Regulation of glycogen metabolism in yeast and bacteria. *FEMS Microbiol Rev* 34: 952-985.
210. Levine E, Hwa T (2007) Stochastic fluctuations in metabolic pathways. *Proc Natl Acad Sci U S A* 104: 9224-9229.
211. Dean AM (1995) A molecular investigation of genotype by environment interactions. *Genetics* 139: 19-33.
212. Görke B, Stülke J (2008) Carbon catabolite repression in bacteria: many ways to make the most out of nutrients. *Nat Rev Microbiol* 6: 613-624.
213. Shen-Orr SS, Milo R, Mangan S, Alon U (2002) Network motifs in the transcriptional regulation network of *Escherichia coli*. *Nat Genet* 31: 64-68.
214. Wang Z, Zhang J (2011) Impact of gene expression noise on organismal fitness and the efficacy of natural selection. *Proc Natl Acad Sci U S A* 108: E67- E76.
215. Hamilton CM, Aldea M, Washburn BK, Babitzke P, Kushner SR (1989) New method for generating deletions and gene replacements in *Escherichia coli*. *J Bacteriol* 171: 4617-4622.
216. Bigger JW, Nelson JH (1941) The growth of coliform bacilli in distilled water. *J Pathol Bacteriol* 53: 189-206.
217. Postgate JR, Hunter JR (1962) The survival of starved bacteria. *J Gen Microbiol* 29: 233-263.
218. Schaechter M, Maaloe O, Kjeldgaard NO (1958) Dependency on medium and temperature of cell size and chemical composition during balanced growth of *Salmonella typhimurium*. *J Gen Microbiol* 19: 592-606.
219. Hua Q, Yang C, Oshima T, Mori H, Shimizu K (2004) Analysis of gene expression in *Escherichia coli* in response to changes of growth-limiting nutrient in chemostat cultures. *Appl Environ Microbiol* 70: 2354-2366.
220. Ferenci T (1999) Regulation by nutrient limitation. *Curr Opin Microbiol* 2: 208-213.
221. Bremer H, Dennis PP (1996) Modulation of chemical composition and

- other parameters of the cell by growth rate (American Society for Microbiology, Washington, DC).
222. Hartl DL, Dykhuizen DE (1979) A selectively driven molecular clock. *Nature* 281: 230-231.
  223. Dykhuizen DE, Hartl DL (1983) Selection in chemostats. *Microbiol Rev* 47: 150-168.
  224. Herbert D, Elsworth R, Telling RC (1956) The continuous culture of bacteria; a theoretical and experimental study. *J Gen Microbiol* 14: 601-622.
  225. Cooney CL, Wang DI, Mateles RI (1976) Growth of *Enterobacter aerogenes* in a chemostat with double nutrient limitations. *Appl Environ Microbiol* 31: 91- 98.
  226. Chiu SY, Erickson LE, Fan LT, Kao IC (1972) Kinetic model identification in mixed populations using continuous culture data. *Biotechnol Bioeng* 14: 207- 231.
  227. Fredrickson AG (1977) Behavior of mixed cultures of microorganisms. *Annu Rev Microbiol* 31: 63-88.
  228. Jannasch HW, Mateles RI (1974) Experimental bacterial ecology studied in continuous culture. *Adv Microb Physiol* 11: 165-212.
  229. Koch AL (1997) Microbial physiology and ecology of slow growth. *Microbiol Mol Biol Rev* 61: 305-318.
  230. Harvey RJ (1970) Metabolic regulation in glucose-limited chemostat cultures of *Escherichia coli*. *J Bacteriol* 104: 698-706.
  231. Michelsen O, Teixeira de Mattos MJ, Jensen PR, Hansen FG (2003) Precise determinations of C and D periods by flow cytometry in *Escherichia coli* K-12 and B/r. *Microbiology* 149: 1001-1010.
  232. Woldringh CL, Grover NB, Rosenberger FR, Zaritsky A (1980) Dimensional rearrangement of rod-shaped bacteria following nutritional shift-up. II. Experiments with *Escherichia coli* B/r. *J Theor Biol* 86: 441-454.
  233. Koch AL (1979) Microbial growth in low concentrations of nutrients.
  234. Loeb A, McGrath BE, Navre JM, Pierucci O (1978) Cell division during nutritional upshifts of *Escherichia coli*. *J Bacteriol* 136: 631-637.
  235. Taymaz-Nikerel H, van Gulik WM, Heijnen JJ (2011) *Escherichia coli* responds with a rapid and large change in growth rate upon a shift from glucose-limited to glucose-excess conditions. *Metab Eng* 13: 307-318.
  236. Sunya S, Devigne F, Uribebarrea J-L, Molina-Jouve C, Gorret N (2012) Comparison of the transient responses of *Escherichia coli* to a glucose pulse of various intensities. *Appl Microbiol Biotechnol* 95: 1021-1034.



237. Nomura M (1999) Regulation of rbosome biosynthesis in *Escherichia coli* and *Saccharomyces cerevisiae*: diversity and common principles. *J Bacteriol* 181: 6857–6864.
238. Yun HS, Hong J, Lim HC (1996) Regulation of ribosome synthesis in *Escherichia coli*: effects of temperature and dilution rate changes. *Biotechnol Bioeng* 52: 615-624.
239. Zaritsky A, Helmstetter CE (1977) Rate maintenance of cell division in *Escherichia coli* B/r: analysis of a simple nutritional shift-down. *J Bacteriol* 174: 8152-8155.
240. Steinsiek S, Bettenbrock K (2012) Glucose transport in *Escherichia coli* mutant strains with defects in sugar transport systems. *J Bacteriol* 194: 5897-5908
241. Lazebnik Y (2002) Can a biologist fix a radio?--Or, what I learned while studying apoptosis. *Cancer Cell* 2: 179-182.



## Summary

Biological systems are often described as complex. Yuri Lazebnik [241] describes how biologists would find out how radios work, instead of biological organisms, without having any knowledge of electronics. He argues that to understand how cells (or radios) function, it is not enough understand their individual components, and puts forward the need for a more quantitative approach in biology. Systems biology is an attempt to understand how the interaction between different components leads to biological function. Numerous studies have shown heterogeneity within population of cells, and that gene expression noise can be a source of heterogeneity. Consequently, the origins and consequences of stochasticity in gene expression have been well investigated. However, how stochasticity impacts growth is less known.

Significant progress has been made to understand how cells achieve growth homeostasis at the population level. However, how the growth of single cells is impacted during environmental changes remains poorly understood. This thesis is thus concerned with the following fundamental question: how are growing cells responding to perturbations? These perturbations can be either internal, such as gene expression noise, or external, which involve changes in the cellular environment. To address this question, we use a single-cell approach, combined with fluorescence time-lapse microscopy to measure both growth rate with sub-cycle resolution, and expression of genes of interest.

Chapter 2 describes novel microfluidic devices based on polyacrylamide gels, which require minimal investment in microtechnologies. For all the different designs, the organism is confined between a polyacrylamide membrane and the glass coverslip through which microscopy is performed. We demonstrate that these devices allow accurate spatio-temporal control of the environment, and can be used to study diverse organisms. We show that we can control the growth of bacterial colonies, change the carbon source in time and follow the response of single-cell lineages. In addition, we can confine and grow yeasts, imposing a reversible arrest of growth within a defined time window by a microtubules depolymerizing drug. We finally show that we can confine developing nematodes in microchambers and follow by time-lapse microscopy the individual growth of multiple larvae in parallel.

Chapter 3 characterizes the dynamics of bacterial growth during diauxic shift in *Escherichia coli* at the single-cell level. We measure simultaneously single-cell growth at high time resolution, and *lac* expression levels. It is known from bulk data that upon glucose exhaustion, cells experience a phase of growth arrest.

Surprisingly, we find that some cells do not exhibit a lag phase: a fraction of about 15% continues to grow at the same speed. In addition, growth recovery times and induction times of single cells are broadly distributed, and are well correlated. To explain the sustained growth of some cells, we create a minimal stochastic model for the system. Simulations reproduce the experimental results, and show sustained growth in a small fraction of cells provided that the relation between *lac* expression and growth is highly non-linear. Finally, we show that genealogically related cells have similar growth recovery times.

Several studies have shown the exponential nature of bacterial growth, both at the population level and in single cells. Exponential growth reflects the cycle inherent to self-replicating systems, where active components help producing the building blocks that are required for their own synthesis. Chapter 4 is concerned with the growth dynamics of single cells upon exposure to a translation-inhibiting antibiotic that disrupts this cycle. We grow cells on lactose as the sole carbon source, and monitor expression of the *lac* genes as well as other essential enzymes. We found that when antibiotics were added to concentrations that fully blocked *lac* enzyme synthesis, the cells continued to grow linearly for over 12 hrs. In this growth regime, ribosome synthesis is maintained though at a lower rate. In addition, we find that the linear growth rate correlates with the age of cells at the moment of tetracycline addition, resulting in significant cell-to-cell variability. Further increase in antibiotic concentration allows growth to continue transiently, until ribosome synthesis is arrested. We show that in absence of *lac* protein synthesis, existing *lac* proteins are able to sustain cellular growth.

Chapter 5 investigates the propagation of noise in gene expression to growth. We use time-lapse microscopy to measure fluctuations in the expression of *lac* enzymes and in the instantaneous growth rate of single *E. coli* cells, and quantify their time-resolved cross-correlations. Metabolism and growth have been shown to be constant in fixed conditions. We show on the contrary that cellular growth is inherently destabilized, and how this is caused by the stochastic expression of metabolic enzymes. In addition, this growth destabilization involves noise propagation through metabolism. We find that not only fluctuations in the *lac* enzymes propagate to growth, but growth fluctuations in turn perturb expression in general. Hence, reciprocal interactions between expression and growth govern the stability of cellular growth. We develop a minimal stochastic model coupling expression and growth noise. The model reproduces the experimental data, and predicts correlations in rewired networks.

Chapter 6 deals with growth dynamics of single cells during nutrient shifts. Cellular growth rate is modulated by changing the external concentration of glucose, from abundant to limiting glucose and vice-versa. We monitor

both the growth rate and ribosome synthesis over time. Previous studies in bulk measured the number of cells over time, or the OD over time, from which the cell mass was inferred. However, OD measurements cannot properly distinguish between cell elongation and number increase. We find that, during upshift, adaptation to the new growth rate is slow and spanned 4 generations, corresponding to 5 hrs. Production rate of ribosomes increases to the new rate within roughly the same time, and is tightly correlated to the growth rate. The transition from high to low growth rate is comparatively faster: the new steady-state for growth and ribosome synthesis is reached after 2 generations only or 3 hrs. Here, growth decrease precedes ribosome production rate decrease. In both cases however, the response of single cells to nutrient shifts is rather homogeneous.



## Samenvatting

Biologische systemen staan bekend om hun complexiteit. Yuri Lazebnik [241] beschreef hoe biologen, zonder enige kennis van electronica, zouden moeten uitvinden hoe radio's werkten in plaats van biologische organismen. Hij beoogt dat het niet voldoende is om de uitzonderlijke componenten van de cel (of een radio) te begrijpen om de werking van het geheel te begrijpen, en pleit verder voor meer kwantitatieve benaderingen in de biologie. Systeembioologie probeert te achterhalen hoe de wisselwerkingen tussen verschillende componenten leiden tot een biologische functie. Een groot aantal onderzoeken heeft variaties laten zien in celpopulaties en dat ruis in genexpressie een bron van variaties kan zijn. Zodoende zijn de oorzaken en gevolgen van stochasticiteiten in genexpressie uitgebreid onderzocht. Echter, de invloed van stochasticiteiten op groei is niet onderzocht.

Er is aanzienlijke vooruitgang geboekt in de kennis van hoe cellen groei-homeostase bereiken op populatieniveau. Echter, de invloed van veranderingen in de omgeving op de groei van enkele cellen is niet helder. In dit proefschrift staat de volgende fundamentele vraag centraal: hoe reageren groeiende cellen op verstoringen? Deze verstoringen kunnen intern plaats vinden, zoals ruis in de genexpressie, of, externe storingen betreffende veranderingen in de celomgeving. Om deze vraag te beantwoorden hanteren we een benadering voor een enkele-cel- systeem gecombineerd met tijdsverloop fluorescentiemicroscopie om zowel de groeitempo met subcyclusresolutie als de expressie van genen die van belang zijn te meten.

Hoofdstuk 2 beschrijft nieuwe microfluidische apparaten gebaseerd op polyacrylamide gels, die een minimale investering vereisen in microtechnologieën. Bij elke apparaat met een specifiek ontwerp is het organisme opgesloten tussen een polyacrylamide membraan en een dekglasje en dit is geschikt voor microscopie. We tonen aan we met deze apparaten nauwkeurige veranderingen teweeg kunnen brengen in zowel plaats als tijd en deze apparaten kunnen worden ingezet om verschillende organismen te bestuderen. We laten zien dat we de groei van de bacteriekoloniën kunnen beheersen, de koolstofbron veranderen als functie van tijd en de reactie van afstemmingen van een individuele cel. Daarbovenop kunnen we gist opsluiten en groeien, een omkeerbare groeistilstand opleggen binnen een gedefinieerd tijdsvak met een drug dat depolymerisatie van microtubuli tot stand brengt. Tot slot laten we zien dat we ontwikkelde nematoden in microkamers kunnen opsluiten en de individuele groei van meerdere larven simultaan kunnen volgen.

Hoofdstuk 3 karakteriseert de dynamica van bacteriegroei tijdens verandering van catabolietrepressie in *Escherichia coli* op het enkele cel niveau. We meten parallel de groei van enkele cellen met een hoge tijd resolutie en *lac* expressieniveaus. Van bulkdata is bekend dat bij glucose-uitputting cellen een fase van groeistilstand ondergaan. Verrassend genoeg zien we dat sommige cellen geen vertragingfase tonen: een deel van ongeveer 15% blijft op dezelfde snelheid groeien. Bovendien zijn de groeiherstellingstijden en de inductietijden van enkele cellen breed verdeeld en goed gecorreleerd. Om de aanhoudende groei van sommige cellen te verklaren, creëren we een minimaal stochastisch model voor het systeem. De simulaties weergeven de experimentele resultaten en laten een aanhoudende groei zien in een klein deel van de cellen, mits de relatie tussen de *lac* expressie en de groei zeer niet lineair is. Tot slot laten we zien dat genealogisch gerelateerde cellen gelijksoortige groeiherstellingstijden hebben.

Verscheidende studies hebben een exponentieel eigenschap van bacteriegroei laten zien zowel op populatieniveau als in enkele cellen. Exponentiële groei weerspiegelt de cyclus dat inherent is aan systemen die zichzelf kopiëren, waar actieve componenten meehelpen aan het produceren van de bouwstenen die nodig zijn voor hun eigen synthese. Hoofdstuk 4 betreft de groeidynamica van enkele cellen na blootstelling aan een translatiestremmingsantibioticum dat deze cyclus verstoort. We groeien cellen op lactose als de enige koolstofbron en zien toe op zowel de expressie van *lac* genen als andere essentiële enzymen. We vinden dat wanneer antibiotica toegevoegd werden in hoeveelheden dat het *lac* enzyme synthese volledig blokkeert, de cellen lineair blijven groeien gedurende 12 uur. In dit groeiregime is de ribosomensynthese behouden, al is het op een lager tempo. Daarnaast vinden we dat de lineaire groeitempo correleert met de leeftijd van de cellen op het moment van toevoeging van tetracycline, wat resulteert in een significante cel-tot-cel variatie. Verdere toeneming van de antibioticaconcentratie staat toe dat de groei tijdelijk doorgaat totdat de ribosoomsynthese is tegengehouden. We laten zien dat in de afwezigheid van *lac* eiwitsynthese de bestaande *lac* eiwitten in staat zijn de celgroei te steunen.

In hoofdstuk 5 wordt de voortplanting van ruis in de genexpressie tot groei onderzocht. We meten fluctuaties in de expressie van *lac* enzymen en in de ogenblikkelijke groeitempo van enkele *E. coli* cellen en kwantificeren hun tijdsopgeloste kruiscorrelaties. Hoewel uitgewezen is dat metabolisme en groei constant zijn in bepaalde condities, hebben wij het tegendeel laten zien dat celgroei inherent gedestabiliseerd is en hoe dit is veroorzaakt door stochastische expressie van metabolistische enzymen. Daarbij heeft deze destabilisatie in groei betrekking tot ruisvoortplanting via metabolisme. Niet alleen vinden we dat fluctuaties in de *lac* enzymen aanzetten tot groei, maar ook de fluctuaties in groei op hun

beurt de expressie verstoren in het algemeen. Dus, wederkerige wisselwerkingen tussen expressie en groei bepalen de stabiliteit van celgroei. We ontwikkelen een minimaal stochastisch model dat expressie met ruis in de groei koppelt. Het model reproduceert de experimentele bevindingen en voorspelt de correlaties in samengebrachte netwerken.

Hoofdstuk 6 heeft te doen met de groeidynamica van enkele cellen gedurende veranderingen van voedingsstoffen. De celgroei tempo is gemoduleerd door het veranderen van de externe glucoseconcentratie, van overvloedig tot gelimiteerd glucose en vice-versa. We beschouwen zowel het groei tempo en de ribosoomsynthese in tijd. Voorgaande bulkstudies hebben het aantal cellen gemeten in tijd, of de OD in tijd, waarvan het celgewicht is afgeleid. Echter, OD metingen kunnen niet naar behoren celrekking onderscheiden van een toename in aantal. We vinden dat tijdens een verandering van lage naar hoge glucoseconcentratie de omschakeling naar het nieuwe groei tempo langzaam verloopt en 4 generaties overspant, wat correspondeert met 5 uur. Het tempo van het aanmaken van ribosomen stijgt tot het nieuwe tempo in ruwweg dezelfde tijd en is strak gecorreleerd met het groei tempo. De overgang van hoge naar lage groei tempo verloopt relatief sneller: het nieuwe evenwicht voor groei en ribosoom synthese is al bereikt na 2 generaties ofwel 3 uur. In dit geval gaat de afname in groei vooraf aan de afname in productietempo van ribosomen. Echter in beide gevallen is de reactie van enkele cellen op de veranderingen in voedingsstoffen tamelijk homogeen.





## Acknowledgements

‘There’s an old joke - two elderly women are at a Catskill mountain resort, and one of ‘em says, “Boy, the food at this place is really terrible.” The other one says, “Yeah, I know; and such small portions.”’ (Woody Allen). That’s essentially how I feel about doing a PhD - lots of frustration, and it’s all over much too quickly. Joke apart, there are many people whom I’d like to thank and shared with me these four years at AMOLF. Sander, thank you for giving me the chance to do fundamental research in your lab and all your good advice. I’ll miss your enthusiasm and excitement for new ideas. I would also like to thank people from my group, past and present. Daan, my first year-second supervisor, thank you for teaching me how to grow bacteria, observe them, and analyze the data (Schnitzhell!), but also for always taking the time to answer my many questions. Marjon, the lab has become so quiet without you! Thanks for your positive attitude and energy. Alex, my first office mate and neighbor, thanks for your help in the lab. Philippe, your ability to understand and solve both scientific and technical problems, and your many good ideas have always impressed me (that, and the speed at which you can read papers). It was great to work with you. Noreen, Sebastian, Katja, and David (ze Germans), Alireza, Sergey, Fatemeh, Arif, Dmitry, thank you for your input and discussions during group meetings. Keep up the good work! Vanda, thank you for contributing to this work (I can’t count all the strains you’ve made), but also for our many discussions and sharing stories, I will certainly miss them. Roland, though you’re not technically part of the group, you were the first one to show me around the lab, and I thank you for all the times you helped me with Killer Mike.

I was extremely lucky to have in my office in the new building Iza and Philippe. I shared both the ups and downs of my PhD with you, but also a lot of fun outside the office. It was sad to see you leave, and I have missed you since. Thanks for all the good times. Jeanette, my squash partner and Dutch translator, it’s always nice to talk to you as you seem to enjoy sarcasm as much as I do. Laurens, totally awesome dude! The French connection, Pierre, François, Sophie, Georges, merci pour votre humour (vos blagues désopilantes vont me manquer) et nos lunches 100% camembert. Chris (papa Rétif), Hincó and Lukasz (Wookie), thanks for making my time here so enjoyable. Milena, I’ll miss your craziness. Tomek, I’ll miss your crazy stories. José, I’ll miss your exuberance and good mood. We started more or less at the same time and are going to graduate at the same time as well. It was nice to have you as road companions. Filipe and Pieter Rein, thank you for your contribution to my work. I would like to thank all my

colleagues for setting such a good atmosphere; AMOLF really is a special place.

Last but not least, I would like to thank the van Engeland family: bedankt voor alle mooie momenten in Grashoek en Amsterdam. Will en Gerrie, veel succes met de B&B. Papou, Mamou et Vincent, merci pour tout. Thijs, my last words are for you: we've had so many great times together, and I'm now looking forward to our next great adventure(s)!

## List of publications

P. Nghe\*, S. Boulineau\*, S. Gude, P. Recouvreux, J. van Zon and S.J. Tans  
Controlling living cells and organisms with microfabricated polyacrylamide membranes

*Manuscript in preparation*

S. Boulineau, F. Tostevin, D.J. Kiviet, P.R. ten Wolde, P. Nghe and S.J. Tans  
Single-cell dynamics reveals sustained growth during diauxic shift  
PLoS ONE 8(4): e61686 (2013)

S. Boulineau and S.J. Tans  
Prolonged linear growth in single bacterial cells upon exposure to antibiotics

*Manuscript in preparation*

D.J. Kiviet\*, P. Nghe\*, S. Boulineau and S.J. Tans  
Noise propagation from enzyme expression to cellular growth, and back

*In revision*

S. Boulineau and S.J. Tans  
Transient dynamics during nutrient shifts

*Manuscript in preparation*

\* Joined first authors



# Curriculum Vitae

## Sarah Boulineau

- 08-07-1986      Born in Nice, France.
- 2000 – 2003      Lycée Thierry Maulnier, Nice.
- 2003 – 2005      Preparatory classes, Nice.
- 2005 – 2008      Master's Degree in Engineering (French diplôme d'ingénieur),  
ECPM (School of Chemistry, Polymers and Materials Science),  
Strasbourg, France.  
Final project at Philips Research, Eindhoven, the Netherlands.
- 2009 – 2013      Ph.D. research,  
FOM-Institute AMOLF, Amsterdam, the Netherlands.  
Biophysics group of prof. dr. S.J. Tans.

